UNC-5082

HYDROGEN THERMAL CONDUCTIVITY AT TEMPERATURES FROM 2000 to 4600°F

Final Report

S. L. Israel
T. D. Hawkins
R. T. Salter
S. C. Hyman

April 14, 1964

Work Performed under UNC Project 2194
Contract NAS 3-3205 for the National
Aeronautics and Space Administration

GPO PRICE $ _____

CFSTI PRICE(S) $ _____

Hard copy (HC) 4.00

Microfiche (MF) 1.00

ff 653 July 65

UNITED NUCLEAR CORPORATION
DEVELOPMENT DIVISION
5 New Street
White Plains, N.Y.

UNC-5082

HYDROGEN THERMAL CONDUCTIVITY AT TEMPERATURES FROM 2000 to 4600°F

Final Report

S. L. Israel
T. D. Hawkins
R. T. Salter
S. C. Hyman

April 14, 1964

Work Performed under UNC Project 2194
Contract NAS 3-3205 for the National
Aeronautics and Space Administration

UNITED NUCLEAR CORPORATION
Development Division
White Plains, New York

ABSTRACT

The thermal conductivity of hydrogen at 150 psia was determined from the measured effective conductivity of porous tungsten specimens filled with pressurized hydrogen. A truncated-sphere model of the porous structure was used to relate the gas conductivity to the effective conductivity of the gas-filled specimen. Effective conductivities were determined from temperature measurements on the upper circular surface of the right circular cylindrical porous specimen heated by high frequency induction currents.

CONTENTS

FIGURES

1. SUMMARY

The thermal conductivity of hydrogen at 150 psia was determined from measured effective conductivities of hydrogen-filled porous-tungsten specimens. A truncated-sphere model of the porous structure was used to relate the hydrogen thermal conductivity to the measured effective conductivity of a hydrogen-filled porous-tungsten body. This analytical model permits adjustment of the particle contact area to allow for variation in the degree of sintering in the three specimens used in the tests. The particle contact area for each specimen is determined from the effective conductivity of the specimen in vacuum. By specifying the particle contact area, a unique relationship is obtained which permits determination of the hydrogen thermal conductivity from the measured effective conductivity of the hydrogen-filled porous-tungsten specimen without any additional information.

The effective thermal conductivity of the hydrogen-filled porous-tungsten structure is determined from temperature measurements on the upper circular surface of a right circular cylindrical specimen heated by high frequency induction currents in a thin layer at the outer cylindrical surface. See Fig. 1. This experimental technique has been used previously by Hoch[1] to determine the thermal conductivity of refractory metals at elevated temperatures. The surface temperature measurements are used as boundary conditions for the relevant heat conduction boundary-value problem from which the temperature distribution within the specimen is determined. The effective conductivity is calculated by equating the axial, centerline heat flux at the surface of the specimen, determined from the solution of the

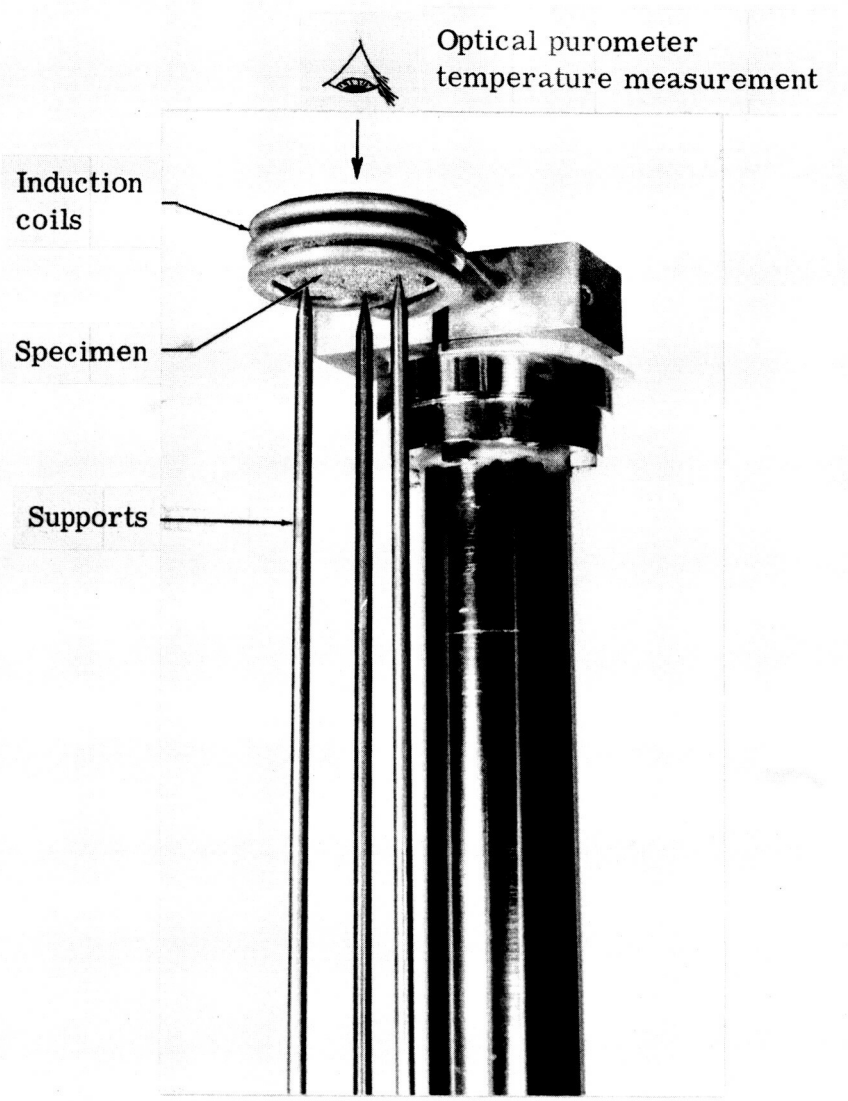

Fig. 1 — Test arrangement

boundary-value problem, to the radiation and thermal convection heat losses at the same point.

The thermal conductivity of hydrogen, determined by the above method, compares reasonably well with previous experimental and theoretical work. The conductivity increases with increasing temperature as shown in Fig. 2. The thermal conductivity of solid tungsten measured in the course of the project is 51.2 Btu/hr-ft-°F in the range from 2000 to 4700°F.

The basic approach to determine the gas conductivity from the measured effective conductivity of the hydrogen-filled porous-tungsten specimen has yielded satisfactory results. Additional experimental work is warranted to provide more gas conductivity data and to provide more reliable information on the emittances and thermal convection quantities that enter into the calculation of the gas conductivity.

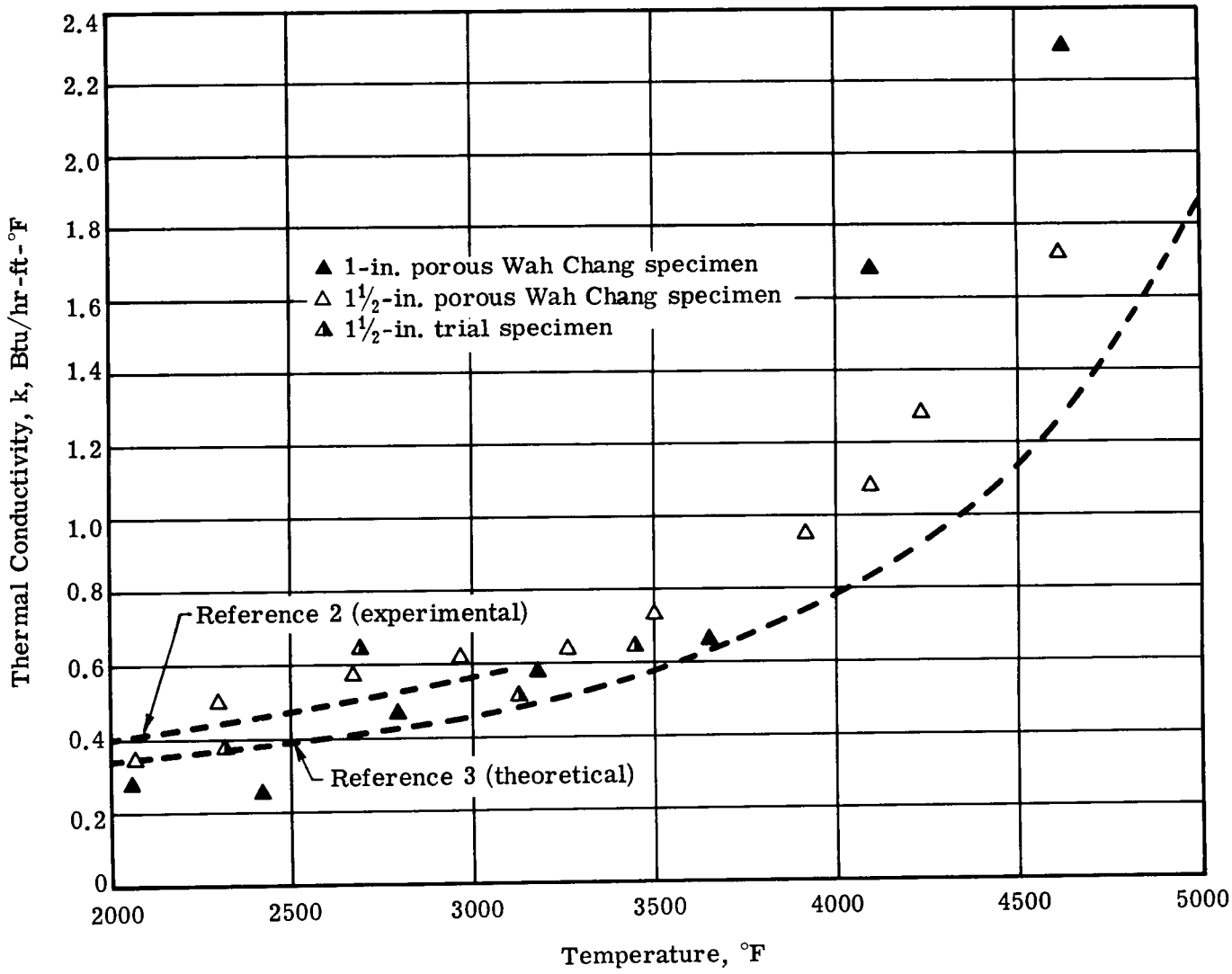

Fig. 2 — Thermal conductivity of hydrogen at 150 psia

2. INTRODUCTION

2.1 BACKGROUND AND PURPOSE OF INVESTIGATION

Considerable work has been done recently on designing nuclear rockets and other devices which use hydrogen as a coolant or propulsive fluid at high temperatures. This work has led to a need for reliable data on the transport properties, including the thermal conductivity, of hydrogen gas at temperatures in the vicinity of 5000°F. Previously available experimental data on the thermal conductivity extend up to 3000°F;[2] theoretical calculations[3] based on intermolecular properties indicate that at higher temperatures the thermal conductivity of hydrogen rises steeply with temperature, and is strongly dependent on pressure, even at pressures above one atmosphere.

The purpose of the present investigation is to measure the thermal conductivity of hydrogen at temperatures up to 5000°F. These measurements provide independent data for the value of hydrogen thermal conductivity in the range 2000 to 5000°F, and provide a comparison with the predicted strong increase at temperatures above 3000°F.

2.2 PROBLEMS IN MEASURING THERMAL CONDUCTIVITIES OF GASES AT HIGH TEMPERATURES

The usual method of measuring the thermal conductivity of a gas is to measure the temperature drop through a plane or annular layer of the gas with a known

heat flux through the layer. In this method, two principal sources of error exist:

1. Radiation from solid surface to solid surface across the gas layer.
2. Convection of the gas within the layer.

Both of these effects increase the heat flux through a layer with a given temperature drop. At low temperature levels, the radiative heat flux is usually small in comparison with the conductive heat flux, so that an approximate correction for radiation allows good accuracy in determining the conductive heat flux. The effect of convection also may be minimized by keeping the temperature difference small and by employing baffles.

At high temperatures, radiation becomes dominant, and small errors in correcting for this effect may cause large relative errors in determining the conductive heat flux. Also, it is more difficult to maintain small temperature differences at high temperature levels, leading to increased errors due to convection. In addition to these effects, problems involving thermal expansion and mechanical strength of the enclosing structure become important.

Therefore, reliable measurement of the thermal conductivity of a gas at temperatures above 3000°F requires the use of a new experimental method.

2.3 APPROACH TAKEN IN PRESENT PROGRAM

The approach taken in this program is to determine the thermal conductivity of hydrogen gas indirectly from the measured effective or apparent thermal conductivity of a porous tungsten body filled with hydrogen at the desired temperature level. An analytical model of the structure of the porous body and the various modes of internal heat transfer, in conjunction with the measured effective conductivity of the porous body in vacuum, is used to determine the thermal conductivity of the hydrogen from the measurements on the gas-filled body.

The small scale of the porous structure (initial particle size 0.006 to 0.010 in.) serves to minimize both radiation and convection within the gas-filled body, while still being large compared with the mean free path in the gas at the operating pressure of 150 psia.

Structural problems at high temperatures are eliminated by freely supporting the cylindrical test specimen and heating it with high frequency induction currents. No direct contact with the specimen by heating or temperature measuring apparatus is required.

In this method, developed by Hoch[1] for measuring the thermal conductivity of a solid at high temperatures, the specimen is allowed to radiate freely from its end surfaces. Temperature observations on only one surface by means of an optical pyrometer, together with appropriate mathematical analysis, are required to determine the effective conductivity of the specimen.

The determination of the thermal conductivity of hydrogen from the effective conductivity of the gas-filled specimen is based on the analysis of the modes of heat transfer in a gas-filled porous body, and the use of an analytical model of the particle shape and arrangement.

The analysis of heat transfer in the porous body is described in Section 3, the experimental apparatus is described in Section 4, and the analysis of the data is described in Section 5. The results are presented and discussed in Section 6.

3. ANALYSIS OF HEAT TRANSFER IN GAS-FILLED POROUS BODIES

3.1 GENERAL DISCUSSION

The experimental procedure of the present program, coupled with the analysis of Hoch et al.,[1] described in Section 5, yields values for the apparent or effective thermal conductivity of the porous solid-gas combination. In order to determine the thermal conductivity of the gas, an additional analysis is required to relate the effective conductivity of the solid-gas combination to the individual conductivities of the solid and gas components.

The development of such an analysis requires an understanding of the various characteristics of a porous structure and their effects on the different mechanisms of heat transfer within the gas-filled porous body. Once this basic understanding has been achieved, then it is possible to develop a simplified physical model of the porous structure, which will include the important heat-transfer mechanisms in their proper relationship, and will be amenable to simple mathematical analysis.

3.2 HEAT-TRANSFER CHARACTERISTICS OF GAS-FILLED POROUS BODIES

The various heat-transfer mechanisms in gas-filled porous bodies have been identified and discussed by Yagi and Kunii[4] and by Kunii and Smith,[5] who developed a simplified equivalent physical structure, and a corresponding algebraic expression for the apparent conductivity in terms of porous-structure parameters and the conductivities of the solid and gas phases. The following heat-transfer mech-

anisms, shown schematically in Fig. 3, exist in a porous body filled with a stagnant gas:

1. Direct solid conduction through areas of actual particle-to-particle contact
2. Direct gas conduction through areas of pore-to-pore communication
3. Series conduction through solid and gas
4. Particle-to-particle radiation across a gas layer
5. Pore-to-pore radiation bypassing the particles.

Of these mechanisms, 1, 2, 3, and 5 may be considered to be in parallel, and 4 to be in parallel with the gas part of 3. Once these heat-transfer mechanisms have been identified and their relationships noted, it is possible to formulate a simplified physical model of a gas-filled porous body and its resulting heat-transfer properties. In this model, the three-dimensional heat transfer within the porous body is reduced to a number of one-dimensional paths, as shown schematically in Fig. 4. Although the model and the resulting general heat-transfer equation are one-dimensional, the three-dimensional geometry of the solid particles is accounted for in determining the relative widths a, δ, and 1-a-δ of the parallel paths and the relative thicknesses ℓ_s and ℓ_g of the layers in series.

The equation for the effective conductivity of this simplified model is

$$k_e = \delta k_s + a k_g + \frac{1 - a - \delta}{\frac{\ell_s}{\ell k_s} + \frac{1}{\frac{\ell k_g}{\ell_g} + \ell h_{rs}}} + a \ell h_{rp}$$

in which the radiation effects have been expressed in terms of equivalent heat-transfer coefficients h_{rs} for surface-to-surface radiation and h_{rp} for pore-to-pore radiation.

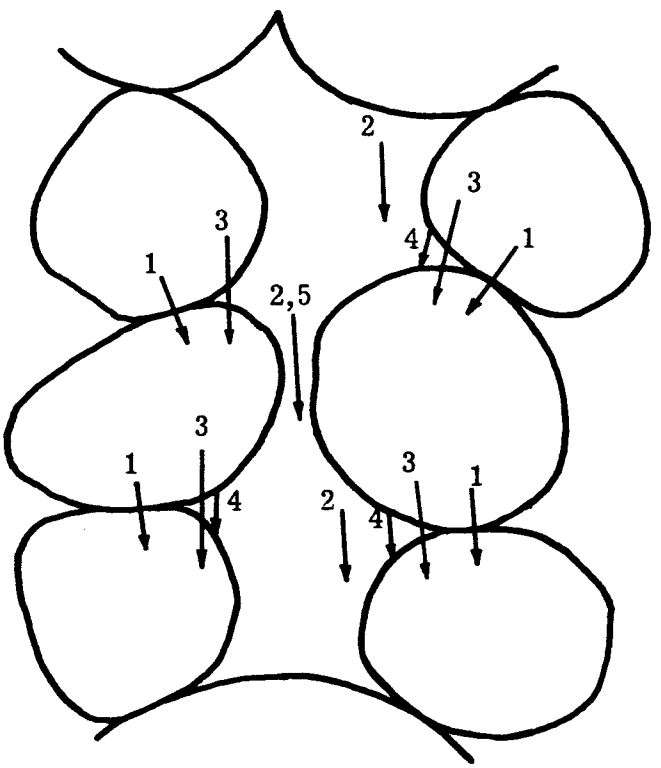

1,2,3 – Conduction
4,5 – Radiation

Fig. 3 — Heat transfer mechanisms in a gas-filled porous body

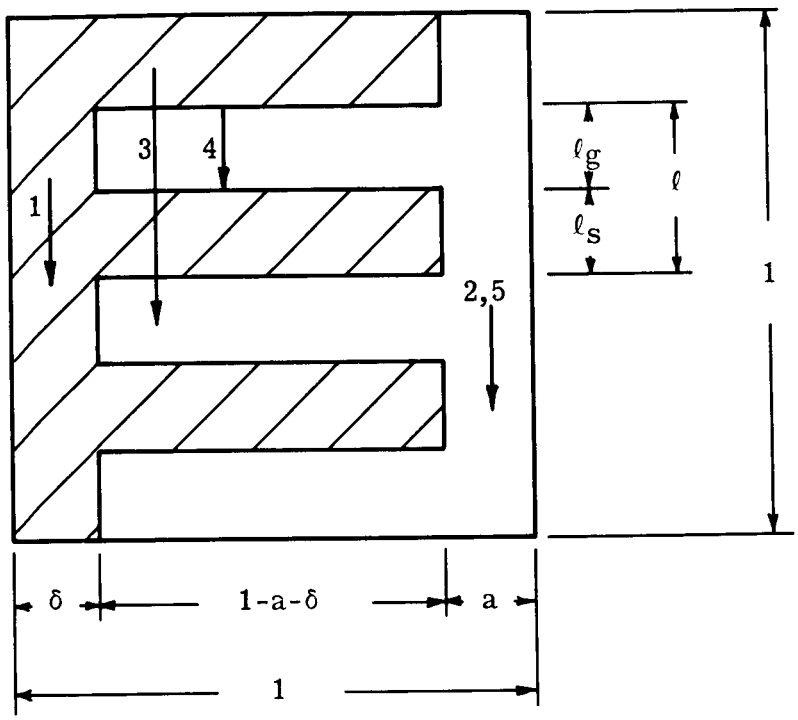

Fig. 4 — Simplified one-dimensional model of porous structure

In the above equation, the first term represents the solid conduction, the second term the gas conduction, the third term the combined effects of series conduction and particle-to-particle radiation, and the fourth term the pore-to-pore radiation.

It is convenient to write the equation in dimensionless form and to define $\varphi_g = \ell_g/\ell$ to yield

$$\frac{k_e}{k_s} = \delta + a\frac{k_g}{k_s} + \frac{1 - a - \delta}{(1 - \varphi_g) + \dfrac{1}{\dfrac{1}{\varphi_g}\dfrac{k_g}{k_s} + \dfrac{\ell h_{rs}}{k_s}}} + a\frac{\ell h_{rp}}{k_s} \qquad (1)$$

This equation helps in understanding the combined heat-transfer properties of a gas-filled porous body in several ways:

1. It shows the direct effect of solid contact area δ, which is expected to be significant for highly-sintered metallic particles
2. It shows the relation of the two radiation terms to the actual conduction terms; in particular, the coupling of the particle-to-particle radiation to conduction through the gas layer
3. By examining the form taken by the equation in vacuum ($k_g = 0$)

$$\frac{k_e}{k_s} = \delta + \frac{1 - a - \delta}{(1 - \varphi_g) + \dfrac{k_s}{\ell h_{rs}}} + a\frac{\ell h_{rp}}{k_s},$$

it can be seen that a measurement of the effective conductivity in vacuum at one particular temperature does not distinguish between solid contact and internal radiation. Since the equivalent heat-transfer coefficients for radiation, h_{rs} and h_{rp}, are proportional to the cube of the temperature level, a series of measurements at different temperature levels should determine the importance of the radiation terms.

However, the above general equation does not yield explicit information on the influence of particle shape. The entire effect of conduction in series through solid

and gas layers is included in the unknown parameter φ_g, which in general is a function of the conductivity ratio k_g/k_s; it is a constant only for special particle shapes.

Therefore, the above simplified physical model and the resulting equation are not sufficient to determine the heat-transfer characteristics of a gas-filled porous solid. Additional information is needed, either in the form of a calibration with a gas of known conductivity, or in the form of knowledge of the actual particle shape. Of course, a complete description of particle shapes in a real porous solid is not practicable. However, a reasonable approximation to an average particle shape should be sufficient to predict the overall heat-transfer characteristics of the body.

3.3 PREVIOUSLY-USED MODELS OF POROUS STRUCTURES

Several investigators have successfully used simplified models of particle shapes to predict the effective conductivity of gas-filled porous solids. Deissler and Eian[6] considered two specific geometries:

1. Spheres in cubic array (porosity 0.475)
2. Right circular cylinders in square array (porosity 0.215).

The effective conductivities of these two geometries were calculated by means of simple integrations, based on the assumption that the local heat flux is everywhere parallel to the direction of the overall temperature gradient (zero lateral conductivity). These results, and those for the two limiting cases of all solid and all gas, were then cross-plotted and interpolated to yield predicted effective conductivities for the entire range of porosity (0 to 1), without reference to a specific geometrical structure at intermediate values of porosity.

The predicted values of effective conductivity were then compared with measured values for a compacted powder filled with various gases. The agreement between theory and experiment was reasonably good; since the material had a porosity of

0.42, the agreement appears to be principally a justification of the spherical model (porosity 0.475) rather than of the entire analysis.

Gorring and Churchill[7] performed a similar analysis in which a variable parameter in the description of the particle shape allowed adjustment of the porosity. The particle shape assumed was a body of revolution bounded by a cubic curve. The variable parameter allowed finite contact, point contact, or a gap in the lateral direction, but, in the direction of heat transfer, point contact was always assumed. The results of this analysis were also tested against experiments with a variety of gas-filled porous materials. Agreement was generally good except for sintered metallic materials.

Previous work shows that simplified geometrical models of particle shapes have been successful in predicting the conduction heat transfer properties of gas-filled porous materials. However, the analyses described do not treat either solid-contact or radiation effects, which must be considered separately.

3.4 TRUNCATED-SPHERE MODEL

Because of the established success of the spherical-particle model in handling the effect of gas conductivity on the important series-conduction mode of heat transfer in gas-filled porous materials, a model was sought in this program which would treat this effect similarly, but would also allow for the effect of solid contact area in a sintered material. As discussed in Section 5, the data for the porous-tungsten specimens tested in vacuum show that there is a significant amount of solid conduction. Therefore, the model must account properly for this important effect.

The model chosen to correlate the data for porous tungsten filled with hydrogen or helium consists of truncated spheres in cubic array, each sphere having six circular flat spots in contact with its neighbors. The local heat flux is assumed to

be everywhere parallel, in a direction normal to one pair of contact spots. Since the relative size of the contact area is the only adjustable parameter in this model, it is chosen to agree with the observed conductivity of the porous solid in vacuum, rather than to adjust the porosity of the model structure. Therefore, the porosity is not considered directly, but follows as a consequence of the assumed structure and the required value of conductivity in vacuum.

The analysis of the effective conductivity of the array of truncated spheres is given in Appendix I (Section 7). As discussed in Section 5, the data for the porous specimens in vacuum do not show any recognizable effect of radiation with increasing temperatures; therefore, the analysis used includes only the true conduction effects (modes 1, 2, and 3 of Section 3.2). The resulting expression for the effective conductivity is

$$\frac{k_e}{k_s} = \delta + \frac{\pi}{2}\frac{\beta}{(1-\beta)^2}\left[\ln\frac{1}{\beta} - (1-\beta)\right] + \left(1 - \frac{\pi}{4} - \delta\right)\beta \qquad (2)$$

where β is the conductivity ratio k_g/k_s. As discussed in the appendix, this expression involves a slight approximation to the geometry of the porous structure. The effect of this approximation is shown to be negligible over the entire range of conductivity ratio β.

When $\beta = 0$ (porous solid in vacuum), Eq. 2 reduces to

$$\frac{k_e}{k_s} = \delta$$

This result agrees with the results of experiments in vacuum; i.e., the effective conductivity of each specimen is a constant fraction of the conductivity of solid tungsten, and no effect of internal radiation is observed. Therefore, for any particular porous specimen, the value of the contact parameter δ can be determined by means of tests in vacuum. Eq. 2 is then an explicit relation between the

conductivity ratios k_e/k_s and k_g/k_s for all tests with that specimen in any gas atmosphere.

The derivation of Eq. 2 is equivalent to determining the parameters a and φ_g in Eq. 1, for the special case of no radiation. The values of these parameters for the truncated-sphere model may be obtained, from comparison of Eqs. 1 and 2, as

$$a = 1 - \frac{\pi}{4} - \delta$$

$$\varphi_g = \frac{2(1 - \beta)}{\ln \frac{1}{\beta} - (1 - \beta)} - \frac{\beta}{1 - \beta}$$

Eq. 2 is plotted in Fig. 5 for values of specimen contact area δ covering the entire possible range from 0 to 1. This figure shows the strong effect of contact area on the effective conductivity of the gas-filled porous solid, and confirms the necessity of using a model which accounts for the contact area.

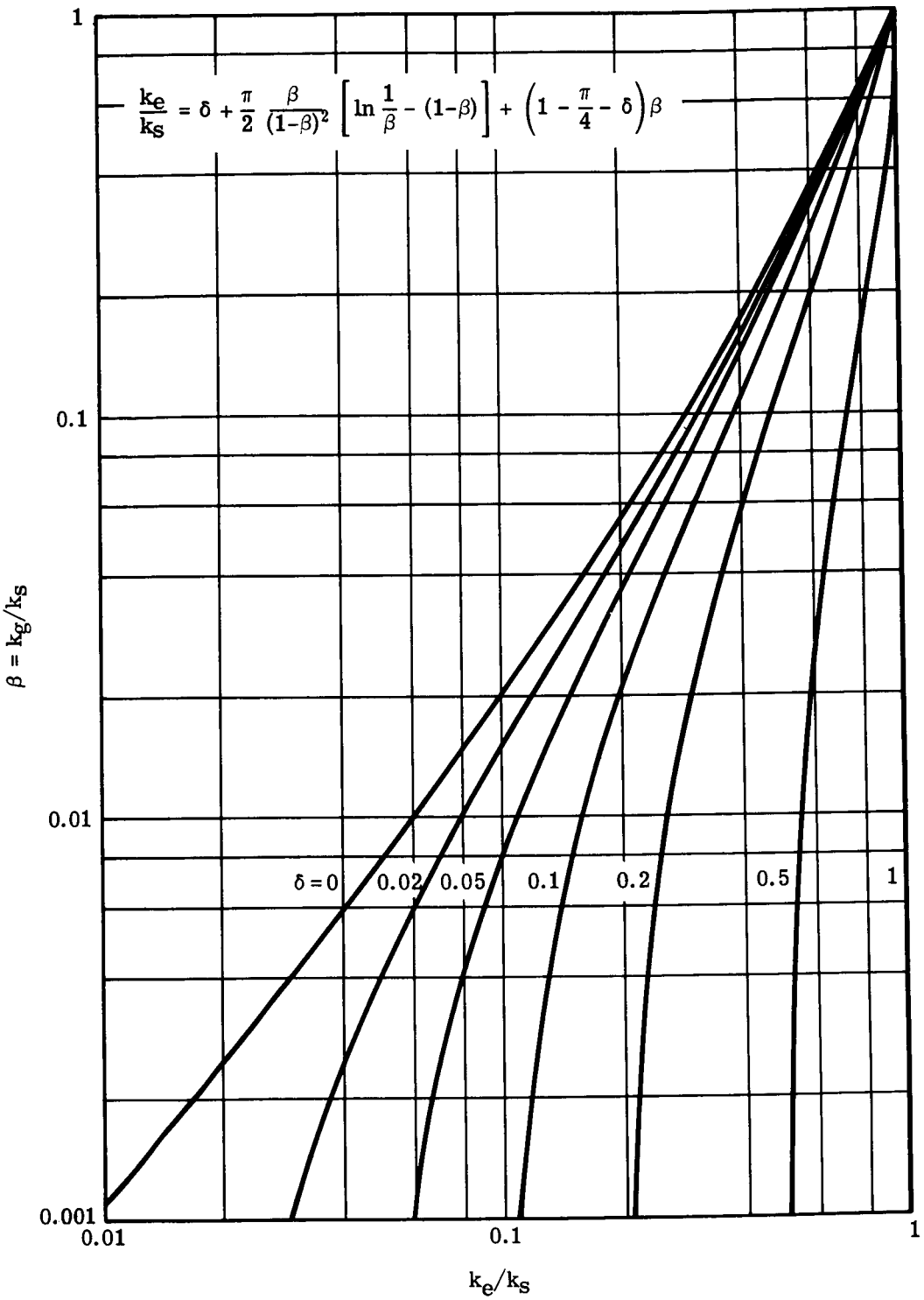

Fig. 5 — Effective conductivity truncated-sphere model

4. EXPERIMENTAL OPERATION

To acquire the necessary effective conductivity measurements for determining the thermal conductivity of hydrogen, an experimental facility has been designed, assembled, and operated at UNC's Development Division laboratories. The facility provides the required conditions for determining the thermal conductivity of solid and porous tungsten specimens in vacuum and in pressurized gas atmospheres at temperatures up to 5000°F.

The experimental approach has been previously used by Hoch and Nitti[1] for the determination of refractory metal thermal conductivities at elevated temperatures. In this method, heat is generated by high frequency induction currents in a thin layer at the outer surface of a right circular cylindrical specimen, thus maintaining an essentially uniform temperature at this cylindrical surface. Heat losses from the circular end surfaces of the specimen lead to temperature distributions with a minimum temperature at the center of the end faces. These experimentally measured temperature distributions on the upper surface of the specimen and a knowledge of the total hemispherical emittance for the specimen are the only information needed to determine the effective average thermal conductivity of the specimen. The details of the heat-transfer analysis of this method are given in Section 5.

This experimental approach simplifies specimen mounting requirements at elevated temperatures since only a tripod is necessary for support with minimum

contact with the specimen. It also eliminates the need for insulation and radiation shields that are customarily required in high temperature resistance heated furnaces.

4.1 APPARATUS

The experimental facility is composed of three basic units (heating unit, test chamber including specimens and instrumentation, and atmosphere control) which are housed in a sheet metal enclosure, approximately 10 × 15 ft, as shown in Fig. 6. A schematic layout of the test chamber and atmosphere control system portion of the facility is shown in Fig. 7. A 220-volt, 200-ampere, 3-phase power supply and 20 gpm water supply and drainage system service the experimental apparatus. A complete set of working drawings used to fabricate the various items of equipment is assembled in Appendix II.

The heating apparatus consists of a high-frequency electronic power supply and a bell jar table, purchased from Lepel High Frequency Laboratories. The converter (Model T-20-3-KC-R-S), serviced by a 200-volt, 150 ampere, 3-phase power supply and a 7 gpm, 60 psig water supply, is capable of 20 kw power at frequencies from 300 to 450 kc. The frequency, which is determined by tuning requirements, is approximately 300 kc for this application. The bell jar table (Model 7414), which contains a step-down transformer, is connected to the generator by water-cooled, high-frequency leads from the primary of its transformer. The step-down transformer provides better power transfer from the load coils to the tungsten specimen and, because of reduced voltage across the load coils, minimizes gas ionization in the test chamber when operating under a partial vacuum. The bell jar table serves as a stand for the test chamber and contains a coaxial lead-through and load-coil fixture that provides power inside the test chamber. The secondary of the step-down transformer has a separate 1.5 gpm water supply which cools the load coil and coaxial lead-through.

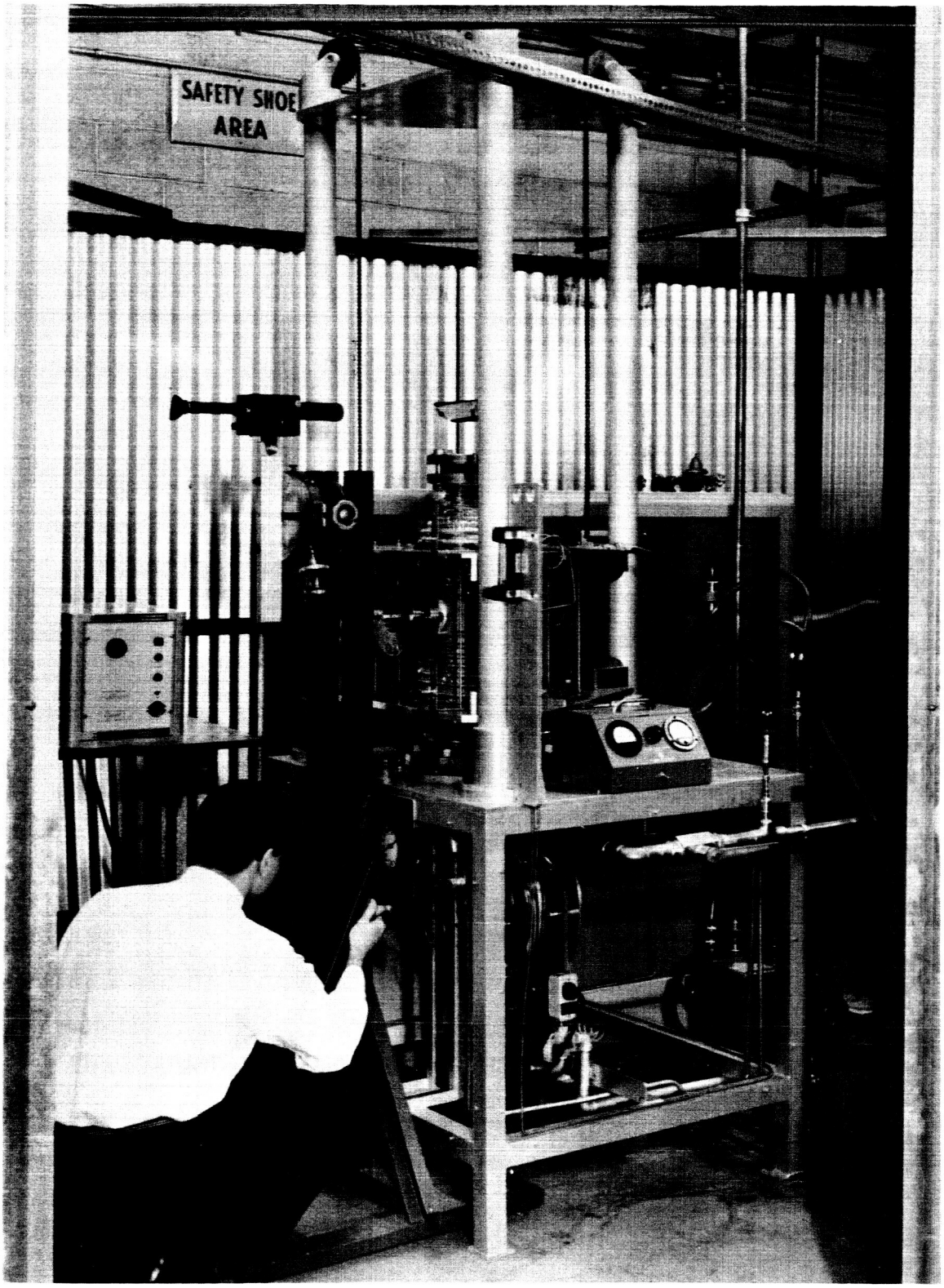

Neg. No. 4481

Fig. 6 — Experimental facility

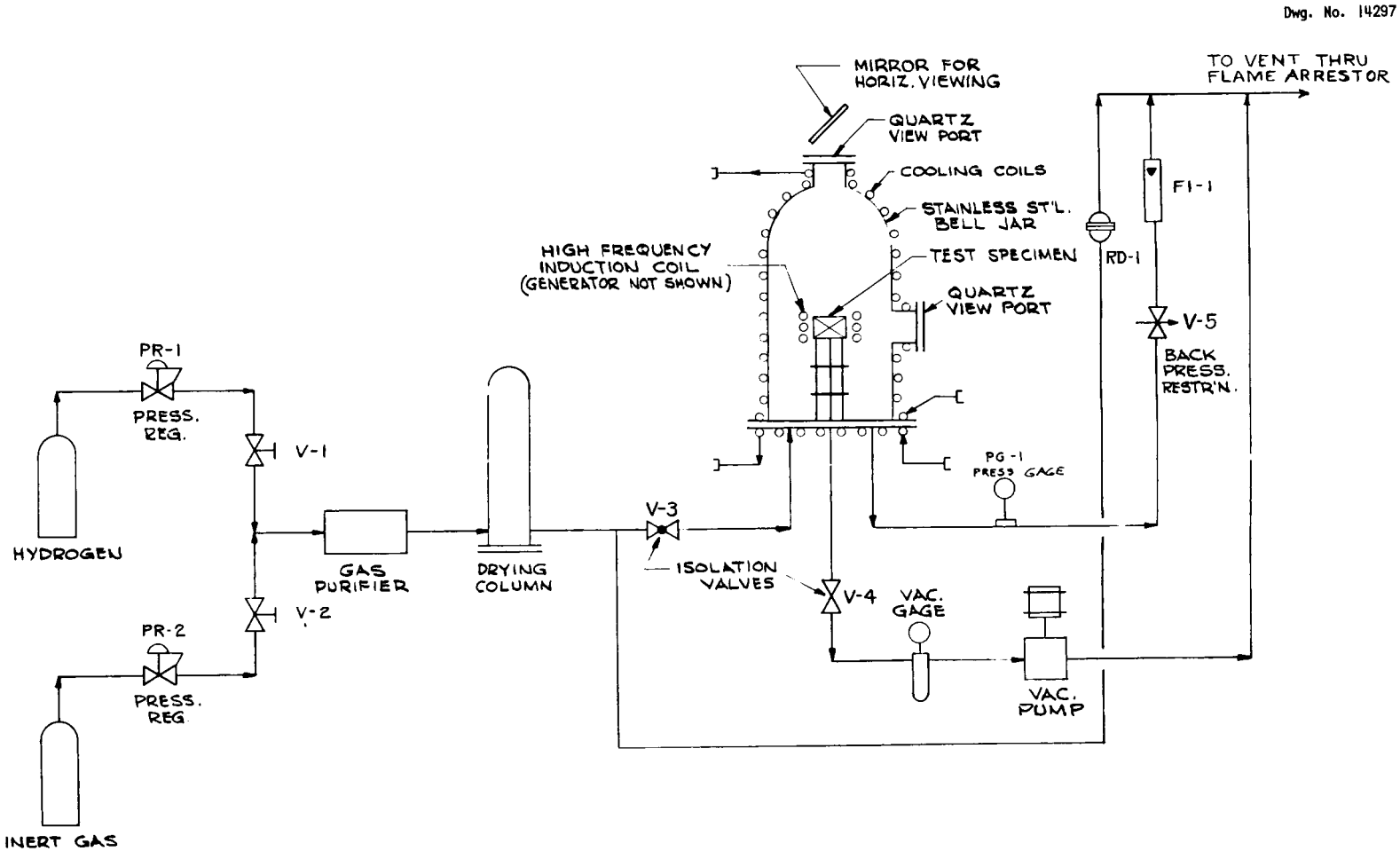

Fig. 7 — Hydrogen thermal conductivity apparatus – schematic

The test chamber, fabricated at UNC, is a stainless steel bell jar (10-in. diameter and 20-in. high) designed for minimum working pressure of 150 psia. The bell jar is bolted to the base plate located on the bell jar table. Double O-rings are used as a pressure seal between the bell jar and base plate. A counterbalance system on the bell jar table facilitates raising and lowering the 220-lb bell jar.

Two viewing ports are provided in the bell jar to permit observation of the upper circular surface and the vertical cylindrical surface of the cylindrical test specimen as shown in the Bell Jar Assembly (Fig. 8). One-inch-thick quartz windows with double O-ring seals are used in the viewing ports. The windows are calibrated prior to installation to determine their spectral transmissivities. A high-temperature vacuum furnace is used as an isothermal temperature source for these calibration tests. The average transmissivities are 0.909 for the top window and 0.922 for the side window. These values are calculated at temperatures between 1600 and 3800°F using the analysis given in Appendix III. A front surfaced mirror, attached to the upper viewing port, facilitates making temperature measurements of the upper circular surface of the specimen.

Three tungsten specimens, purchased from the Wah Chang Corporation, are shown in Fig. 9. One specimen is a solid-tungsten disc, $1\frac{1}{2}$-in. diameter and 1/2-in. high, which is used to determine the thermal conductivity of solid tungsten. This specimen is certified to be 99.5% dense and 99.8% pure. The remaining two specimens are porous (42%) tungsten and are fabricated by sintering tungsten powder at temperatures close to 5000°F for a long period of time to insure mechanical stability of the resulting porous structure.

The size of the particles used in the specimens (0.006 to 0.010-in. diameter) represents a compromise between two conflicting requirements:

1. The pore size should not be too small in comparison with the mean free path of the gas molecules at the operating temperature and pressure.

Otherwise, noncontinuum effects will cause apparent values of thermal conductivity which are smaller than the true values observed in an enclosure larger than the critical size.

2. The dimensions of the structure should be small in order to reduce the temperature differences enough (between adjacent particles or pores) to eliminate most of the internal radiation; i.e., to provide a large number of radiation shields within the specimen.

According to an analysis presented by Deissler and Eian,[6] the first requirement is satisfied by the particle size used at the operating pressure of 150 psia. The measurements in vacuum at various temperature levels show that the second requirement is also satisfied.

Initially, a 0.040-in. solid-tungsten ring surrounded the porous specimens for mechanical and heating purposes. During test operations, these specimens exhibited poor bonding between the solid ring and the porous body which necessitated the removal of the solid ring before performing additional tests. Both porous specimens were 1/2-in. high and had different diameters of 1 and 1½ in. After removal of the solid ring, the larger specimen became 1.45-in. diameter by 0.500-in. high and the smaller specimen became 0.975-in. diameter by 0.375-in. high. These porous specimens (without solid rings) were used to determine the thermal conductivity of hydrogen. A trial porous tungsten specimen (1½-in. diameter by 1/2-in. high) was used in early tests. This specimen had a porosity of 55% and was sintered from tungsten powder of unknown size and purity.

A tripod, made from pointed 1/8-in. tungsten rods inserted in a Mycalex base, is used to support the specimens inside the bell jar as shown in Fig. 10.

Temperature measurements on the upper circular surface of the specimen are made with a micro-optical pyrometer (Model No. 95) purchased from the Pyrom-

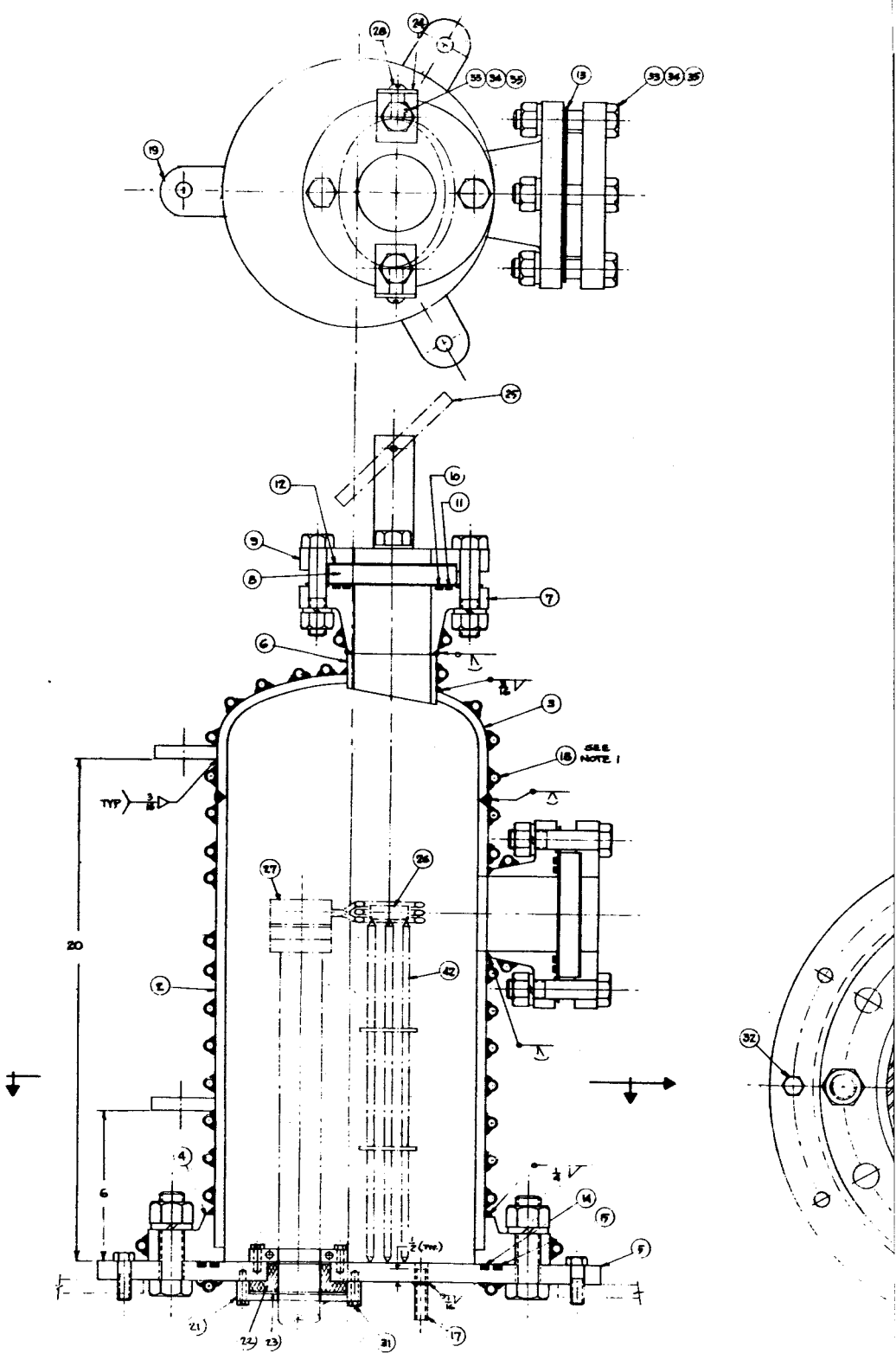

① BELL JAR ASSEMBLY

Dwg. No. 14276

PARTS LIST FOR DWG. NO. 14276

ITEM NO.	SHOWN ON DWG. NO.	QTY.	DESCRIPTION	MATERIAL	USED ON DWG. NO.
1	14276	1	BELL JAR ASSEMBLY		4276
2	14277	1	BARREL		
3	14278	1	CAP		
4	14276	1	10" I.P.S. SOCKET WELD FLANGE	304 S.S.	
5	14279	1	BASE PLATE		
6	14280	1	NIPPLE		
7	14281	2	VIEWING PORT FLANGE		
8	14276	2	WINDOW 5" DIA x 1" THICK	QUARTZ	
9	14282	2	COVER PLATE		
10	14276	2	O RING PARKER NO 5427-44	NEOPRENE	
11	14276	2	O RING PARKER NO 5427-90	NEOPRENE	
12	14276	2	GASKET 5" O.D. x 4" I.D. x 1/16 THK	NEOPRENE	
13	14283	2	GASKET		
14	14276	1	O RING PARKER NO 5427-77	NEOPRENE	
15	14276	1	O RING PARKER NO 5427-73	NEOPRENE	
16	14276	1	1 1/4" SCHED 40 PIPE 2" LG.	304 S.S.	
17	14276	2	1/4" SCHED 40 PIPE 2" LG.	304 S.S.	
18	14276	AR	COOLING COIL 1/4" O.D. x .049 WALL	COPPER	
19	14284	6	LIFTING LUG		
20	14285	1	TOP SEAL COLLAR		
21	14286	1	BOTTOM SEAL COLLAR		
22	14276	1	SEAL (LEPEL H.F. LABS.)	RUBBER	
23	14276	1	SPLIT WASHER 3/4 O.D. x 1/2 I.D. x 1/16 THK	304 S.S.	
24	14287	2	MIRROR BRACKET		
25	14288	1	MIRROR		
26	14276	1	SPECIMEN 1/2 DIA x 1/2 THK.	TUNGSTEN	
27	14276	1	HEATING COIL ASSY (LEPEL)		
28	14276	2	NO 12-24 NC RD HD MACH SC 3/4 LG	304 S.S.	
29	14276	4	1/4-20 NC HEX HD CAP SCR. 3/4 LG.	304 S.S.	
30	14276	2	1/4-20 NC HEX HD CAP SCR. 2 1/2 LG.	304 S.S.	
31	14276	4	1/4-20 NC HEX HD CAP SCR. 1" LG.	304 S.S.	
32	14276	12	3/8-16 NC HEX HD CAP SCR. 1 1/2 LG.	304 S.S.	
33	14276	8	3/8-16 NC HEX HD BOLT 4 LG.	304 S.S.	
34	14276	8	3/8-16 NC HEX NUT	304 S.S.	
35	14276	8	3/8" LOCKWASHER	302 S.S.	
36	14276	10	1/2-13 NC HEX HD BOLT 3 1/16 LG. (MIN.)	304 S.S.	
37	14276	10	1/2-13 NC HEX NUT	304 S.S.	
38	14276	10	1/2" LOCKWASHER	302 S.S.	
39	14276	2	1"-8 NC HEX HD BOLT 3 1/16 LG. (MIN.)	304 S.S.	
40	14276	2	1"-8 NC HEX NUT	304 S.S.	
41	14276	2	1" LOCKWASHER	302 S.S.	
42	14290	1	TEFLON ASSEMBLY		

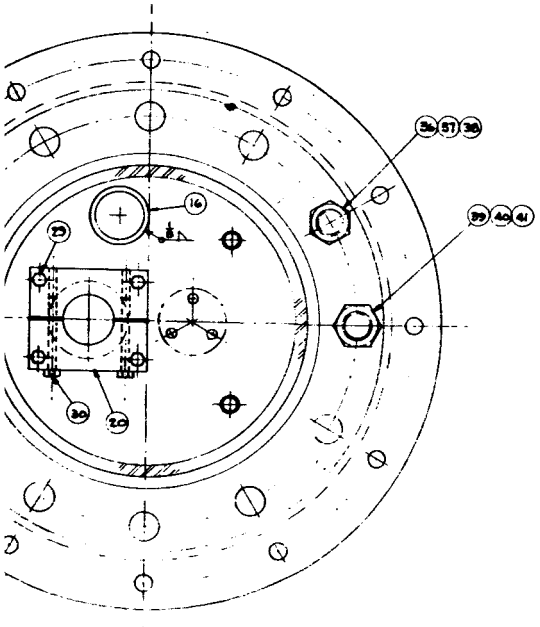

NOTES:

1. COOLING COIL (18) TO BE SILVER SOLDERED TO BELL JAR WITH A CONTINUOUS FILLET OF 1/8 x 1/8 (MIN.) AND A MAXIMUM PITCH OF 1".

Fig. 8 — Bell jar assembly

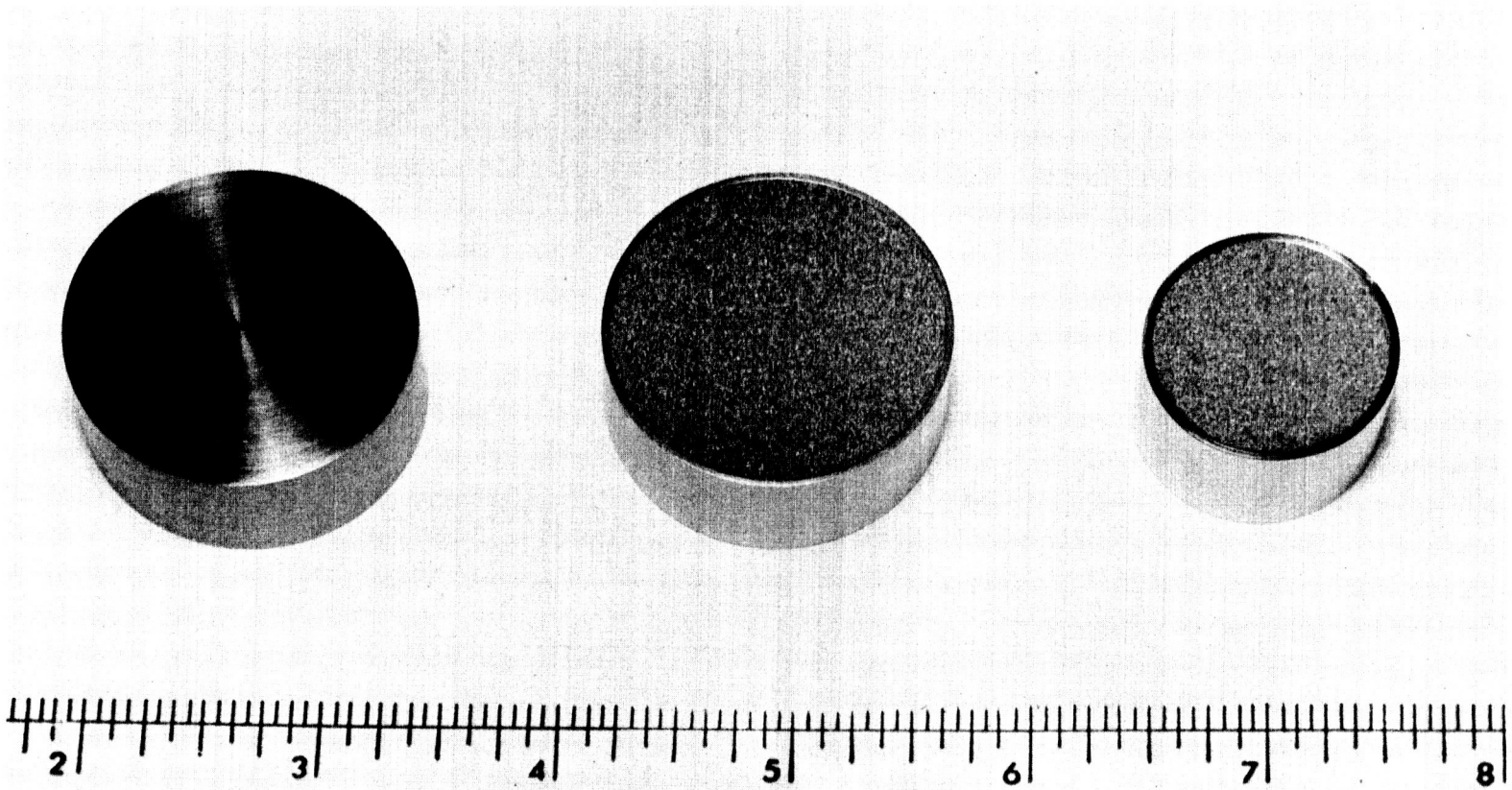

Neg. No. 4483

Fig. 9 — Tungsten test specimens

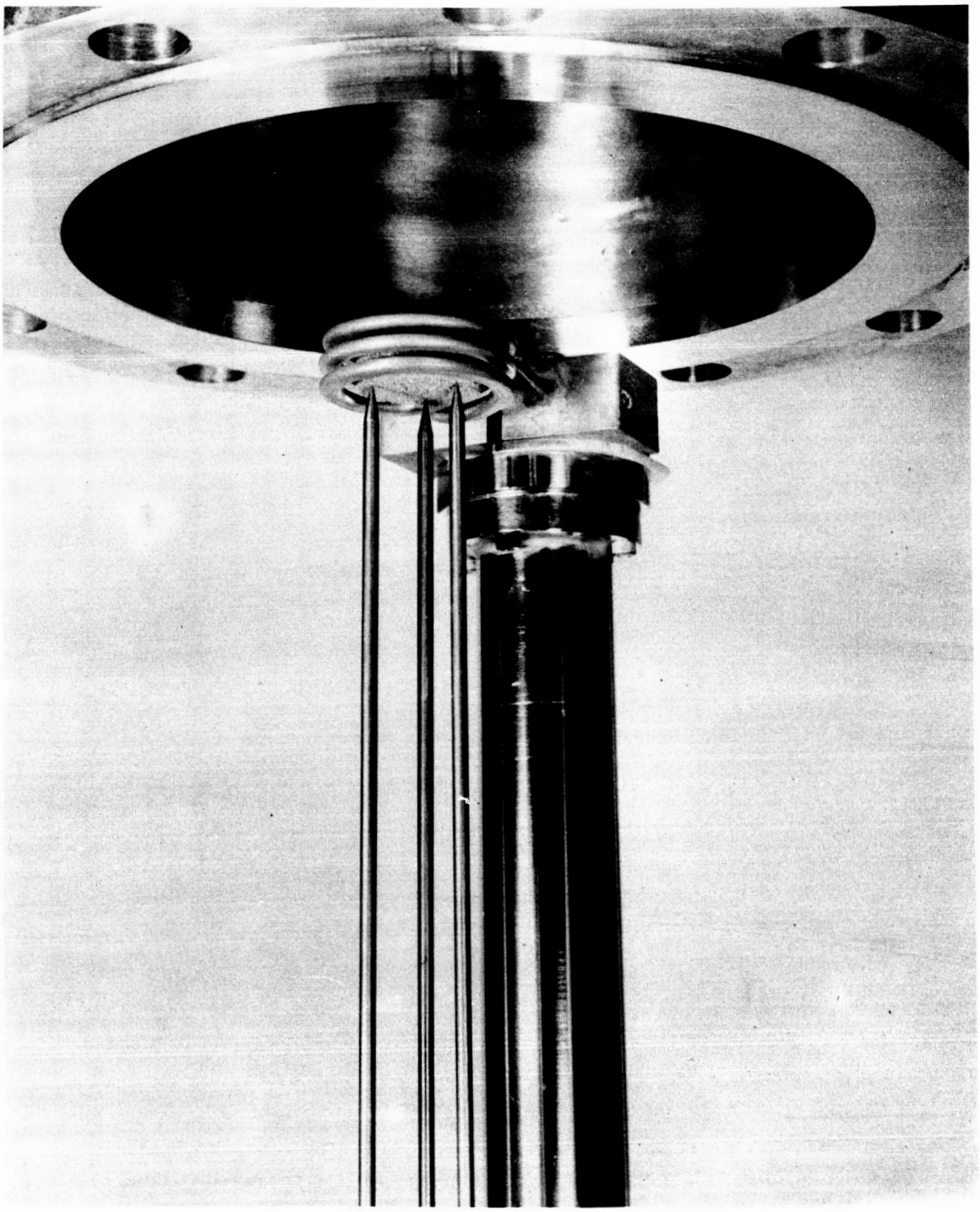

Neg. No. 4482

Fig. 10 — Tungsten specimen located inside test chamber

eter Instrument Company. A certificate of calibration provided with the instrument indicates an uncertainty of ±10° at 3200°F and ±18° at 4500°F. A pyrometer mount has been fabricated to provide a sturdy platform for making temperature measurements. A circular milling table, attached to the pyrometer mounts, permits positioning of the disappearing filament in the pyrometer along two mutually perpendicular diameters of the upper circular surface of the specimen.

The cooling coils, attached to the bell jar and base plate, provide an estimated maximum temperature of 160°F at the inside wall of the bell jar. These cooling coils are connected to a 10 gpm water supply.

The atmosphere inside the test chamber, whether vacuum or pressurized gas, is controlled through ports located in the base plate on the bell jar table. A 1½-in. ball valve and a thermocouple-type vacuum gage are located between the vacuum port and the mechanical vacuum pump. The vacuum gage, manufactured by NRC Equipment Corporation, permits measurement down to 1 micron Hg. The mechanical pump is a Welch No. 1402 and has a rated pumping speed of 80 liters per minute at 1 micron Hg. The vacuum system is vented through a flame arrester on the roof of the building to minimize the hazards when evacuating hydrogen from the test chamber.

The vacuum system is isolated by the 1½-in. ball valve during pressurized gas operation as shown in Fig. 7. Commercially available cylinders of helium and hydrogen were used for pressurized gas operations. A catalytic gas purifier and chemical dryer, located downstream of the gas supply, increase the purity of the gas atmosphere. A Bourdon tube-type pressure gage and a throttle valve are located downstream of the bell jar to permit control of the pressure in the test chamber. The gas is exhausted through a low-flow rotometer to the roof vent. A 160-psig rupture disc connected to the vent line protects the gas system and bell jar from overpressure.

4.2 TEST PROCEDURE

The test specimen was placed on the tripod and centered in the load coil located inside the test chamber. A three-turn 1¾-in. ID load coil was used for the 1½-in. diameter specimen, and a three-turn 1¼-in. ID load coil was used for the 1-in. diameter specimen. All specimens were baked out for one day at temperatures above 3000°F before making temperature measurements. Only the trial porous specimen had an appreciable amount of volatile impurities. The solid tungsten specimen was polished to a mirror finish before installation in the test chamber.

When performing tests under pressure, the porous specimen was first heated in a vacuum of approximately 10 microns Hg to 2300°F to drive off any residual gases remaining in the pores. The system was then pressurized with the desired gas to 150 psia. The test chamber was evacuated to about 5 microns Hg before temperature measurements under vacuum were made. The test sequence was to perform all the tests in vacuum first, then in helium, and finally in hydrogen. Data were generally obtained at successively higher temperature levels in each atmosphere except for several instances where additional data were obtained at a later date at intermediate temperature levels.

The test specimen was heated at constant power for 20 to 30 minutes to insure steady-state conditions before making temperature measurements. Two temperature measurements were made at five locations on each of three radii of the upper circular surface of the specimen as indicated in Fig. 11. One measurement was made by decreasing, and the other was made by increasing filament brightness of the optical pyrometer. The arithmetic average of these two readings was used as the temperature at each point.

The surface of the solid tungsten specimen appeared uniform in brightness when viewed through the optical pyrometer. The surface of the porous specimen had a mottled appearance due to a difference in brightness of the grains and pores along

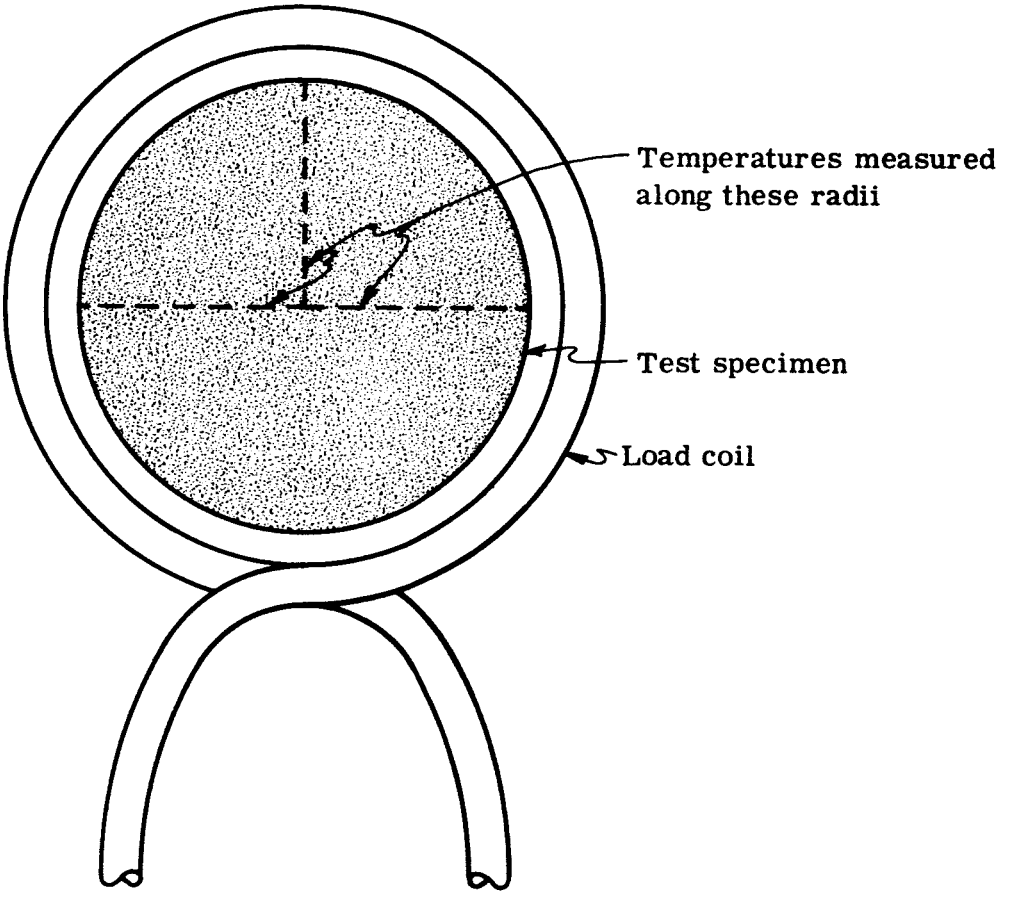

Fig. 11 — Location of temperature measurements on test specimen

the surface. This difference in brightness is due mainly to a difference in effective emittance between the pores and grains (the pores have a higher effective emittance and, therefore, a brighter appearance). The filament in the pyrometer was matched to the pore brightness for all the temperature measurements on the porous specimens. Thermal convection currents in pressurized gas operation caused some shimmer in the appearance of the porous specimen when viewed through the optical pyrometer; however, the temperature data for the porous specimens in gas appear to have the same reproducibility as the data for the same specimens in vacuum.

4.3 EXPERIMENTAL DATA

More than 150 temperature distributions (measured on the upper circular surface) were obtained for the solid and porous tungsten specimens in vacuum, helium, and hydrogen at average temperatures to 4700°F.

The actual data recorded were brightness temperatures measured with the optical pyrometer. The true temperatures were related to the brightness temperatures by the spectral emittance (at $\lambda = 0.65\,\mu$) and the spectral transmissivity of the quartz window. Wien's formula was used to reduce all observed brightness temperatures to true temperatures as shown in Appendix III. The spectral emissivities used for solid tungsten are given in Appendix III. These were obtained from References 8 and 9 which are in good agreement.

There is a disagreement in the published literature on the spectral emittance of porous tungsten. References 9 and 10 indicate an emittance of about 0.4, but there is scatter and an undefined dependence on porosity. Reference 11 shows emittances around 0.8, also with a fair amount of scatter. Because of this disagreement, spectral emittances were calculated from the observed temperatures in the porous Wah Chang specimen which is enclosed by a solid tungsten ring. The true temperature in the solid tungsten ring was calculated from the solid tungsten

emissivity data and was assumed to be equal to the temperature of the adjacent porous body so that a spectral emittance for the porous surface could be determined. The resulting average value, $\epsilon_\lambda = 0.58$, was used in the reduction of all the porous specimen temperatures. Uncorrected brightness temperature data for the specimens are given in Appendix IV.

The upper circular surface of the solid tungsten specimen was polished in order that published emissivity data would be applicable. After one day's operation in a vacuum (about 5 microns Hg) at temperatures up to 3600°F, the surface became crackled in appearance though it still retained its original mirror-like qualities and smoothness. This occurrence was the result of thermal etching of the grain boundaries. This specimen was repolished several times during operations to maintain its surface finish. During operation with the solid specimen, temperatures were measured along the vertical cylindrical surface. These measurements showed no measurable temperature gradient over this surface. A typical temperature distribution on the upper circular surface of the solid tungsten specimen in vacuum is shown in Fig. 12.

Initial temperature measurements on the 1½-in. porous Wah Chang specimen surrounded by a solid tungsten ring showed a strong asymmetry in the temperature distribution over the upper circular surface. There was a sharp temperature decrease between the solid ring and porous body at two opposing interfaces while no such interfacial temperature difference was noted on the diameter perpendicular to the first. This asymmetry was caused by poor bonding between the solid tungsten ring and the porous body. Consequently, the solid tungsten ring was removed before further testing. The data obtained without the solid ring showed good temperature symmetry.

Temperature distributions for tests in vacuum and hydrogen are shown in Figs. 13 and 14, respectively. Comparison of the temperature distributions for porous and

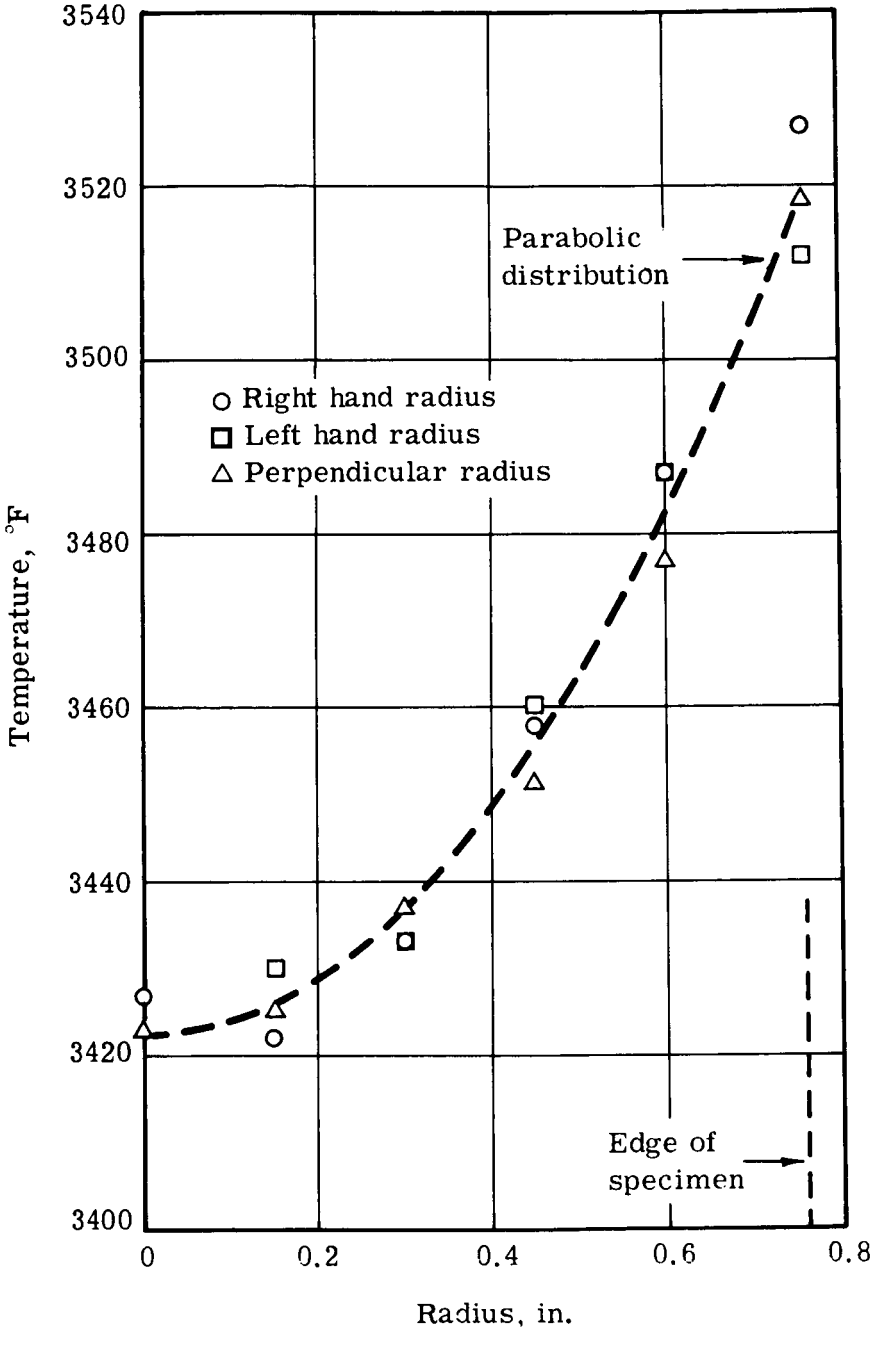

Fig. 12 — Temperature distribution for $1\frac{1}{2}$-in. solid tungsten specimen in vacuum

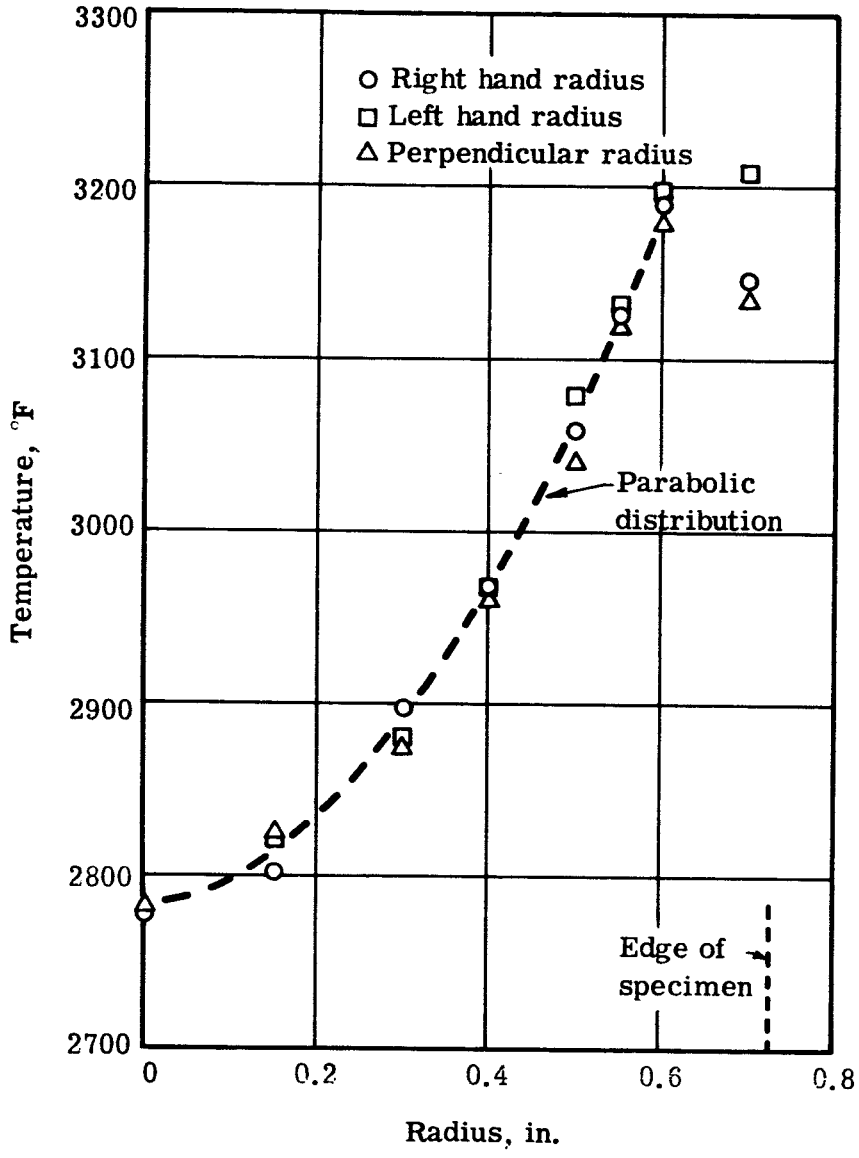

Fig. 13 — Temperature distribution for 1½-in. porous tungsten Wah Chang specimen in vacuum

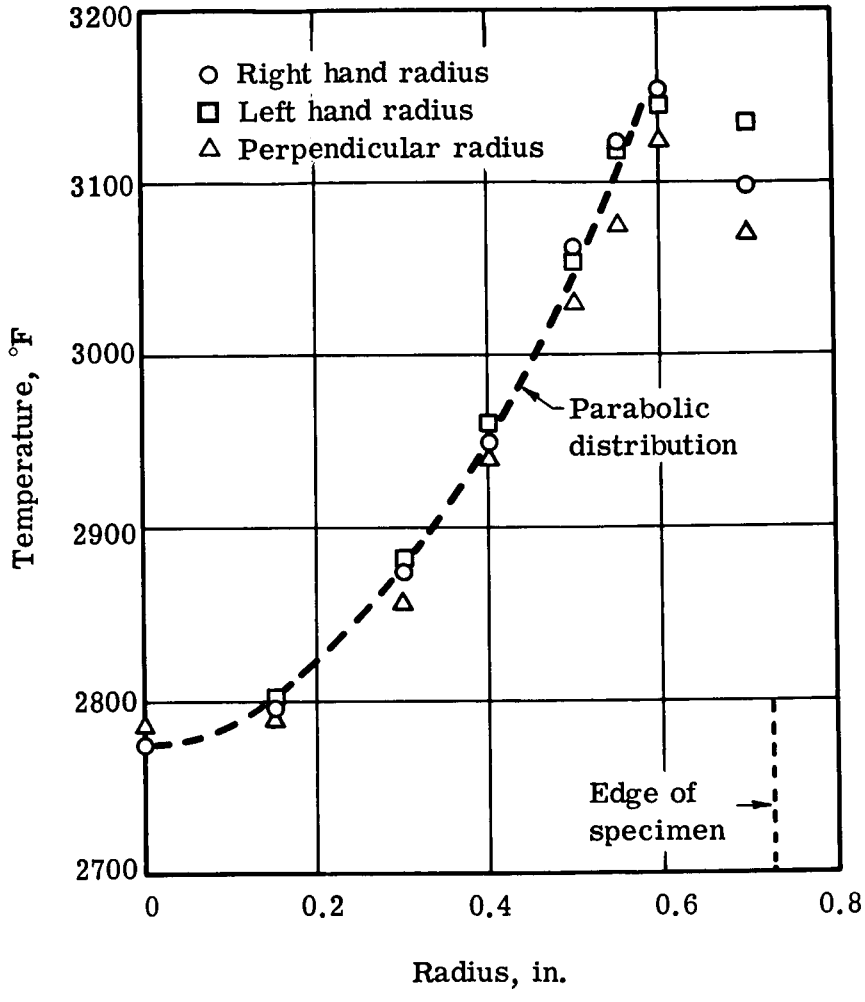

Fig. 14 — Temperature distribution for 1½-in. porous tungsten Wah Chang specimen in hydrogen (150 psia)

solid tungsten specimens in vacuum show the temperature peaking at an inner radius of the upper surface of the porous specimen, while the peak temperature is at the outer radius of the solid specimen. This effect is caused by a greater induction heating depth due to the high electrical resistance of the porous structure.

A complete set of temperature distribution data was obtained with the 1-in. Wah Chang specimen before evidence of poor bonding between the solid tungsten ring and porous body was noted. These data were subsequently discarded because of unreasonable trends and a second set of data was obtained with this specimen after the solid ring was removed. These later data were the only data from this specimen used to determine hydrogen thermal conductivity.

Data were obtained for the 1½-in. porous trial specimen at relatively low temperatures. When further high temperature tests were performed, an internal void was caused by a crack in the specimen. This prevented obtaining additional data with this specimen.

5. ANALYSIS OF EXPERIMENTAL DATA

The thermal conductivity of the cylindrical specimens is determined from the heat flux at the center of the upper circular surface and the axial centerline temperature gradient. The observed temperature distribution on the upper circular surface of the specimen provides an empirical boundary condition for solution of the partial differential equation for the temperature distribution within the specimen:

$$\frac{\partial^2 T}{\partial r^2} + \frac{1}{r}\frac{\partial T}{\partial r} + \frac{\partial^2 T}{\partial z^2} = 0$$

This equation does not contain a source term since all of the heating occurs in a very thin layer at the cylindrical surface. The thermal conductivity has been assumed to be uniform throughout the body. The derivative of the solution is used to evaluate the axial temperature gradient at the center of the upper surface.

The experimental data show that induction heating is confined to a thin layer near the surface of the solid tungsten specimen and that no measurable temperature difference occurs over the outer cylindrical surface of this specimen. For this specimen then, the boundary condition is clearly

$$T = T_{R_o} \text{ at } r = R_o$$

The induction heating of the porous tungsten specimens occurs over a greater depth than for the solid specimen. Because the temperature differences are relatively small in this area and the region itself is thin, the above boundary condition

is also considered appropriate for porous specimens provided R_0 is chosen at the interface between the induction heating region and the simple heat conduction region of the central portion of the porous specimen. Examination of the experimental temperature distributions for the porous specimens indicate that the appropriate R_0 is approximately 4/5 of the radius of the porous specimen.

The actual boundary condition on the end surfaces requires satisfying the Stefan-Boltzmann radiation law (in a vacuum, radiation is the only mode of heat loss from the specimen; even in a pressurized gas atmosphere, radiation is the principal mode of heat loss) at every point on the end surfaces. Analytical solutions which satisfy these nonlinear boundary conditions cannot be obtained; therefore, the following procedure is used.

The boundary condition is taken to be the temperature distribution empirically observed on the end surface of the specimen. A survey of the experimental data indicates that some latitude exists in specifying the temperature distribution from the experimental points when the data for the three radii are superimposed. This scatter is attributed to small nonuniformities in the specimens, particularly the porous compacts, and small asymmetries in the induction heating.

At UNC, a digital computer program was written for the CDC-1604-A to fit the best parabolic, cosine, and zero-order Bessel function curve to the experimental data using the method of least squares. The results indicate that the parabolic distribution is best for the majority of cases; however, the root-mean-square deviation of the data is fairly close for all three distributions and amounts to about 10% of the temperature difference across the specimen. This parabolic distribution agrees with the experimental work done by Hoch.[1]

The mathematics of the solution for the temperature distribution in a cylindrical specimen have been carried out in detail by Hoch[1] assuming symmetry, parabolic end face temperature distribution, and uniform temperature over the cylindrical

surface at $r = R_o$. The resulting solution for the temperature distribution is

$$\frac{T - T_{R_o}}{T_o - T_{R_o}} = 4 \sum_{n=1}^{\infty} \left[\frac{1}{\lambda_n^2} \frac{J_2(\lambda_n)}{J_1^2(\lambda_n)} \frac{\cosh \lambda_n \frac{z}{R_o}}{\cosh \lambda_n \frac{L}{R_o}} J_o\left(J_n \frac{r}{R_o}\right) \right]$$

The axial centerline temperature gradient is evaluated by differentiating the above temperature expression with respect to z and setting $r = 0$ and $z = L$, or,

$$\left(\frac{\partial T}{\partial z}\right)_{0,L} = \frac{4(T_o - T_{R_o})}{R_o} \sum_{n=1}^{\infty} \left[\frac{J_2(\lambda_n)}{\lambda_n J_1^2(\lambda_n)} \tanh\left(\lambda_n \frac{L}{R_o}\right) \right] \tag{3}$$

$$= \frac{4(T_o - T_{R_o}) S_o}{R_o}$$

S_o is the sum of the infinite series which is evaluated by Hoch[1] for various values of L/R_o.

5.1 THERMAL CONDUCTIVITY OF SPECIMENS IN VACUUM

The thermal conductivity of a specimen in vacuum is determined by equating the heat conducted to the center of the upper circular surface to the heat radiated away, or

$$-k \left(\frac{\partial T}{\partial z}\right)_{0,L} = \epsilon_T \sigma T_o^4$$

Using the axial centerline temperature gradient evaluated by Eq. 3, the resulting expression for the thermal conductivity of a specimen in vacuum is

$$k = \frac{\epsilon_T \sigma T_o^4}{4(T_{R_o} - T_o) \frac{S_o}{R_o}} \tag{4}$$

The thermal conductivity of solid tungsten is calculated from the data for the 1½-in. solid tungsten specimen using $R_o = 0.76$ in. and $S_o = 0.341$. The total hemispherical emittances, ϵ_T, used for these calculations are shown in Fig. 26. These emittances were obtained from References 8 and 9. The calculated solid tungsten thermal conductivities are shown in Fig. 15 and are in good agreement with values published in Reference 8. The average value of the thermal conductivity for the experimental points is 51.2 Btu/hr-ft-°F with a maximum deviation of 8.4 Btu/hr-ft-°F. There is no definitive change in the experimental conductivities with temperature between 2000 and 5000°F. Other sources of tungsten thermal conductivity do not agree with the values presented in Fig. 15, and vary in range from 100 down to 30 Btu/hr-ft-°F. The effective conductivities of the porous tungsten specimens in in vacuum are calculated from Eq. 3 also. The values of the constants R_o and S_o used for these calculations are as follows:

	R_o(in.)	S_o
1½-in. trial specimen	0.6	0.413
1½-in. Wah Chang (sans solid ring)	0.58	0.388
1-in. Wah Chang (sans solid ring)	0.38	0.42

The total hemispherical emittances, ϵ_T, used for porous tungsten are shown in Fig. 26. These emittances are based on information published in References 9 and 10 which show scatter and an undefined dependence on porosity. Values are chosen at a porosity of 30%, which was the closest to our specimens. The calculated effective conductivities for the three porous specimens are shown in Fig. 16 as a function of the average temperatures of the specimens $(T_{R_o} + T_o)/2$.

The effective conductivities of the porous specimens are lower than the thermal conductivity of their parent material, tungsten. The trial specimen, which has a porosity of 0.55, has a lower effective conductivity than the Wah Chang specimens whose porosities are 0.42. From these results, it can be seen that the effective conductivity of a porous material generally varies inversely with the porosity.

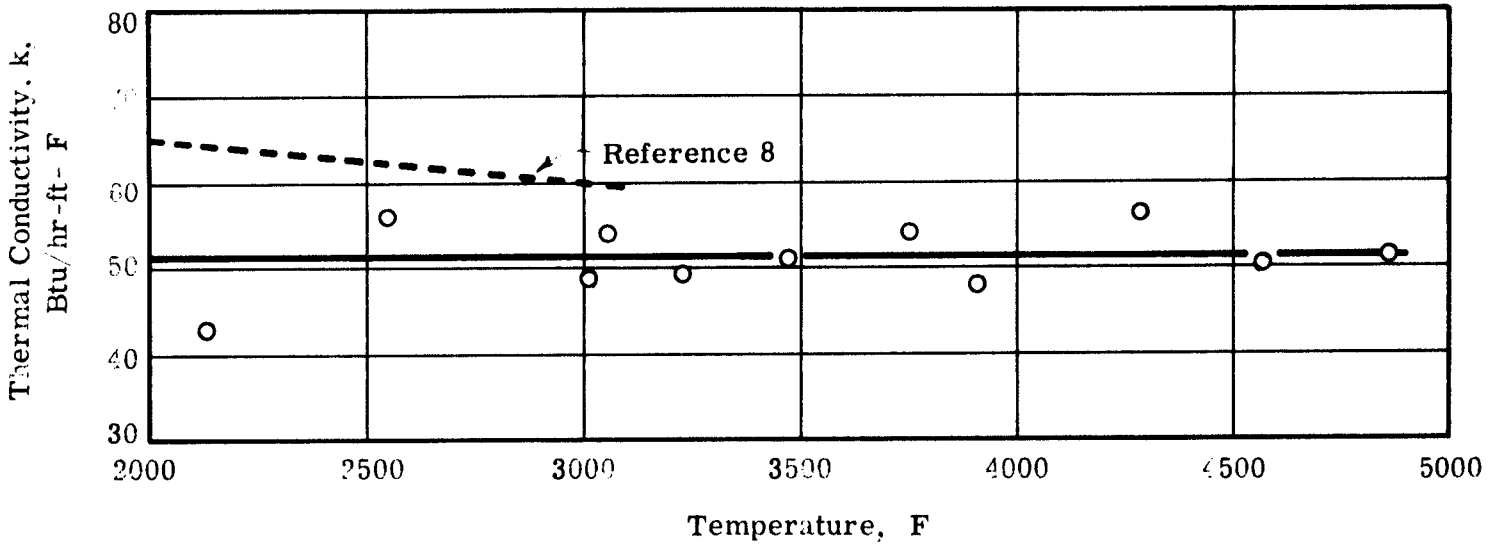

Fig. 15 — Thermal conductivity of solid tungsten

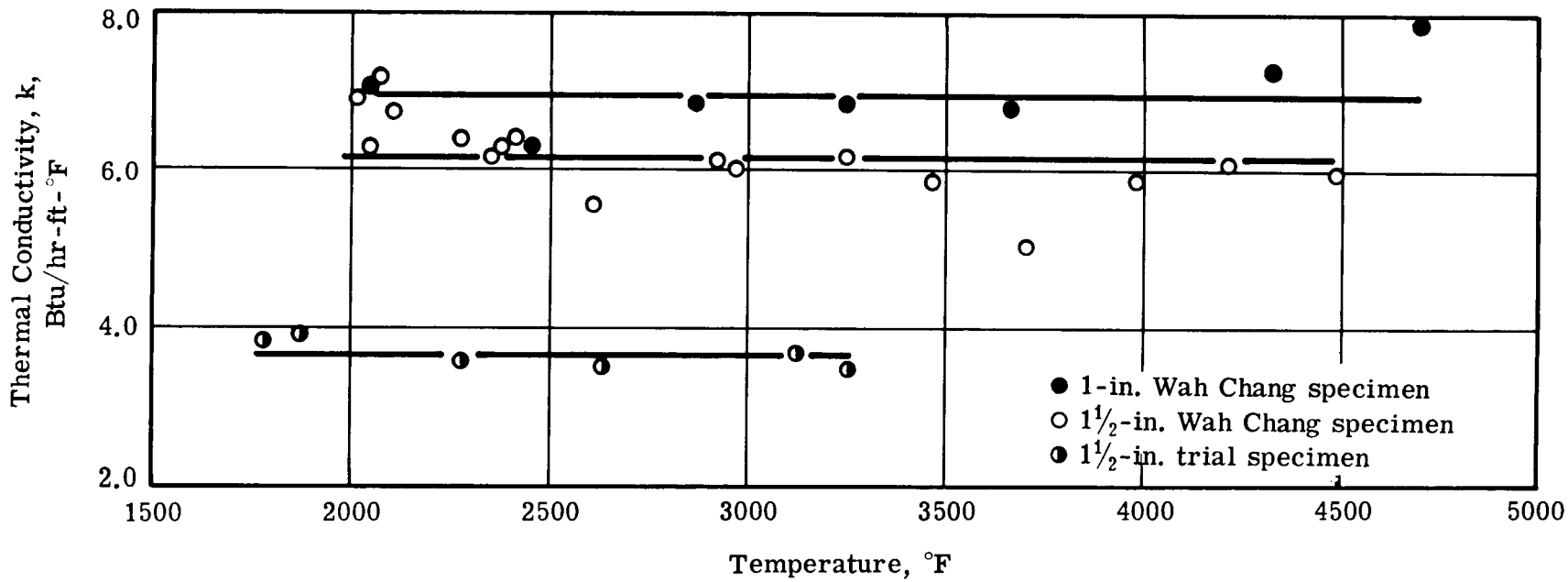

Fig. 16 — Effective thermal conductivity of porous tungsten specimens in vacuum

This effect is not conclusive because possible variations in fabrication also can affect the conductivity as evidenced by the two Wah Chang specimens which have the same porosity but different effective conductivities.

Eq. 1 is a generalized expression derived for the effective conductivity of a simplified model of a porous structure. If the gas conductivity is set equal to zero, this equation reduces to

$$\frac{k_e}{k_s} = \delta + \frac{1 - a - \delta}{(1 - \varphi_g) + \frac{k_s}{\ell h_{rs}}} + a \frac{\ell h_{rp}}{k_s}$$

which is valid for a porous structure in vacuum. It can be seen, by comparing the porous and solid tungsten thermal conductivities, that k_e/k_s does not show any definitive trend to increase with temperature, which would be the case if radiation within the porous structure were important. This result indicates that the effective conductivity of these porous specimens in vacuum is simply related to the contact area between adjacent particles as $k_e/k_s = \delta$.

Data for the 1-in. porous Wah Chang specimen with the solid ring were discarded because the effective conductivities, calculated for this specimen in vacuum, showed a strong trend to decrease with increasing temperature. This effect was strongly contradicted by the data for the other two specimens and also by the data for the 1-in. Wah Chang specimen without the solid ring. The presence of the solid ring was thought to be the cause of these spurious results, but the causal relationship was not determined.

5.2 EFFECTIVE THERMAL CONDUCTIVITY OF POROUS SPECIMENS IN A PRESSURIZED GAS ATMOSPHERE

The determination of the effective thermal conductivity of the porous specimens in a pressurized gas atmosphere is similar to that described for the specimens in vacuum except for the effect of thermal convection on the heat flux from the speci-

men. The resulting expression for the effective thermal conductivity is

$$k_e = \frac{\epsilon_T \sigma T_o^4 + q_c}{4(T_{R_o} - T_o)\frac{S_o}{R_o}} \tag{5}$$

where q_c is the heat flux due to thermal convection at the center of the upper circular surface.

Temperature distribution data obtained for the 1½-in. diameter solid tungsten specimen are used to estimate the thermal convection heat flux at the center of the upper circular surface of the specimens. Since the thermal conductivity of the solid tungsten is not affected by the environment, the conductivities of solid tungsten, calculated by Eqs. 3 and 4, can be equated to yield

$$q_c = \epsilon_T \sigma T_o^4 \left[\frac{(T_{R_o} - T_o) \text{ in gas}}{(T_{R_o} - T_o) \text{ in vacuum}} - 1 \right]$$

Thermal-convection heat fluxes, calculated by the above equation, are shown in Fig. 17 as a function of specimen center temperature.

The thermal convection correlation for spheres and cubes, which was developed by King and reported in Jakob,[12] is used to correlate these experimental data for short cylinders. King's correlation, for the range of Rayleigh Numbers of interest, is of the usual form

$$\frac{hD}{k} = C_1 \left[\frac{g\rho^2 D^3 \beta \Delta T}{\mu^2} \times \frac{C_p \mu}{k} \right]^{1/4}$$

where C_1 is a correlating constant. Because of the close proximity of the load coils to the specimen, this correlating constant is smaller for these data than for "freely" suspended spheres and cubes. Heat fluxes, predicted by the above correlation, use two different characteristic dimensions (D), namely (1) the diameter

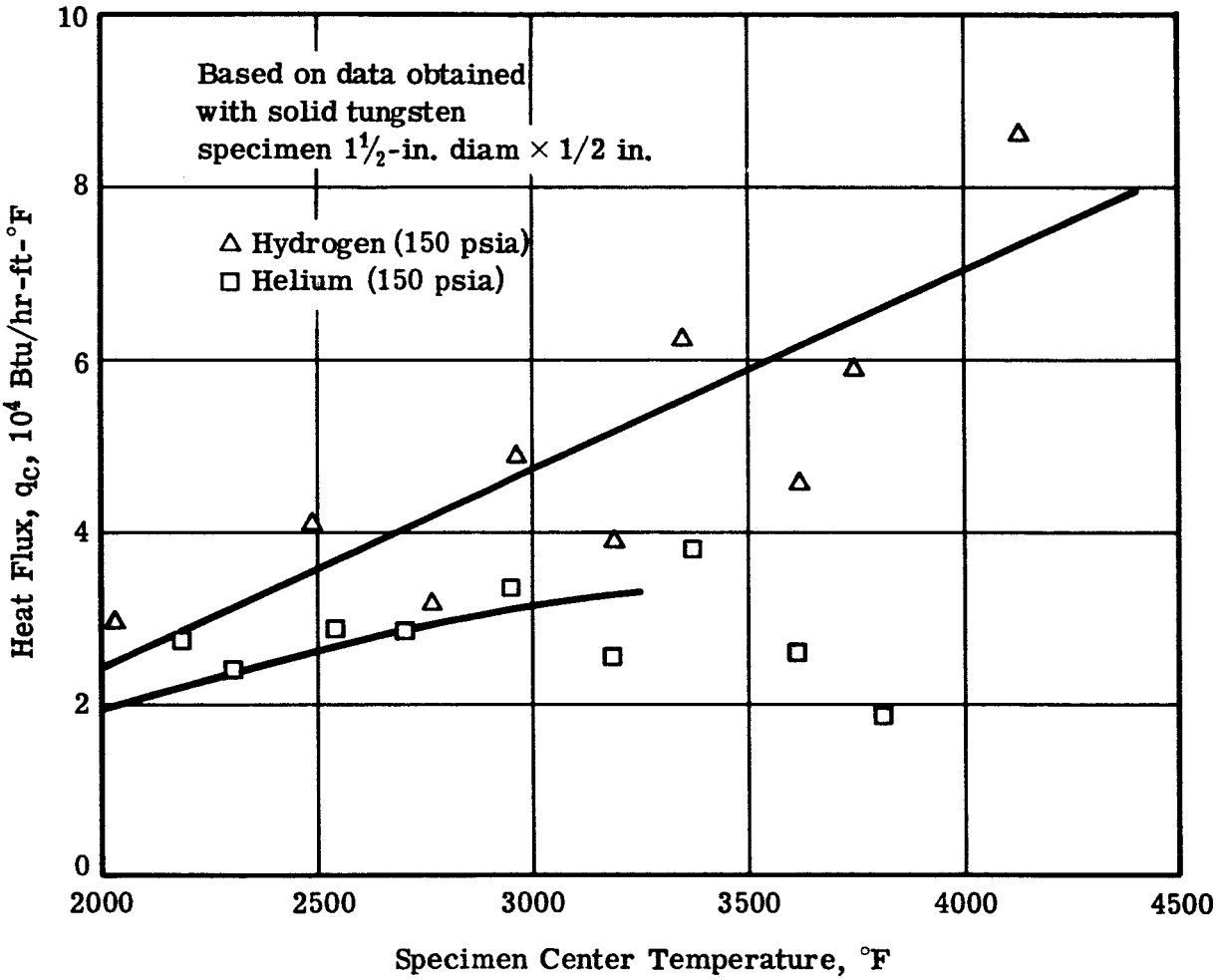

Fig. 17 — Thermal convection heat flux from center of upper circular surface

of the specimen, and (2) the weighted characteristic dimension suggested by King for finite bodies

$$\frac{1}{D} = \frac{1}{\text{Height}} + \frac{1}{\text{Diameter}}.$$

The physical properties used for these calculations are obtained from Reference 2 and 13 and the ambient gas temperature inside the test chamber is assumed to be 200°F. These predicted heat fluxes are fitted to the experimental data for the 1½-in. diameter specimen in Fig. 17 by adjusting the correlating constant. Both characteristic dimensions predict the thermal convection heat flux for the 1-in. diameter specimen to be 15% higher than the heat flux for the 1½-in. diameter specimen. A comparison between the estimated thermal convection heat fluxes (for hydrogen and helium at 150 psia) and radiation from the center of the upper circular surface is shown in Fig. 18. The use of these values to determine the effective conductivities of the porous tungsten specimens in pressurized helium and hydrogen atmospheres is appropriate because the physical properties of the gases and the relative geometries are the same for the porous and solid specimens.

The effective thermal conductivities calculated from the experimental data for the porous specimens in helium and in hydrogen at 150 psia are shown in Figs. 19, 20, and 21. The conductivities are plotted against average specimen temperature, $(T_{R_o}+T_o)/2$. The constants R_o and S_o used in calculating these values from Eq. 5 are the same as the ones used for the vacuum conductivity determinations in Section 5.1.

The porous specimens have measurably higher effective conductivities in a pressurized gas atmosphere than in vacuum. Hydrogen-filled specimens have a higher effective conductivity than helium-filled specimens. This is an effect which is consistent with the published information on the thermal conductivity of hydrogen and helium at these temperatures. There is a definite trend for the specimen conductivities in hydrogen to increase with increasing average specimen temperature.

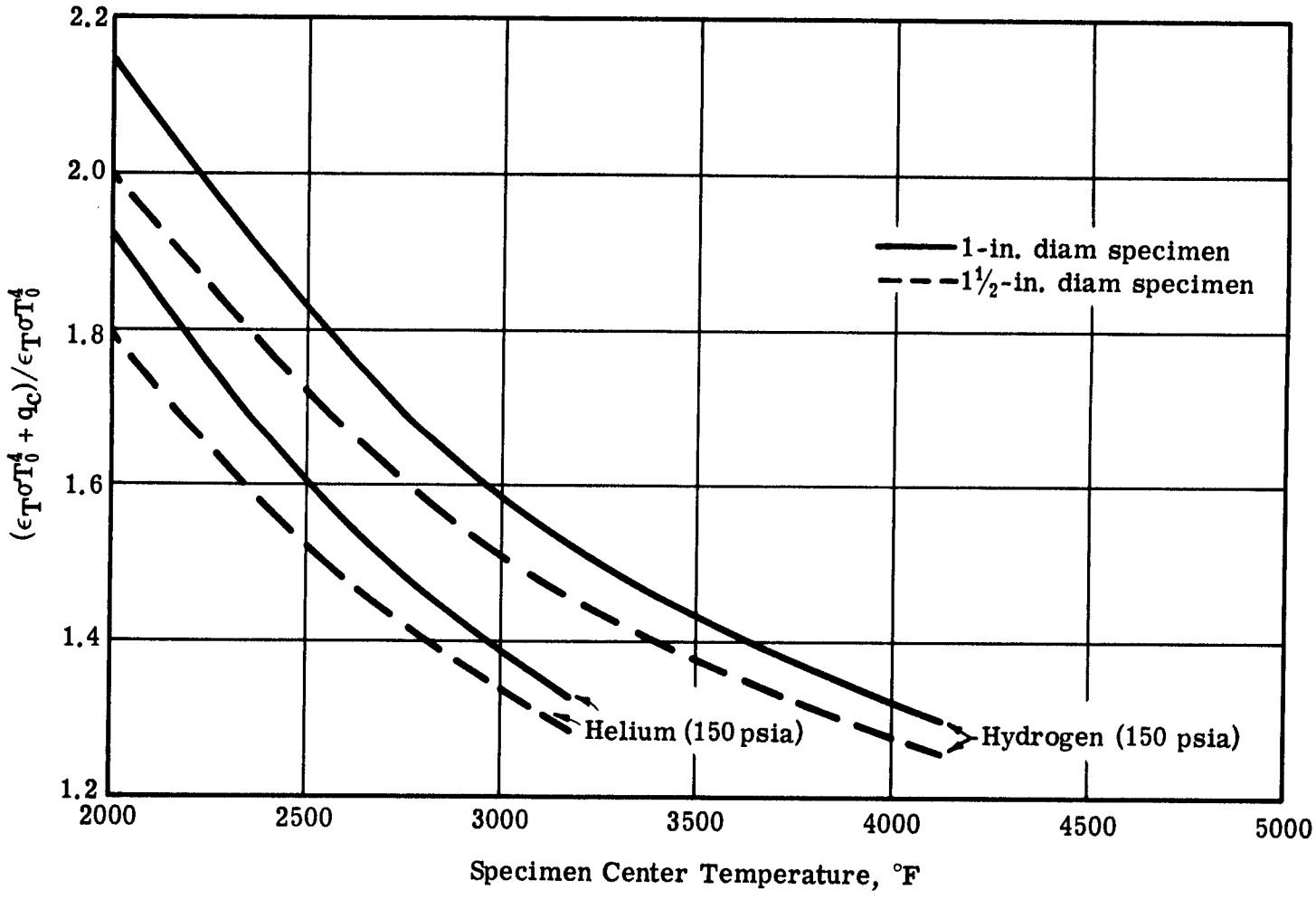

Fig. 18 — Comparison of radiation and thermal convection heat fluxes at center of upper circular surfaces of porous tungsten specimens

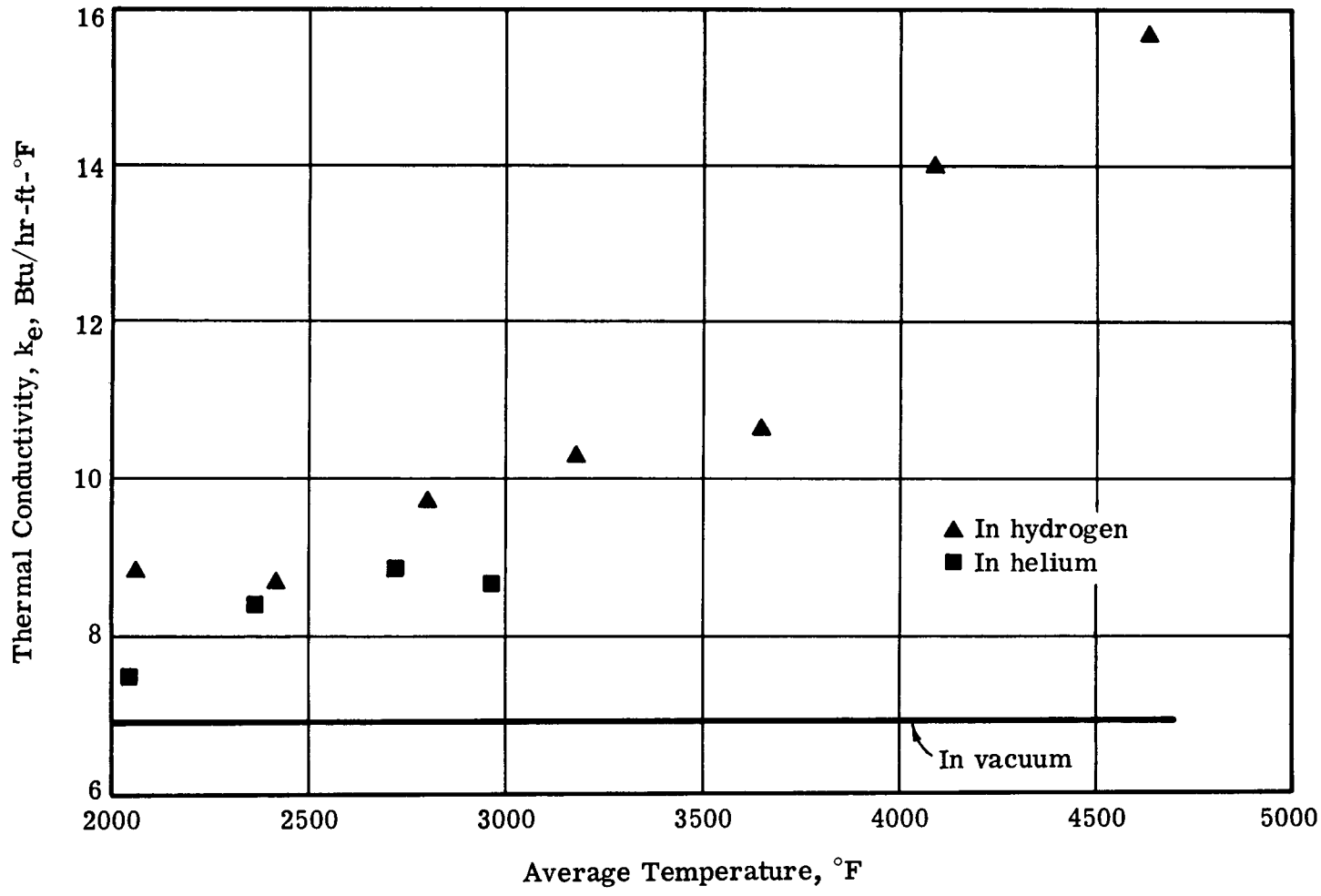

Fig. 19 — Effective thermal conductivity of 1-in. porous tungsten Wah Chang specimen in helium and in hydrogen at 150 psia

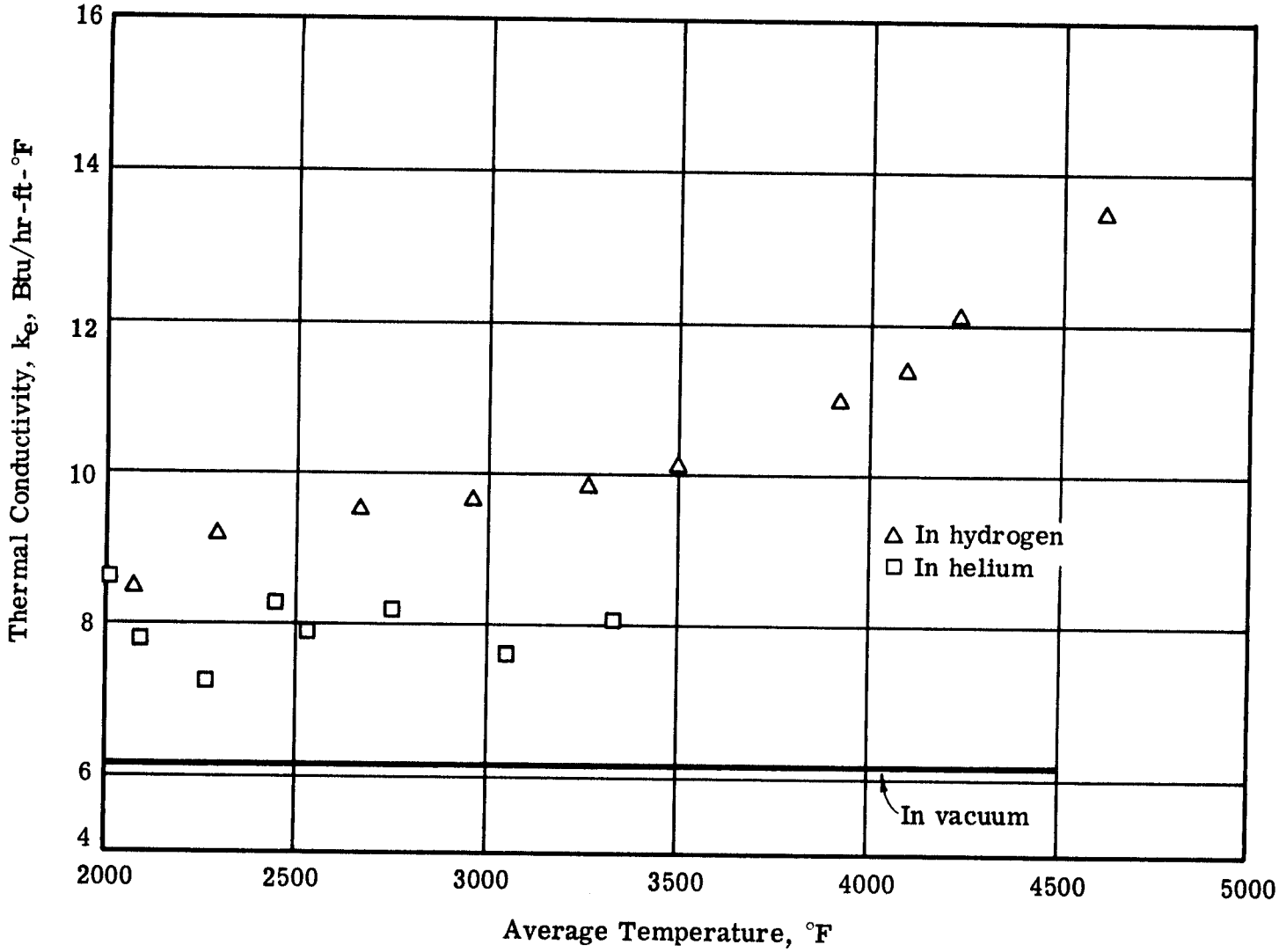

Fig. 20 — Effective thermal conductivity of 1½-in. porous tungsten Wah Chang specimen in helium and hydrogen at 150 psia

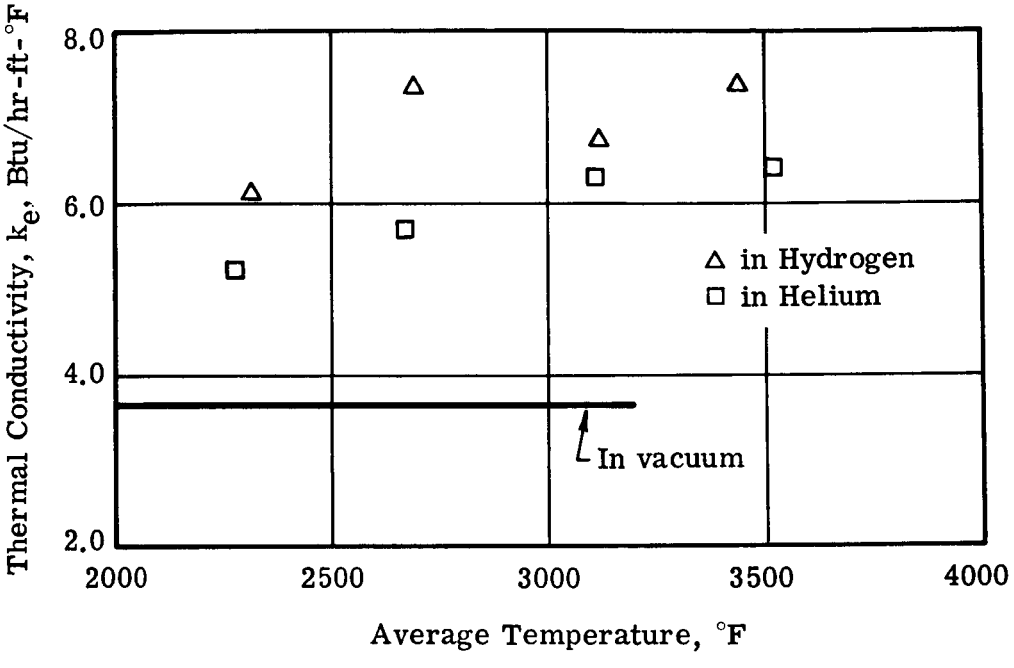

Fig. 21 — Effective thermal conductivity of $1\frac{1}{2}$-in. porous tungsten trial specimen in helium and in hydrogen at 150 psia

This increasing conductivity indicates that the hydrogen thermal conductivity has a demonstrable effect on the specimen because the solid tungsten conductivity is essentially constant at these temperatures.

5.3 COMPARISON OF EXPERIMENTAL DATA WITH RESULTS OF TRUNCATED-SPHERE MODEL

The data-correlation curves shown in Fig. 22 which relate the gas conductivity to the effective conductivity have been established on the basis of an assumed analytical model of the porous structure, plus measured conductivities of the three working specimens in vacuum. Although the use of the particular truncated-sphere model has already been supported by the previous success of other workers[6] with spherical models of unsintered materials, it is interesting to make a more direct comparison of the results of the present model with the available data from another source for hydrogen and helium conductivities in the lower temperature range of the present investigation.

In order to display this comparison graphically, the reported values of gas conductivity at various temperatures have been plotted against the measured effective conductivities of the specimens at the same temperatures. Both values have been nondimensionalized by means of the value of the conductivity of solid tungsten as measured in the present investigation. The set of points thus obtained, and plotted on Fig. 22, corresponds to the complete set of measured effective conductivities of the three specimens in the temperature range of the available data.

The comparison of the truncated-sphere results with available gas data is made by observing how nearly the plotted points fall on the correlation curves for the three specimens. In general, within the experimental scatter, the points fall rather well on the predicted curves, further justifying the analytical model. The greatest departure from the predicted curves occurs, as expected, for helium with the specimens of large contact area, i.e., the case where the effective conductivity is affected least by the presence of gas.

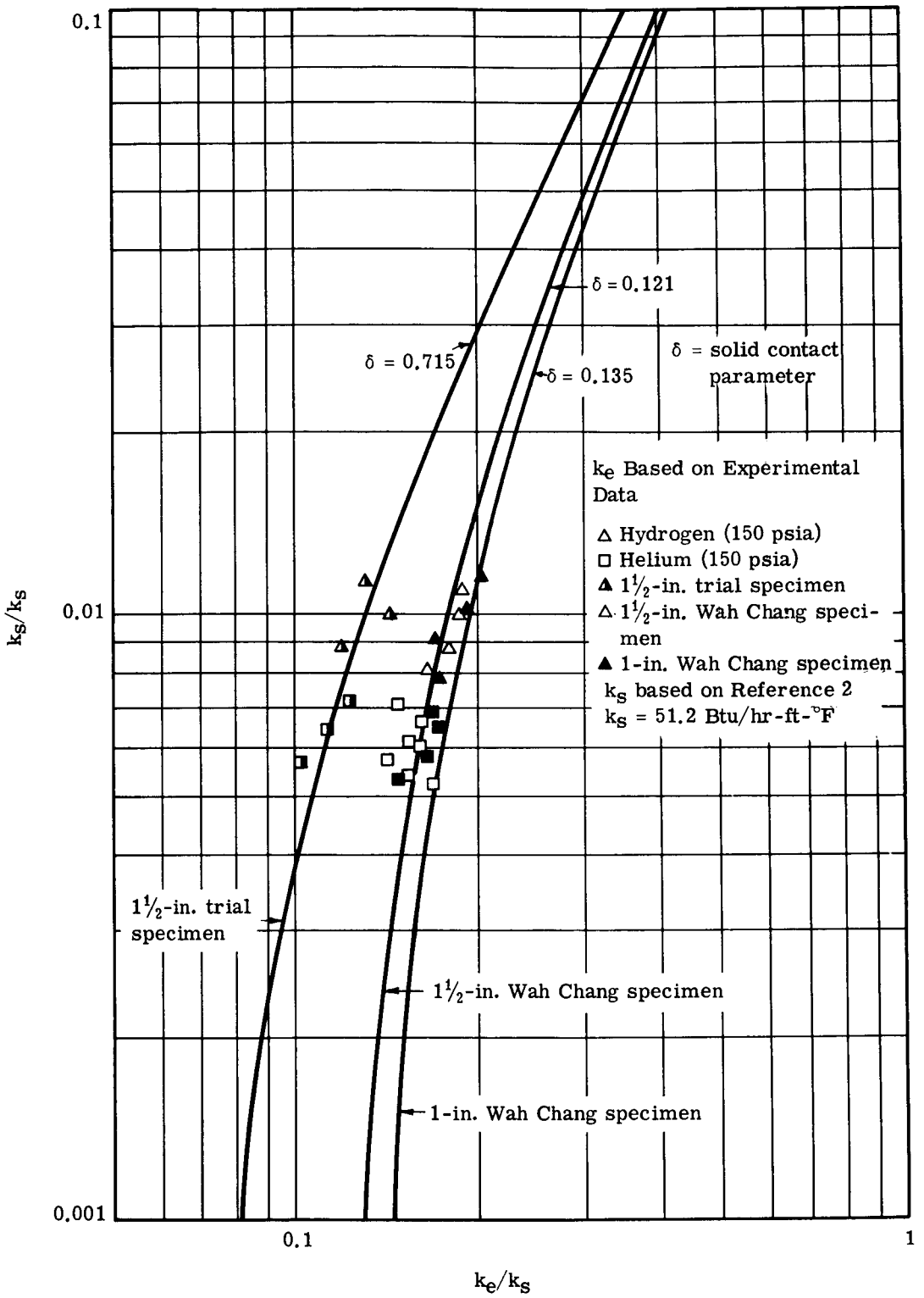

Fig. 22 — Comparison of experimental data and truncated sphere model

6. RESULTS AND DISCUSSION

6.1 THERMAL CONDUCTIVITY OF HYDROGEN AT ELEVATED TEMPERATURES

The thermal conductivity of hydrogen is determined from the effective conductivity data using the truncated-sphere correlation curves shown in Fig. 22. Each correlating curve is determined by the effective conductivity of the porous specimen in vacuum. The effective conductivities, calculated in Section 5.2, for the porous specimens in hydrogen (150 psia) are divided by the thermal conductivity of solid tungsten, 51.2 Btu/hr-ft-°F, to provide values of k_e/k_s. Using the appropriate correlating curve in Fig. 22, the term k_g/k_s can be determined for each value of k_e/k_s calculated from the data. The resulting hydrogen thermal conductivity is plotted in Fig. 23 as a function of the average specimen temperature, $(T_{R_o}+T_o)/2$, at which the data are obtained.

The data for the three specimens are in agreement and show an increasing thermal conductivity with increasing temperature. The upper dashed line in Fig. 23 represents Los Alamos thermal conductivity data[2] for hydrogen at reduced pressures (less than atmospheric) which are used in Fig. 22 to compare the experimental data with the truncated-sphere model. These Los Alamos data are still comparable to our high pressure data because the hydrogen thermal conductivity has not been shown to be pressure sensitive for those temperatures and pressures, except in enclosures of very small dimensions. The lower dashed line represents predicted values of hydrogen thermal conductivity at a pressure of 10 atmospheres. These

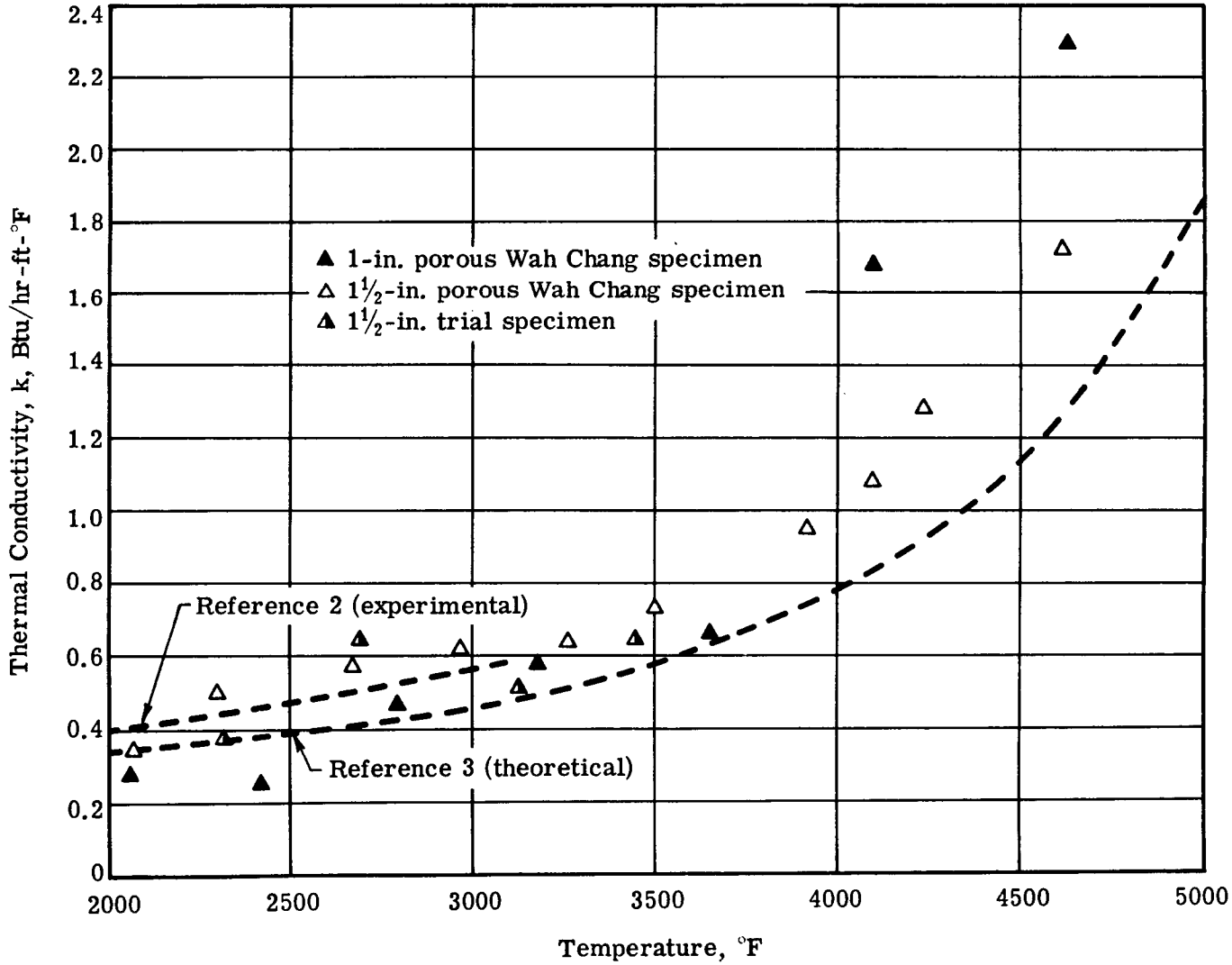

Fig. 23 — Thermal conductivity of hydrogen at 150 psia

predictions, calculated by Grier[3] using kinetic-theory formulas, show a sharp increase in thermal conductivity above 4000°F.

At the lower temperatures, the experimental data fall between the Los Alamos and Grier values, while at higher temperatures, the experimental data are above the Grier predictions. The increase in thermal conductivity with increasing temperature is more pronounced than that predicted by Grier. These comparisons are a reasonable confirmation of our experimentally determined values of hydrogen thermal conductivity at temperatures from 2000 to 4700°F.

6.2 DISCUSSION OF RESULTS AND ERROR ANALYSIS

The values of hydrogen thermal conductivity presented in Fig. 23 are not directly measured, but are the result of a formal calculation procedure. Therefore, the uncertainty of these calculated values is due to cumulative uncertainties. First, the relative uncertainty in the hydrogen thermal conductivity is approximately twice the relative uncertainty in the effective conductivity of the porous specimen in hydrogen as shown by the slope of the correlating curves in Fig. 22. Second, the uncertainties in the calculated effective conductivities are due to random and systematic errors in measured and published information used in these calculations.

Differentiating the equation for effective conductivity in a pressurized gas atmosphere (Eq. 5), it can be shown that

$$\left|\frac{dk_e}{k_e}\right| = \frac{|\sigma T_o^4 d\epsilon_T| + |4\epsilon_T \sigma T_o^3 dT_o| + |dq_c|}{\epsilon_T \sigma T_o^4 + q_c} + \left|\frac{d(T_{R_o} - T_o)}{T_{R_o} - T_o}\right| + \left|\frac{d\,\frac{S_o}{R_o}}{\frac{S_o}{R_o}}\right|$$

Using the comparison of radiation and thermal convection heat fluxes shown in Fig. 18, the above expression reduces to

$$\frac{1}{2}\left|\frac{dk_g}{k_g}\right| \approx \frac{dk_e}{k_e} \approx \frac{1}{1.3}\left|\frac{d\epsilon_T}{\epsilon_T}\right| + \frac{4}{1.3}\left|\frac{dT_o}{T_o}\right| + 0.3\left|\frac{dq_c}{q_c}\right| + \left|\frac{d(T_{R_o}-T_o)}{T_{R_o}-T_o}\right| + \frac{d\left(\frac{S_o}{R_o}\right)}{\frac{S_o}{R_o}}$$

at high temperatures. This equation is used to estimate the uncertainty in the calculated hydrogen thermal conductivity.

The principal sources of random errors are the measurement of temperatures and the procedure for establishing $(T_{R_o}-T_o)$ for each set of data. Two temperature measurements are made at each radial location on the specimen. On the average, there is a 10 to 20 degree difference in these measurements which results in an uncertainty in the center temperature of $|dT_o/T_o| \approx 0.005$. The term $(T_{R_o}-T_o)$ is calculated by a computer code that fit the best parabolic curve to the temperature data. The root-mean-square deviation of the temperature data from the best fit curve was approximately 10% of the term $(T_{R_o}-T_o)$. Assuming that $|d(T_{R_o}-T_o)/(T_{R_o}-T_o)| \approx |d(T_o)/(T_{R_o}-T_o)| = 0.1$, the random uncertainty in the hydrogen thermal conductivity is

$$\left|\frac{dk_g}{k_g}\right| \approx 2\left[\frac{4}{1.3}\ (0.005) + 0.1\right] = 0.23$$

This uncertainty is consistent with the scatter in the thermal conductivity data shown in Fig. 23.

The systematic errors in the hydrogen thermal conductivity calculations are caused by errors in assumed values of spectral and total hemispherical emittances, values of thermal convection heat flux, and boundary condition assumptions that are used for all specimens. Reference 10 shows total hemispherical emittances, ϵ_T, for porous tungsten of 0.375 to 0.36; Reference 9 shows ϵ_T's of 0.3 to 0.375; and Reference 11 shows ϵ_T's ranging from 0.3 to 0.6. The value used for these

calculations is approximately 0.375 (Fig. 26). The most probable uncertainty in this value is 15%. The spectral emittance of porous tungsten was previously discussed in Section 4.3. Because of the way in which the spectral emittance enters into the determination of the true temperature, a 40% error in the assumed spectral emittance results in only a 15% error in the term

$$\left| 4\frac{dT_o}{T_o} - \frac{d(T_{R_o}-T_o)}{T_{R_o}-T_o} \right|$$

which considers the same systematic error in T_o and $(T_{R_o}-T_o)$ and no thermal convection heat flux. Taking the thermal convection heat flux into account and assuming a 40% uncertainty in the spectral emittance results in the following approximation:

$$\frac{4}{1.3}\left|\frac{dT_o}{T_o}\right| + \left|\frac{d(T_{R_o}-T_o)}{T_{R_o}-T_o}\right| \approx \frac{1}{1.3}\left| 4\frac{dT_o}{T_o} - \frac{d(T_{R_o}-T_o)}{T_{R_o}-T_o}\right| = 0.115$$

The uncertainty in the thermal convection correction is approximately 15%. The term (S_o/R_o) contains assumptions used in the solution of the boundary-value problem. Based on Hoch's work,[1] it is estimated that $d(S_o/R_o)/(S_o/R_o) = 0.1$ for the porous specimens which have L/R_o ratios close to 0.5. By way of comparison, it is estimated that $d(S_o/R_o)/(S_o/R_o)$ is less than 2% for the solid tungsten specimen ($L/R_o = 0.34$). These possible systematic errors result in an uncertainty in the absolute level of gas conductivity of

$$\left|\frac{dk_g}{k_g}\right| = 2\left[\frac{1}{1.3}(0.15) + 0.115 + \frac{1}{4}(0.15) + 0.1\right] = 0.74$$

This uncertainty represents the worst possible combination of errors in assumed values for the various parameters. Contemplated additional experimental work directed at the determination of the spectral and total emittances and the thermal convection heat flux should greatly reduce the uncertainty in the calculated values of hydrogen thermal conductivity.

7. APPENDIXES

7.1 APPENDIX I – ANALYSIS OF TRUNCATED-SPHERE MODEL

7.1.1 Derivation of Effective Conductivity Equation

Because of symmetry and the absence of a particle-size effect, the effective conductivity of a cubic array of truncated spheres may be calculated by considering 1/8 of a particle within a unit cube. Applying unit temperature difference makes the effective conductivity equal to the total rate of heat transfer through the cube. This volume is divided into three regions – I Solid conduction, II Series conduction, and III Gas conduction – as shown in two views in Fig. 24. This figure also shows the differential element of volume used in the integration for the series-conduction region (II).

From the figure it is clear that the radius of contact r is related to the relative contact area δ by

$$\delta = \frac{\pi}{4} r^2$$

and that the radius of the sphere R is

$$R = \sqrt{1 + r^2}$$

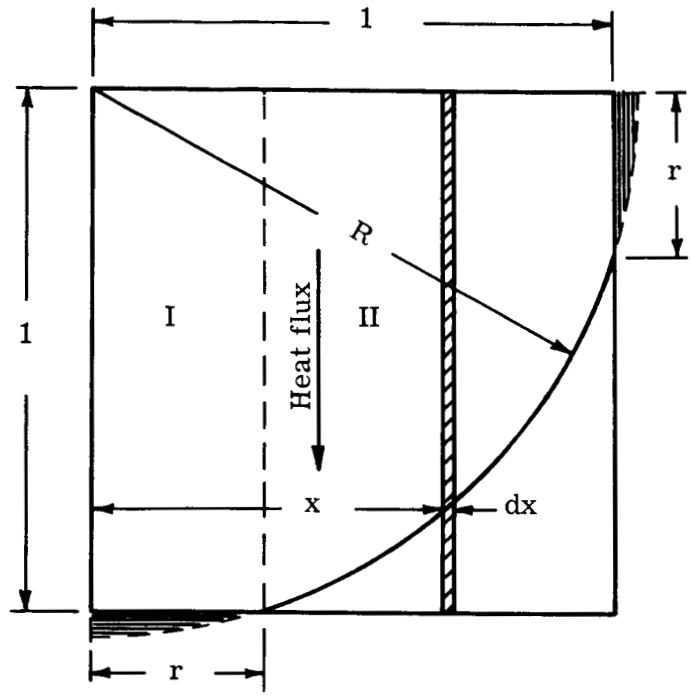

Elevation

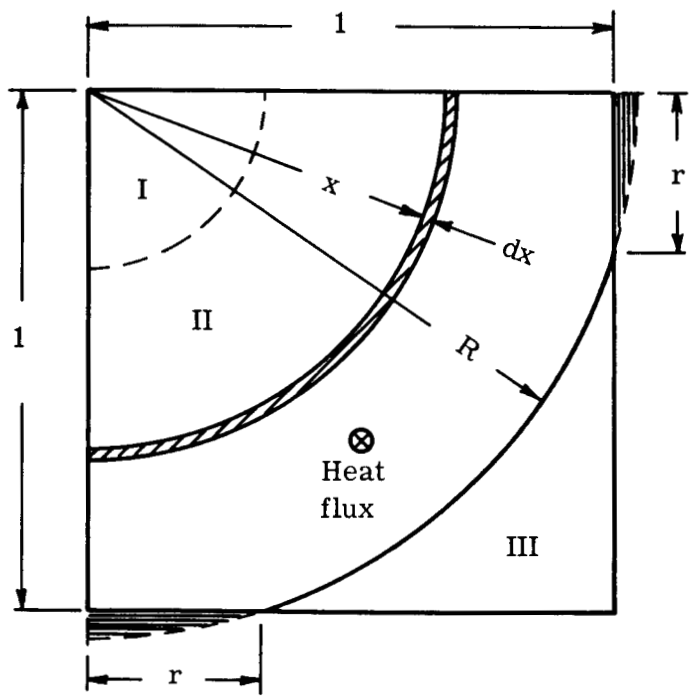

Plan

Fig. 24 — Unit cell for truncated-sphere model

Region I – Solid Conduction

$$q_I = \frac{\pi}{4} r^2 k_s = \delta k_s$$

Region II – Series Conduction

$$r < x < 1: \; dq_{II} = \frac{\pi}{2} k_g \frac{x\,dx}{1 - (1-\beta)\sqrt{R^2-x^2}}$$

$$1 < x < R: \; dq_{II} = \left(\frac{\pi}{2} - 2\tan^{-1}\sqrt{x^2-1}\right) k_g \frac{x\,dx}{1-(1-\beta)\sqrt{R^2-x^2}}$$

$$q_{II} = \frac{\pi}{2} k_g \int_r^1 \frac{x\,dx}{1-(1-\beta)\sqrt{R^2-x^2}} + k_g \int_1^R \frac{\left(\frac{\pi}{2} - 2\tan^{-1}\sqrt{x^2-1}\right) x\,dx}{1-(1-\beta)\sqrt{R^2-x^2}} \quad (6)$$

This term can be evaluated with only a slight error by neglecting the quantity $2\tan^{-1}\sqrt{x^2-1}$, i.e., by extending the integration through the shaded region outside the unit cube, as though the sphere were not truncated at the side contacts. Because of the three-dimensional geometry, the excess volume included is very small; furthermore, the thickness of the gas layer is greatest in this region, so that the error incurred is very small except for a gas with extremely high conductivity. The heat flux in region II is then given by the integral

$$q_{II} = \frac{\pi}{2} k_g \int_r^R \frac{x\,dx}{1-(1-\beta)\sqrt{R^2-x^2}} \quad (7)$$

which can be evaluated by making the substitution $u = \sqrt{R^2-x^2}$ to yield the form

$$q_{II} = \frac{\pi}{2} k_g \int_0^1 \frac{u\,du}{1-(1-\beta)u} = \frac{\pi}{2} k_g \left[\frac{1}{(1-\beta)^2} \ln \frac{1}{\beta} - \frac{1}{1-\beta}\right] \quad (8)$$

It is interesting to note that this result is exactly the same as that obtained by Deissler and Eian[6] for the series-conduction region of untruncated spheres. Mathematically, the definite integral (Eq. 7) is independent of the value of R, although it appears in both the integrand and the limits of integration. Physically, this result means that the combined effects of gas-layer thickness and circumference are the same in moving from the contact point to the outer limit for the two cases. Thus, both models show basically the same effect of increasing gas conductivity on the effective conductivity.

Region III – Gas Conduction

$$dq_{III} = k_g \int_1^{\sqrt{2}} \left(\frac{\pi}{2} - 2\tan^{-1}\sqrt{x^2-1} \right) x\,dx$$

This term is small, except when the gas conductivity is extremely high. Rather than evaluate the integral, an approximation is used which compensates exactly for the error incurred in region II at the limiting condition where $k_g/k_s = 1$, and partially compensates for it at intermediate values of k_g/k_s. This approximation is

$$q_{III} = \left(1 - \frac{\pi}{4} - \delta\right) k_g$$

which is equivalent to subtracting the contact area δ from the gas area $1 - \pi/4$ of the case where $\delta = 0$.

Total Effective Conductivity

Adding the heat fluxes through the three regions, and nondimensionalizing, yields the expression for the effective conductivity of a cubic array of truncated spheres

$$\frac{k_e}{k_s} = \delta + \frac{\pi}{2} \frac{\beta}{(1-\beta)^2} \left[\ln \frac{1}{\beta} - (1-\beta) \right] + \left(1 - \frac{\pi}{4} - \delta\right)\beta \qquad (9)$$

7.1.2 Estimation of Error in Calculation of Series-Conduction Term

The series-conduction term given in Eq. 9 is too large by the amount

$$2\beta \int_1^R \frac{(\tan^{-1}\sqrt{x^2-1})\,x\,dx}{1-(1-\beta)\sqrt{R^2-x^2}}$$

Making the substitution $u = \sqrt{R^2-x^2}$ and the small-angle approximation $\tan^{-1}\sqrt{x^2-1} \approx \sqrt{x^2-1}$ yields the form

$$2\beta \int_0^r \frac{\sqrt{r^2-u^2}\;u\,du}{1-(1-\beta)u}$$

The maximum value of r for the porous specimens considered is approximately 0.4. Therefore, the range of values of the denominator of the integrand is 0.6 to 1.0 for $\beta = 0$, and less for $\beta > 0$. The magnitude of the error term, which is always small, can be estimated with sufficient accuracy by setting the variable u in the dominator equal to its average value r/2, allowing the integral to be evaluated:

$$\frac{2\beta}{1-(1-\beta)\frac{r}{2}} \int_0^r \sqrt{r^2-u^2}\;u\,du = \frac{\frac{2}{3}\beta r^3}{1-(1-\beta)\frac{r}{2}}$$

Evaluation for $r = 0.4$, $\beta = 0.01$

$$\text{Correction term } \frac{\left(\frac{2}{3}\right)(0.01)\,(0.4)^3}{1-\frac{(0.99)(0.4)}{2}} = 0.000532$$

Uncorrected value 0.05785

$$\text{Relative error } \frac{0.000532}{0.05785} < 1\%$$

Evaluation for r = 0.4, $\beta = 0.1$

$$\text{Correction term } \frac{\left(\frac{2}{3}\right)(0.1)(0.4)^3}{1 - \frac{(0.9)(0.4)}{2}} = 0.00521$$

Uncorrected value 0.2722

$$\text{Relative error } \frac{0.00521}{0.2722} < 2\%$$

At higher values of β, the correction term increases further, but is partly compensated for by the term for region III; the total error decreases to zero at $\beta = 1$.

7.2 APPENDIX II – FABRICATION DRAWINGS

The experimental apparatus which provides the conditions for measuring the thermal conductivity of porous test specimens in a vacuum, and in an atmosphere of hydrogen at temperatures up to 5000°F consists of two major pieces of equipment.

1. High-frequency generator – 20-kw, 450-kc output, 220-v, 60-cycle, 3-phase input.
2. Bell jar fixture for controlled atmosphere heating modified to meet the requirements of the program.

The following drawings and specifications are required to fabricate and assemble the apparatus and are included in this appendix.

Dwg. No.	Title	Dwg. No.	Title
14276	Bell Jar Assembly	14286	Bottom Seal Collar
14277	Barrel	14287	Mirror Bracket
14278	Cap	14297	Hydrogen Thermal Conductivity Apparatus Schematic
14279	Base Plate		
14280	Nipple	14391	Pyrometer Mount
14281	Viewing Port Flange	14392	Bell Jar Fixture Specification
14282	Cover Plate	14393	Porous Tungsten Specimen Specification
14283	Gasket		
14284	Lifting Lug	14394	Solid Tungsten Specimen Specification
14285	Top Seal Collar		

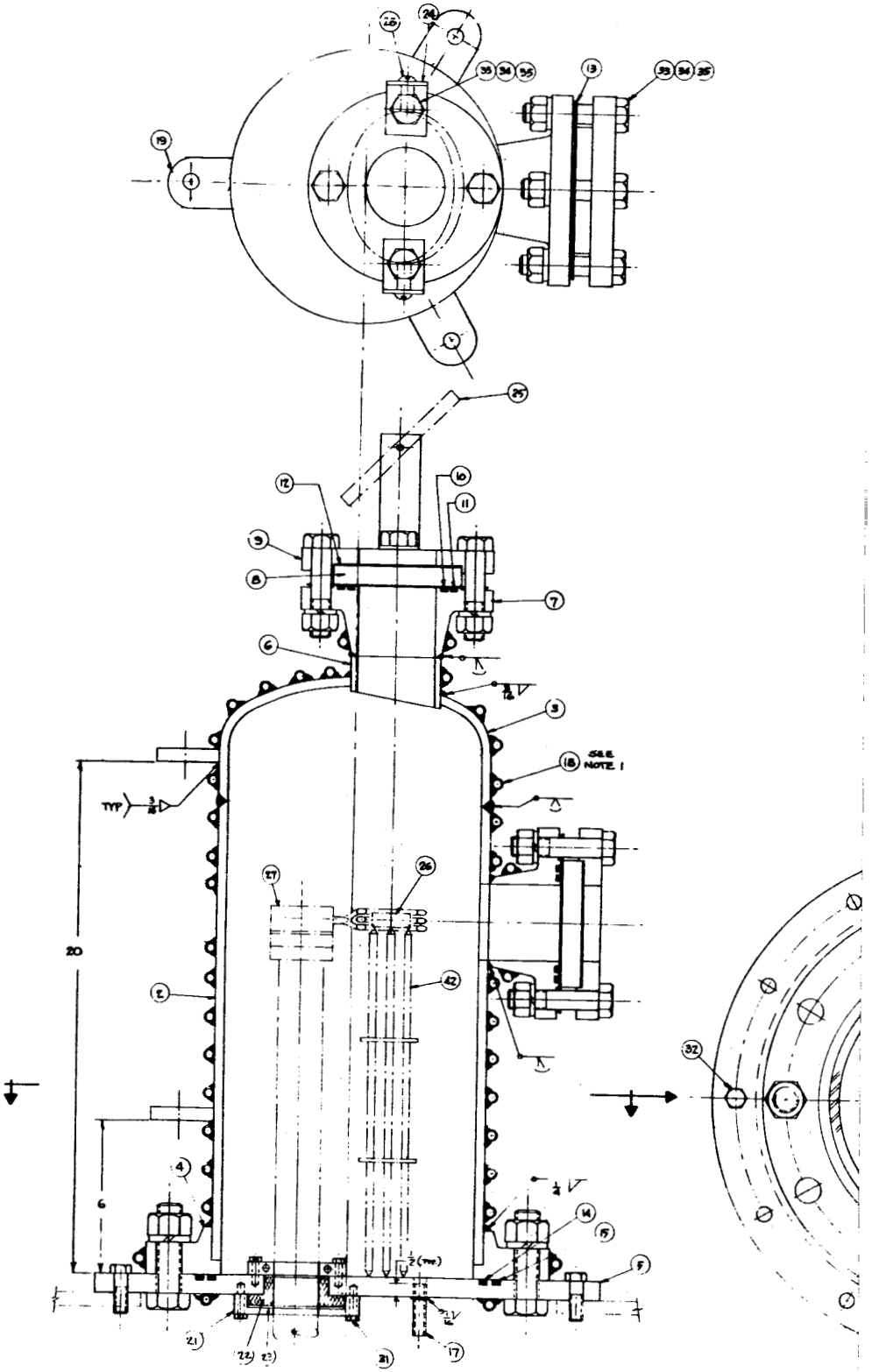

1) BELL JAR ASSEMBLY

PARTS LIST FOR DWG. NO. 14276

ITEM NO.	SHOWN ON DWG. NO.	QTY.	DESCRIPTION	MATERIAL	USED ON DWG. NO.
1	14276	1	BELL JAR ASSEMBLY		14276
2	14277	1	BARREL		
3	14278	1	CAP		
4	14276	1	10" 150# SOCKET WELD FLANGE	304 S.S.	
5	14279	1	BASE PLATE		
6	14280	1	NIPPLE		
7	14281	2	VIEWING PORT FLANGE		
8	14276	2	WINDOW 5" DIA x 1" THICK	QUARTZ	
9	14282	2	COVER PLATE		
10	14276	2	O RING PARKER NO 2427-44	NEOPRENE	
11	14276	2	O RING PARKER NO 2427-50	NEOPRENE	
12	14276	2	GASKET 5" O.D. x 4" I.D. x 1/16 THK.	NEOPRENE	
13	14283	2	GASKET		
14	14276	1	O RING PARKER NO 2427-77	NEOPRENE	
15	14276	1	O RING PARKER NO 2427-79	NEOPRENE	
16	14276	1	1 1/4" SCHED 40 PIPE 2" LG.	304 S.S.	
17	14276	2	1/4" SCHED 40 PIPE 2" LG.	304 S.S.	
18	14276	AS REQ'D	COOLING COIL 1/4" O.D. x .049 WALL	COPPER	
19	14284	6	LIFTING LUG		
20	14285	1	TOP SEAL COLLAR		
21	14286	1	BOTTOM SEAL COLLAR		
22	14276	1	SEAL (LEPEL H.F. LABS.)	RUBBER	
23	14276	1	SPLIT WASHER 3/8 O.D. x 11/32 I.D. x 1/16 THK.	304 S.S.	
24	14287	2	MIRROR BRACKET		
25	14288	1	MIRROR		
26	14276	1	SPECIMEN 1/4" DIA. x 1/4" THK.	TUNGSTEN	
27	14276	1	HEATING COIL ASSY (LEPEL)		
28	14276	2	NP 12-24 NC RD HD MACH SC 3/4 LG.	304 S.S.	
29	14276	4	1/4-20 NC HEX HD CAP SCR. 3/4 LG.	304 S.S.	
30	14276	2	1/4-20 NC HEX HD CAP SCR. 2 1/2 LG.	304 S.S.	
31	14276	4	1/4-20 NC HEX HD CAP SCR. 1" LG.	304 S.S.	
32	14276	12	3/8-16 NC HEX HD CAP SCR. 1 1/2 LG.	304 S.S.	
33	14276	8	3/8-16 NC HEX HD BOLT 4 LG.	304 S.S.	
34	14276	8	3/8-16 NC HEX NUT	304 S.S.	
35	14276	8	3/8 LOCKWASHER	302 S.S.	
36	14276	10	3/8-16 NC HEX HEAD BOLT 3" LG. (PARTIAL THREAD)	304 S.S.	
37	14276	10	3/8-16 NC HEX NUT	304 S.S.	
38	14276	10	3/8 LOCKWASHER	302 S.S.	
39	14276	2	1"-8 NC HEX BOLT 3" LG. (PARTIAL THREAD)	304 S.S.	
40	14276	2	1"-8 NC HEX NUT	304 S.S.	
41	14276	2	1" LOCKWASHER	302 S.S.	
42	14290	1	TRIPOD ASSEMBLY		

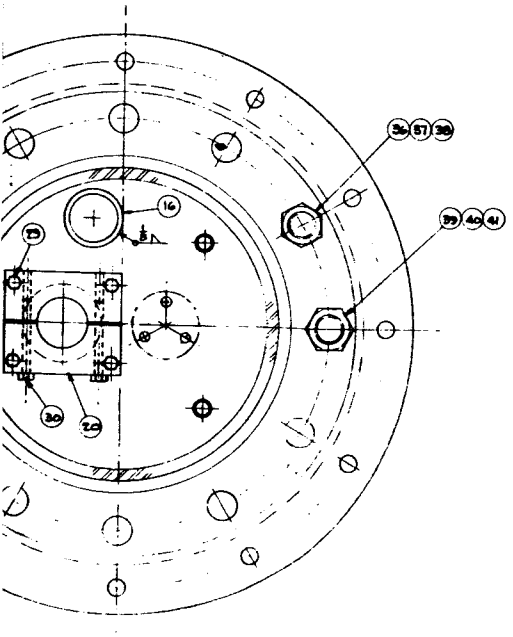

NOTES:

1. COOLING COIL (18) TO BE SILVER SOLDERED TO BELL JAR WITH A CONTINUOUS FILLET OF 1/16 x 3/8 (MIN.) AND A MAXIMUM PITCH OF 1".

1	8/64	RELOCATED LIFTING LUGS	7/1

UNITED NUCLEAR CORPORATION

DEVELOPMENT DIVISION

BELL JAR ASSEMBLY

			SCALE: HALF SIZE
			CLASS: U; SIZE: E
			DWG. NO. 14276
APPROVALS	DATE	PROJ. APPLIC.	

68

PARTS LIST FOR DWG. NO. 14277					
ITEM NO.	SHOWN ON DWG. NO.	QTY.	DESCRIPTION	MATERIAL	USED ON DWG. NO.
1	14277		10" SCHED 40 PIPE	304 S.S.	14276

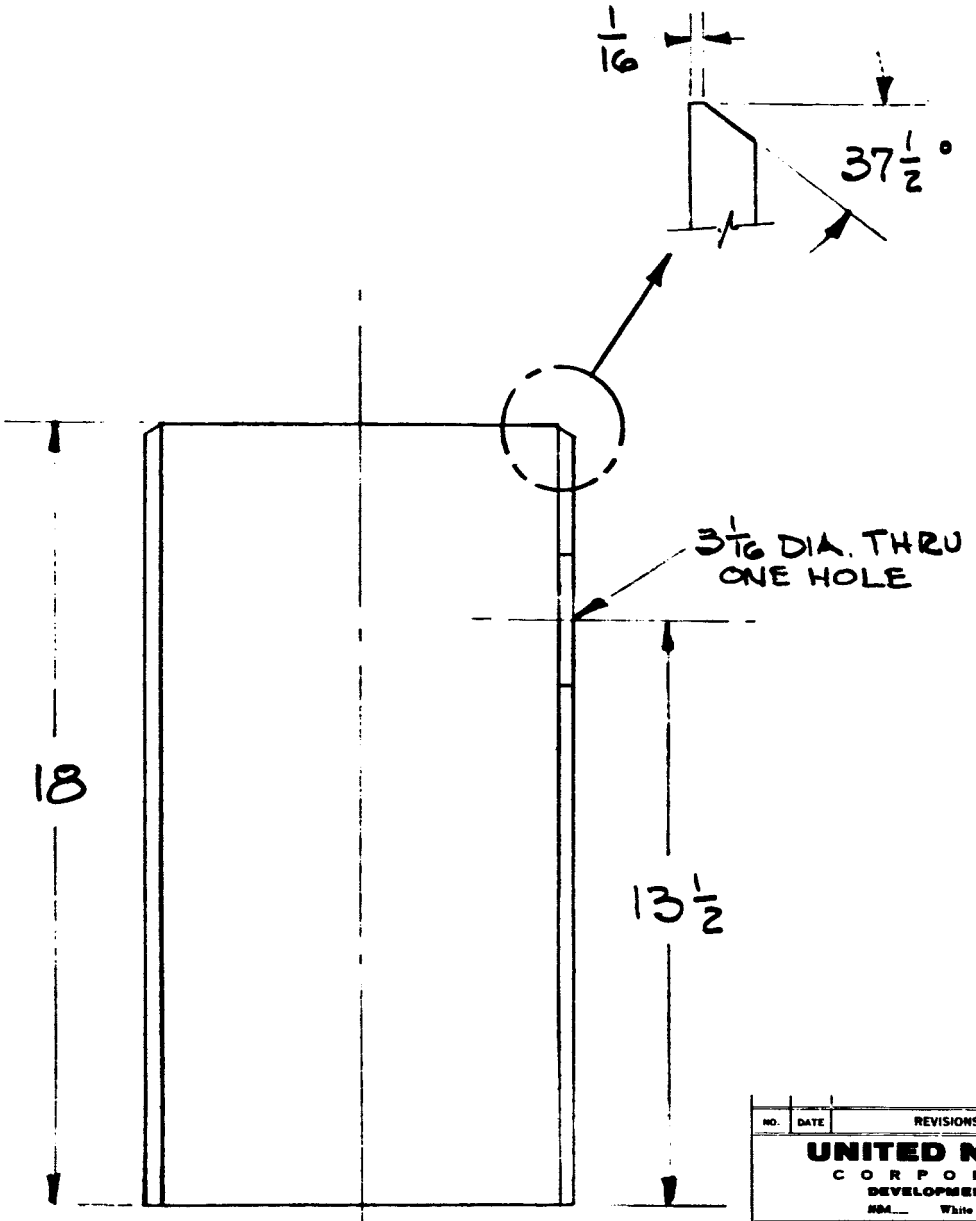

(1) BARREL

NO.	DATE	REVISIONS	DWN.	CHK.	APPD.

UNITED NUCLEAR
CORPORATION
DEVELOPMENT DIVISION
NDM — White Plains, New York

BARREL

			SCALE 1/4
PROJ. ENG. TDM	7/2/63		
DES. CHK.			CLASS U / SIZE B
DES. ENG. TDM	7/2/63		
DFT. CHK.			DWG. NO. 14277
DWN. BY JRR	6-5-63	2194-100	
APPROVALS	DATE	PROJ. APPLIC.	

PARTS LIST FOR DWG. NO. 14278					
ITEM NO.	SHOWN ON DWG. NO.	QTY	DESCRIPTION	MATERIAL	USED ON DWG. NO.
1	14278		10" SCHED 40 PIPE CAP	304 S.S.	14276

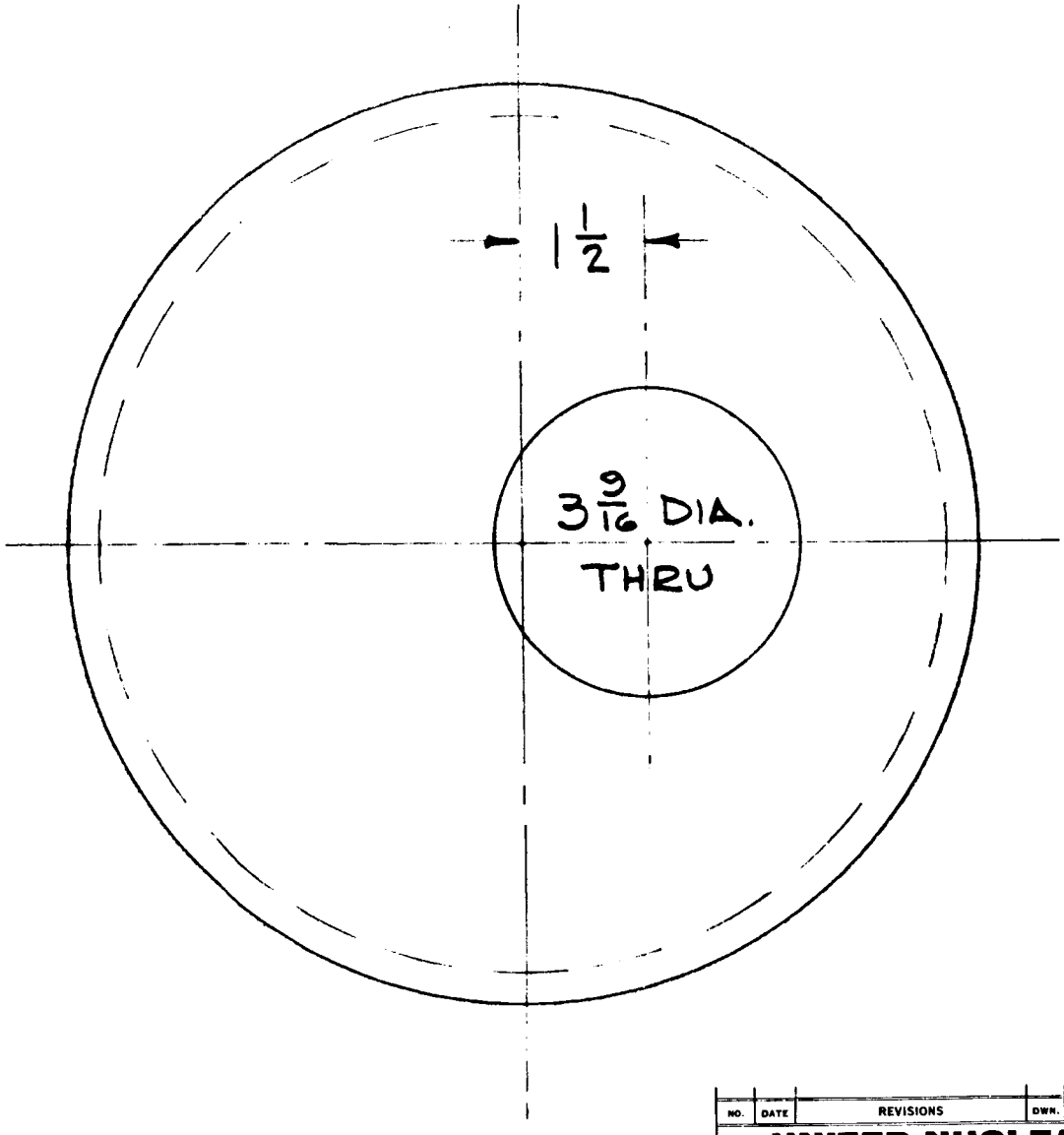

(1) CAP

NO.	DATE	REVISIONS	DWN.	CHK.	APPD.

UNITED NUCLEAR
CORPORATION
DEVELOPMENT DIVISION
NDA White Plains, New York

CAP

			SCALE HALF SIZE
Prel. Eng. TDH	7/1/63		
DES. CHK.			CLASS U / SIZE B
DES. ENG. TDH	7/1/63		
DFT. CHK.			DWG. NO. 14278
DWN. BY RRS	6-5-63	2194-100	
APPROVALS	DATE	PROJ. APPLIC.	

PARTS LIST FOR DWG. N° 14279					
ITEM NO.	SHOWN ON DWG. No.	QTY.	DESCRIPTION	MATERIAL	USED ON DWG. NO.
1	14279		BASE PLATE ½ x 20 DIA.	304 S.S.	14276

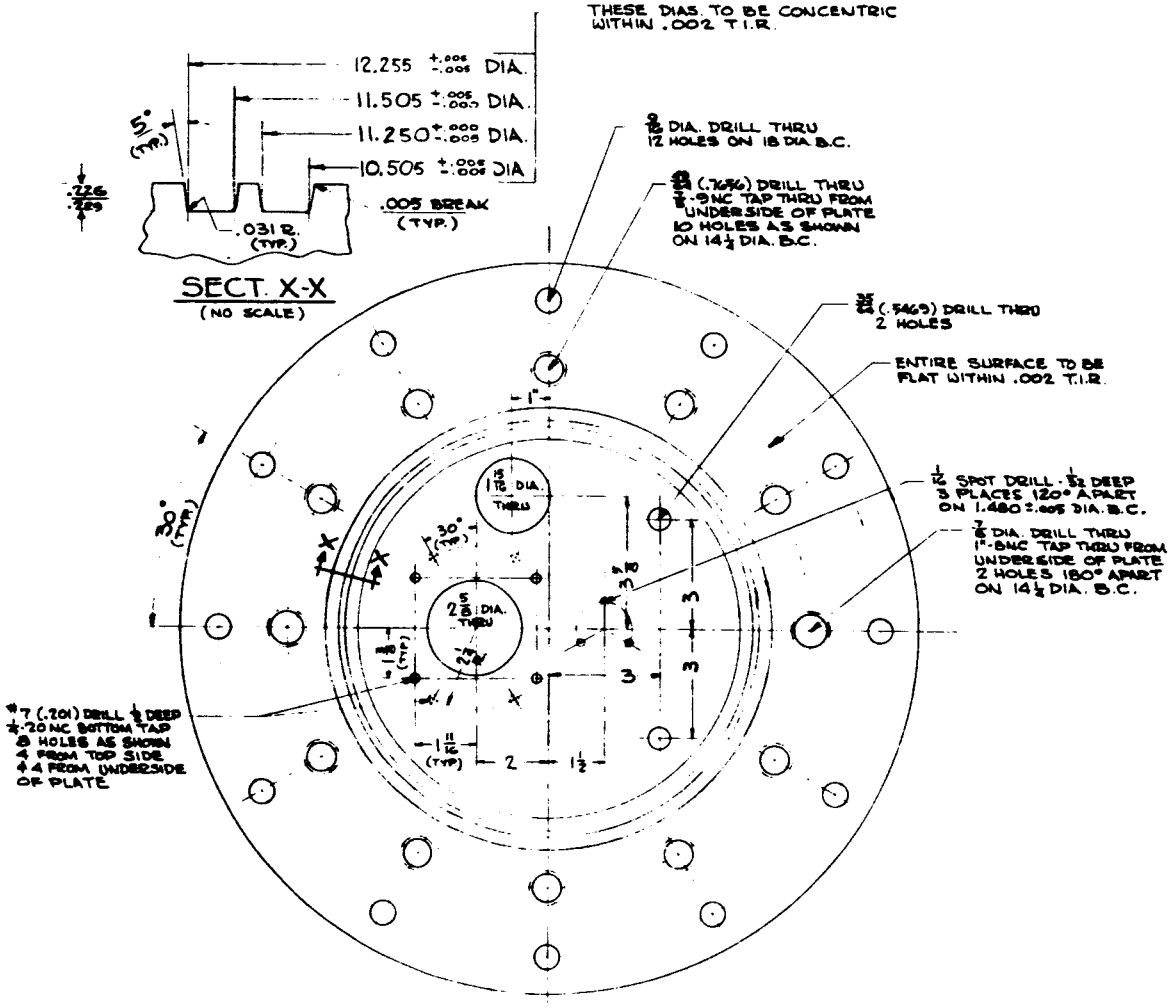

① BASE PLATE

1	7/28/61	O-RING DIM. CHANGED	SLI		
NO.	DATE	REVISIONS	DRN.	CHK.	APPD.

UNITED NUCLEAR
CORPORATION
DEVELOPMENT DIVISION
NEW HAVEN, New York

BASE PLATE

			SCALE:	HALF SIZE
PROT. ENGR.			CLASS	SIZE
ENGR. CHK.			U	C
ENGR. APPR.				
OPT. CHK.				
DWN. BY		2.194-100	DWG. NO.	
APPROVALS	DATE	PROJ. APPLIC.	14279	

PARTS LIST FOR DWG. NO. 14280					
ITEM NO.	SHOWN ON DWG. NO.	QTY	DESCRIPTION	MATERIAL	USED ON DWG. NO.
1	14280		3" SCHED 40 PIPE	304 S.S.	14276

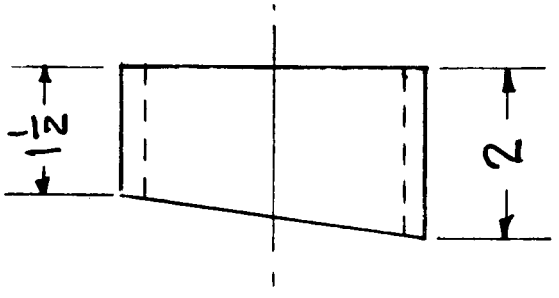

(1) NIPPLE

NO.	DATE	REVISIONS	DWN.	CHK.	APPD.

UNITED NUCLEAR
CORPORATION
DEVELOPMENT DIVISION
NDA — White Plains, New York

NIPPLE

			SCALE: HALF
Proj Engr.	7/2/63		
DES. CHK.			CLASS: U / SIZE: A
DES. ENG.	7/2/63		
DFT. CHK.			DWG. NO.
DWN. BY WRS	6-6-63	2124-100	14280
APPROVALS	DATE	PROJ. APPLIC.	

PARTS LIST FOR DWG. NO. 14281					
ITEM NO.	SHOWN ON DWG. NO.	QTY.	DESCRIPTION	MATERIAL	USED ON DWG NO.
1	14281		3" 150# ASA B16.5 W.N. FLG	304 S.S.	14276

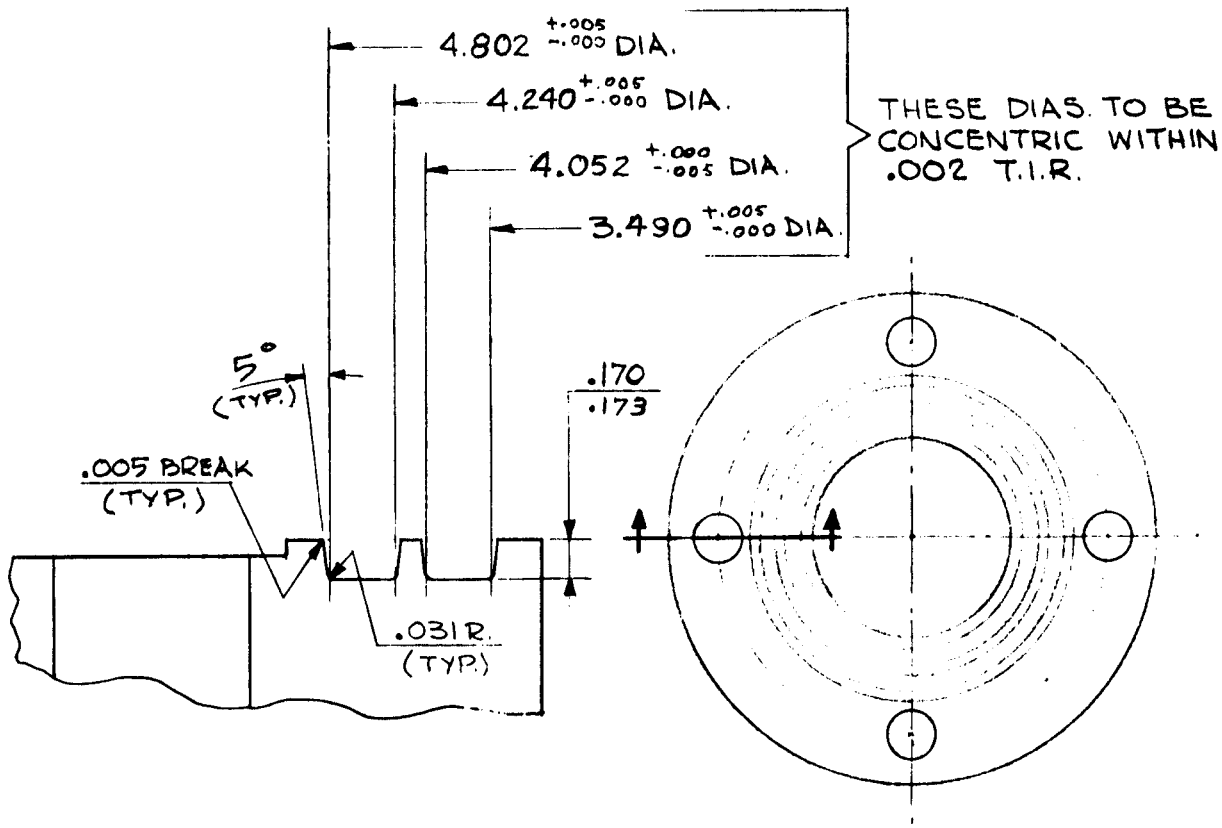

(1) VIEWING PORT FLG.

NO.	DATE	REVISIONS	DWN.	CHK.	APPD.
2	9/6/67	O-RING DIM. CHANGED	SLT	TDH	TDH
1	7/6/65	O-RING DIAM. CHANGED	TDH		TDH

UNITED NUCLEAR CORPORATION
DEVELOPMENT DIVISION
Mod. White Plains, New York

VIEWING PORT FLANGE

DES. CHK.	TDH	7/5/65	
DES. ENG.	TDH	7/5/65	
DFT. CHK.			
DWN BY	SLT	7/1/65	2124-100
APPROVALS		DATE	PROJ. APPLIC.

SCALE NONE
CLASS U
SIZE B
DWG. NO. 14281

PARTS LIST FOR DWG. NO. 14282					
ITEM NO.	SHOWN ON DWG. NO.	QTY	DESCRIPTION	MATERIAL	USED ON DWG. NO.
1	14282		3" 150# ASA B 16.5 BLIND FLG	304 S.S.	14276

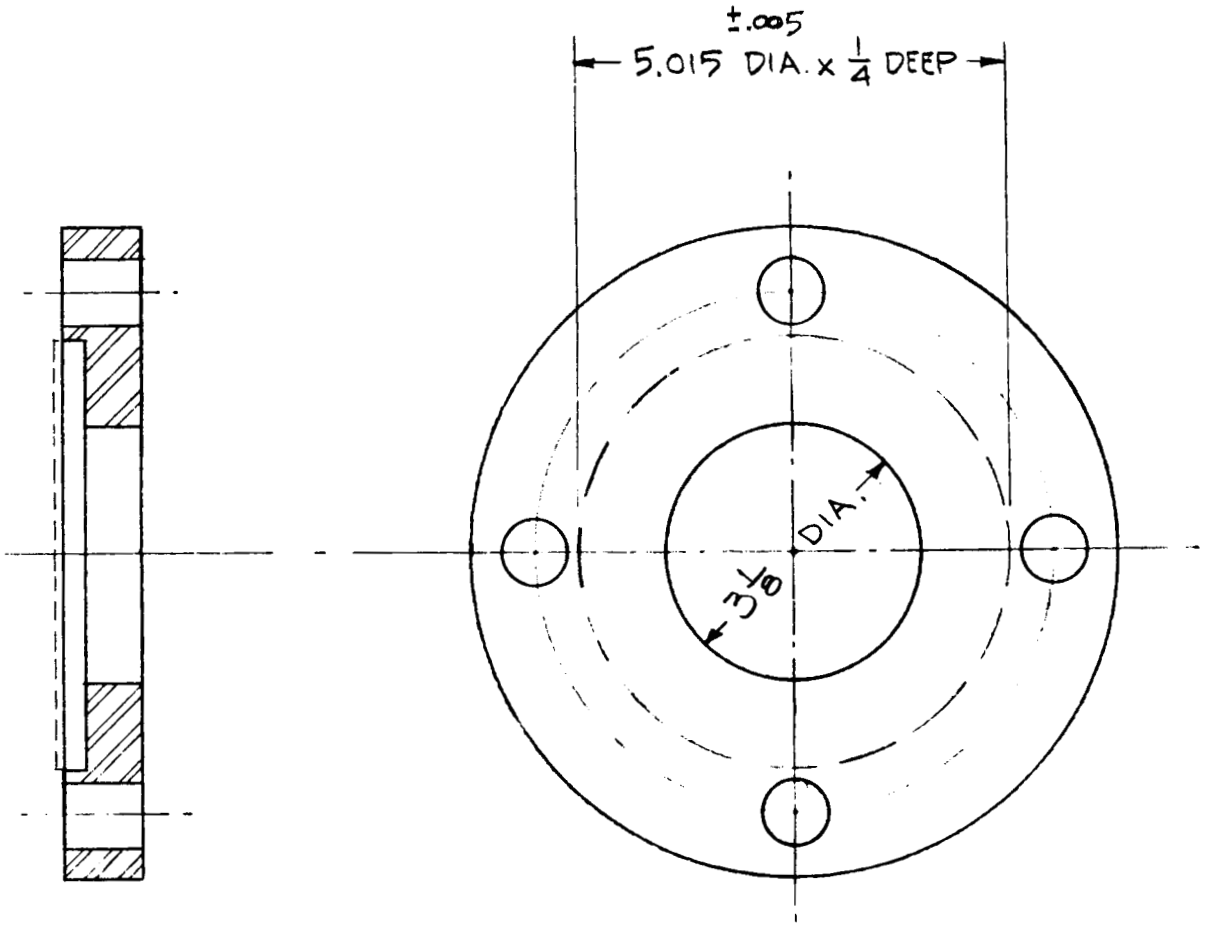

(1) COVER PLATE

NO.	DATE	REVISIONS	DWN.	CHK.	APPD.

UNITED NUCLEAR
CORPORATION
DEVELOPMENT DIVISION
NDA___ White Plains, New York

COVER PLATE

			SCALE HALF
PROJ. ENGR.	5/2/63		
DES. CHK.			CLASS U / SIZE B
DES. ENG.	5/2/63		
DFT. CHK.			DWG. NO. 14282
DWN. BY	5-31-63	2194-100	
APPROVALS	DATE	PROJ. APPLIC.	

PARTS LIST FOR DWG. NO. 14283					
ITEM NO.	SHOWN ON DWG. NO.	QTY	DESCRIPTION	MATERIAL	USED ON DWG. NO.
1	14283	-	GASKET 0.010 THK.	NEOPRENE	14276

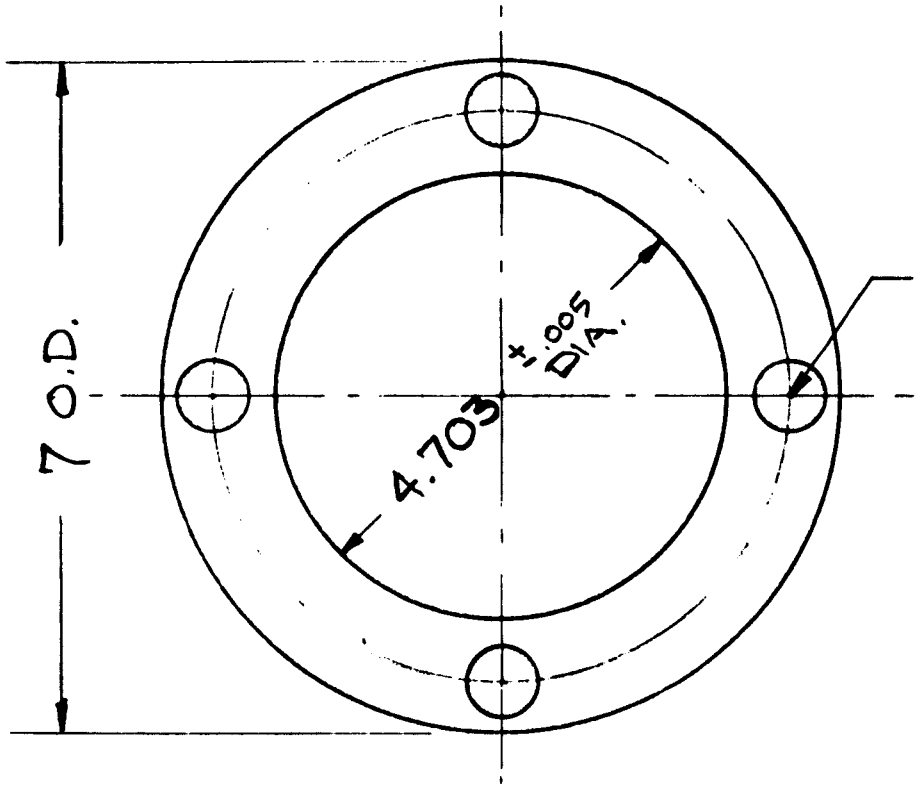

(1) GASKET

NO.	DATE	REVISIONS	DWN.	CHK.	APPD.

UNITED NUCLEAR
CORPORATION
DEVELOPMENT DIVISION
NDA — White Plains, New York

GASKET

			SCALE HALF
Proj. Engr.	7/2/63		
DES. CHK.			CLASS U / SIZE A
DES. ENG.	7/2/63		
DFT. CHK.			DWG. NO.
DWN. BY	5/31/63	2194-100	14283
APPROVALS	DATE	PROJ. APPLIC.	

PARTS LIST FOR DWG. NO. 14284					
ITEM NO.	SHOWN ON DWG. NO.	QTY	DESCRIPTION	MATERIAL	USED ON DWG. NO.
1	14284		LIFTING LUG 5/16x2 FB	304 S.S.	14276

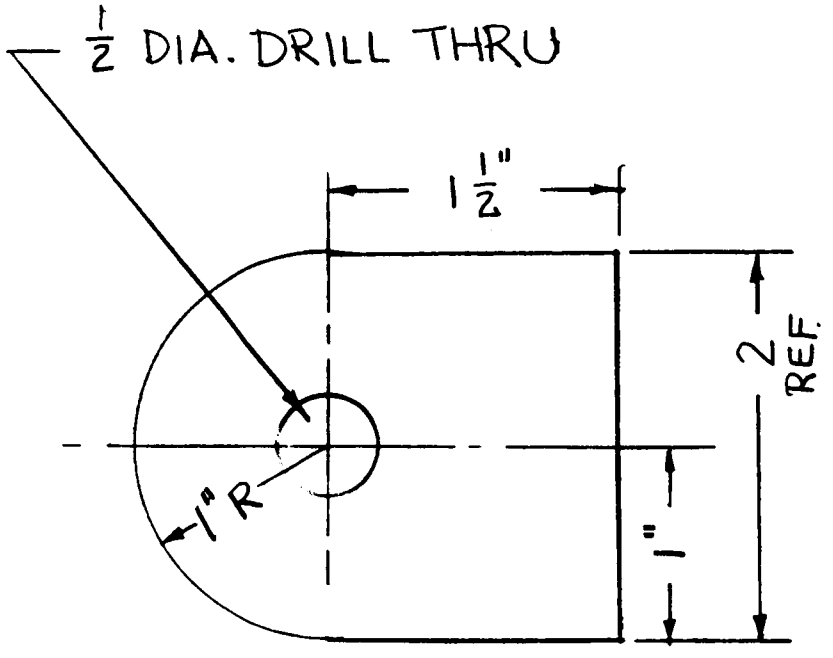

(1) LIFTING LUG

NO.	DATE	REVISIONS	DWN.	CHK.	APPD.

UNITED NUCLEAR
CORPORATION
DEVELOPMENT DIVISION
NDA — White Plains, New York

LIFTING LUG

			SCALE FULL
PROJ ENGR			
DES. CHK.			CLASS U / SIZE A
DES. ENG.			
DFT. CHK.			DWG. NO. 14284
DWN. BY T. ROE	5-31-63	2194-100	
APPROVALS	DATE	PROJ. APPLIC.	

PARTS LIST FOR DWG. NO. 14285

ITEM NO	SHOWN ON DWG NO	QTY	DESCRIPTION	MATERIAL	USED ON DWG. NO.
1	14285		TOP SEAL COLLAR ½" PLATE	304 SS	14276

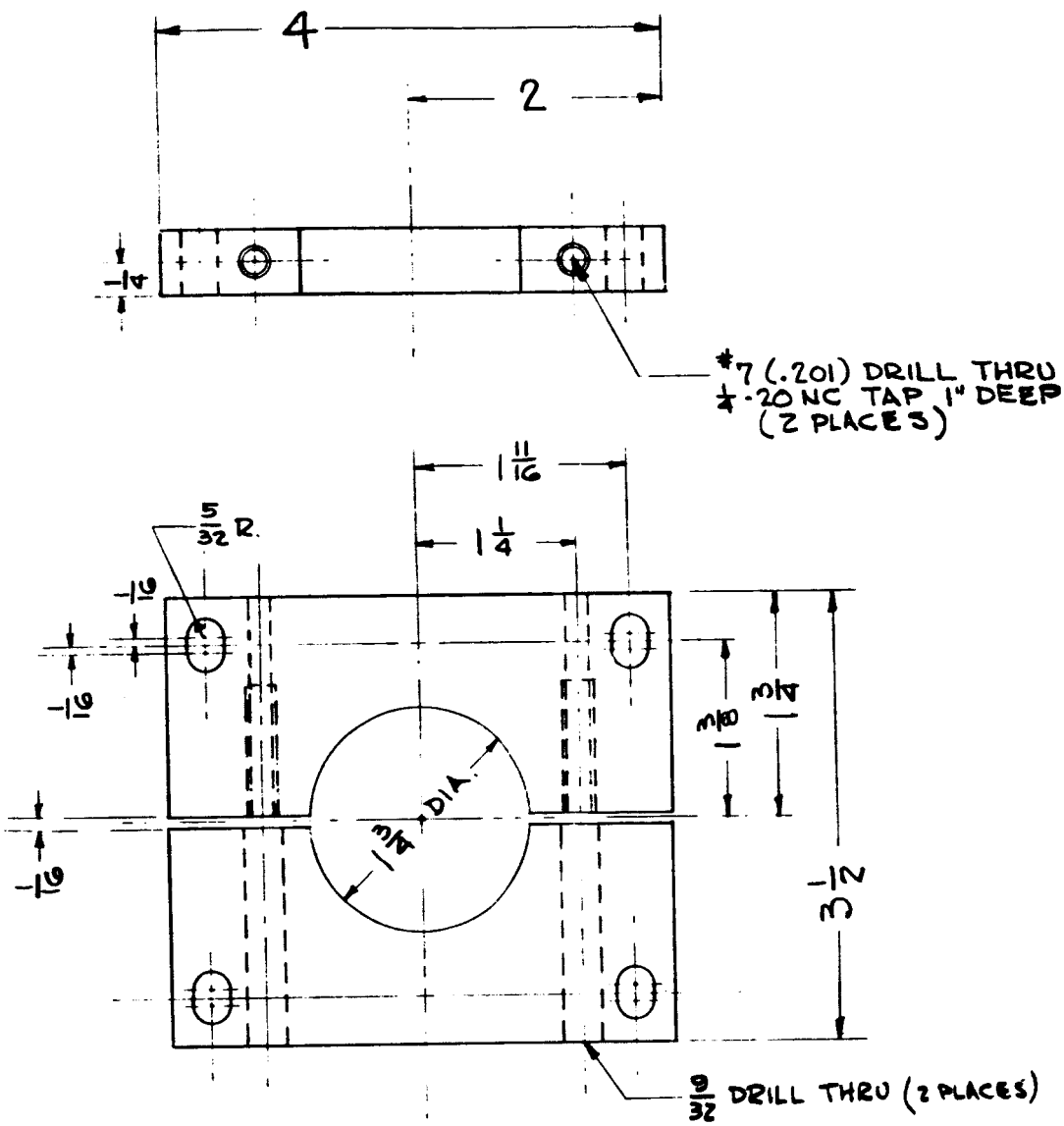

(1) TOP SEAL COLLAR

NO.	DATE	REVISIONS	DRWN.	CHK.	APPD.

UNITED NUCLEAR
CORPORATION
DEVELOPMENT DIVISION
White Plains, New York

TOP SEAL COLLAR

			SCALE FULL
Plant Engr.			CLASS U SIZE B
DES. CHK.			
DES. ENG.			DWG. NO.
DFT. CHK.			
DWN. BY	6-6-61	2194-100	14285
APPROVALS	DATE	PROJ. APPLIC.	

PARTS LIST FOR DWG. NO. 14286					
ITEM NO.	SHOWN ON DWG. NO	QTY	DESCRIPTION	MATERIAL	USED ON DWG. NO.
1	14286		BOTTOM SEAL COLLAR	Rod S.S.	14276

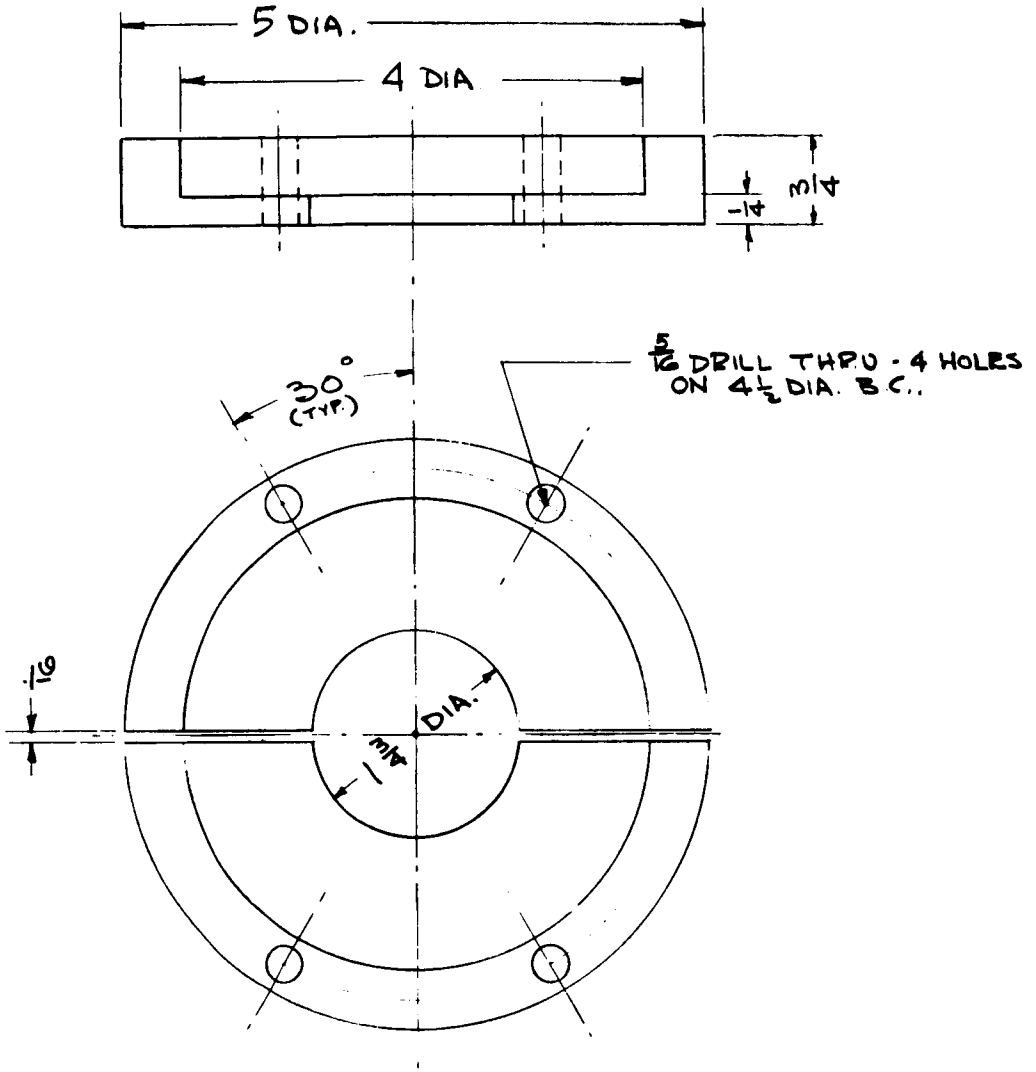

(1) BOTTOM SEAL COLLAR

NO.	DATE	REVISIONS	DWN.	CHK.	APPD.

UNITED NUCLEAR
CORPORATION
DEVELOPMENT DIVISION
NEW WHITE Plains, New York

BOTTOM SEAL COLLAR

			SCALE FULL
DES. CHK			CLASS U SIZE B
DES. ENG			DWG. NO.
DFT. CHK			
DWN. BY	6-6-61	2194-109	14286
APPROVALS	DATE	PROJ. APPLIC.	

PARTS LIST FOR DWG. NO. 14287					
ITEM NO.	DRAWN OR DWG. NO.	QTY	DESCRIPTION	MATERIAL	USED ON DWG. NO.
1	14287		MIRROR BKT. - 1/8 BAR	304 SS.	14276

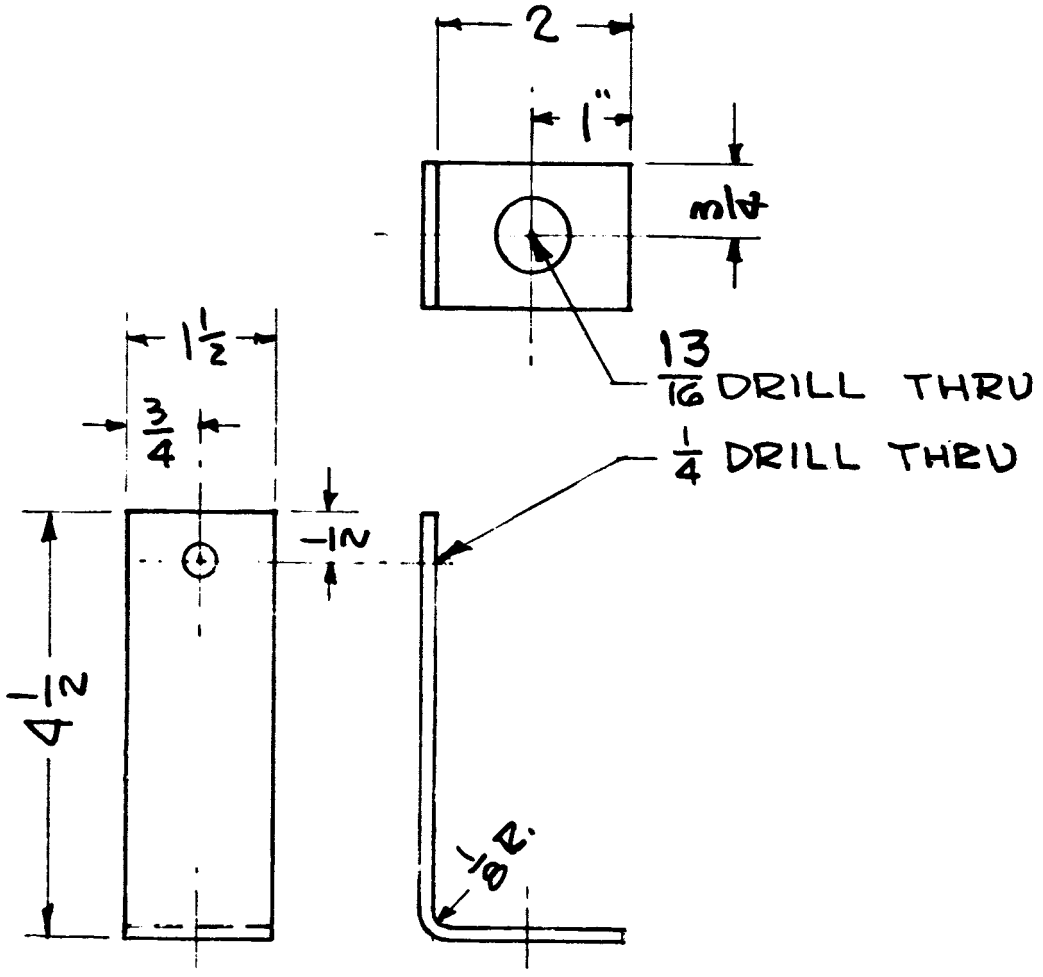

(1) MIRROR BRACKET

NO.	DATE	REVISIONS	DWN.	CHK.	APPD.

UNITED NUCLEAR
CORPORATION
DEVELOPMENT DIVISION
NDA — White Plains, New York

MIRROR BRACKET

			SCALE: HALF
PROJ. ENGR. [illegible]	7/2/63		CLASS: U / SIZE: A
DES. CHK.			
DES. ENG. [illegible]			
DFT. CHK.			DWG. NO.
DWN. BY [illegible]	6-6-63	2194-100	14287
APPROVALS	DATE	PROJ. APPLIC.	

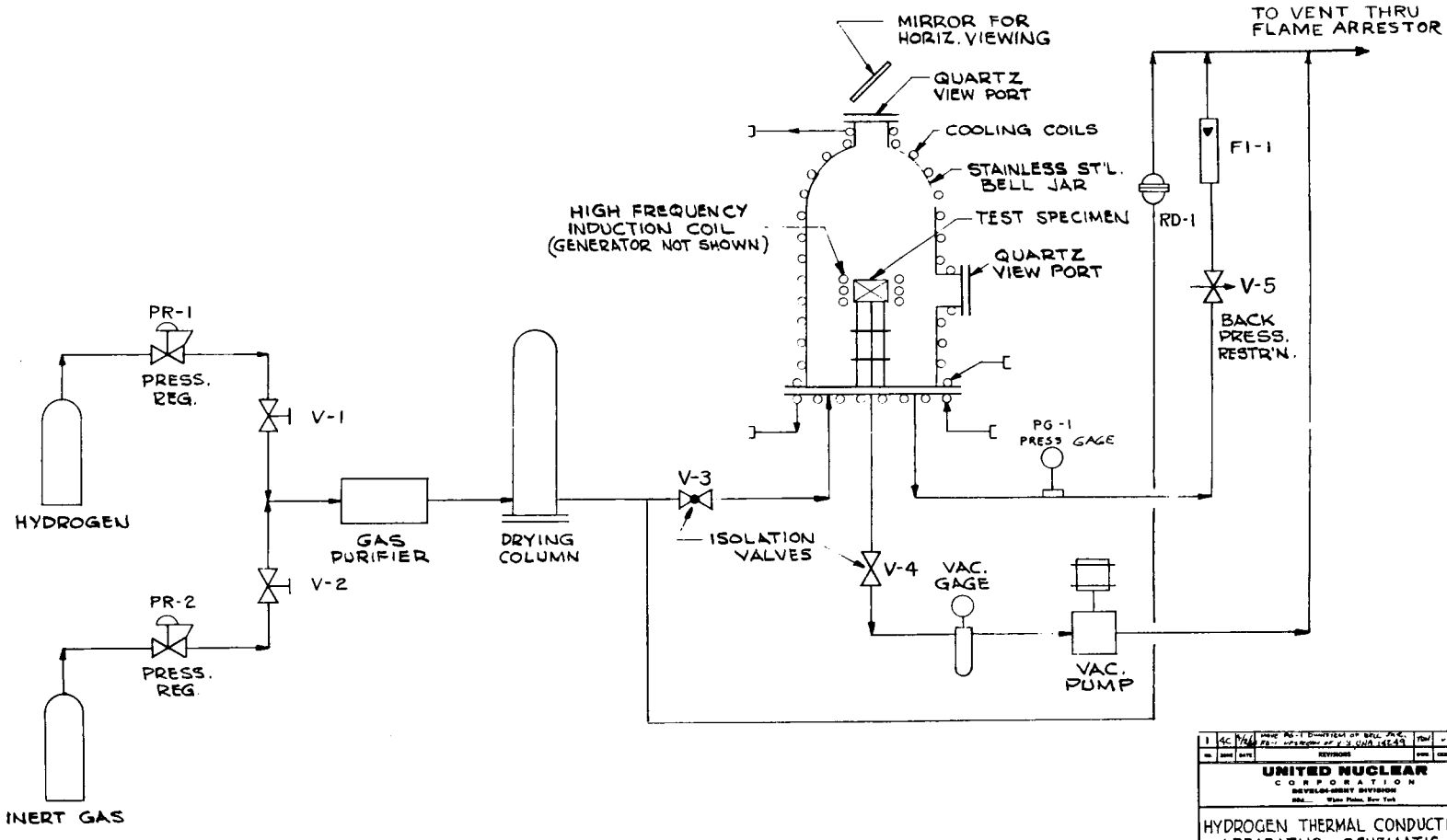

1	4C	7/64	ADDED PG-1 DOWNSTREAM OF BELL JAR. FI-1 UPSTREAM OF V-5 UNA 14549	TDW	-	7/64
NO.	BORE	DATE	REVISIONS	DWN	CHD	APPD

UNITED NUCLEAR CORPORATION
DEVELOPMENT DIVISION
NNA — White Plains, New York

HYDROGEN THERMAL CONDUCTIVITY APPARATUS SCHEMATIC

DES. CHR. TDW	7/64		SCALE: NONE
DES. ENG.	7/64		CLASS U / SIZE C
DFT. CHR.			
DWN. BY TDW	6-1-65	5124-100	DWG. NO. 14297
APPROVALS	DATE	PROJ. APPLIC	

PARTS LIST FOR DWG. NO. 14391					
ITEM NO.	SHOWN ON DWG. NO.	QTY.	DESCRIPTION	MATERIAL	USED ON DWG. NO.
1	——		PYROMETER MOUNT	——	——
2	——	34'	3"[X 4.1 #/FT	ST.	——
3	——	2	¼ X 1½ X 9" PLATE	ST.	——

NOTES:
1. ALL STANDARD STEEL MEMBERS (CHANNELS & PLATES) TO BE JOINED BY WELDING.

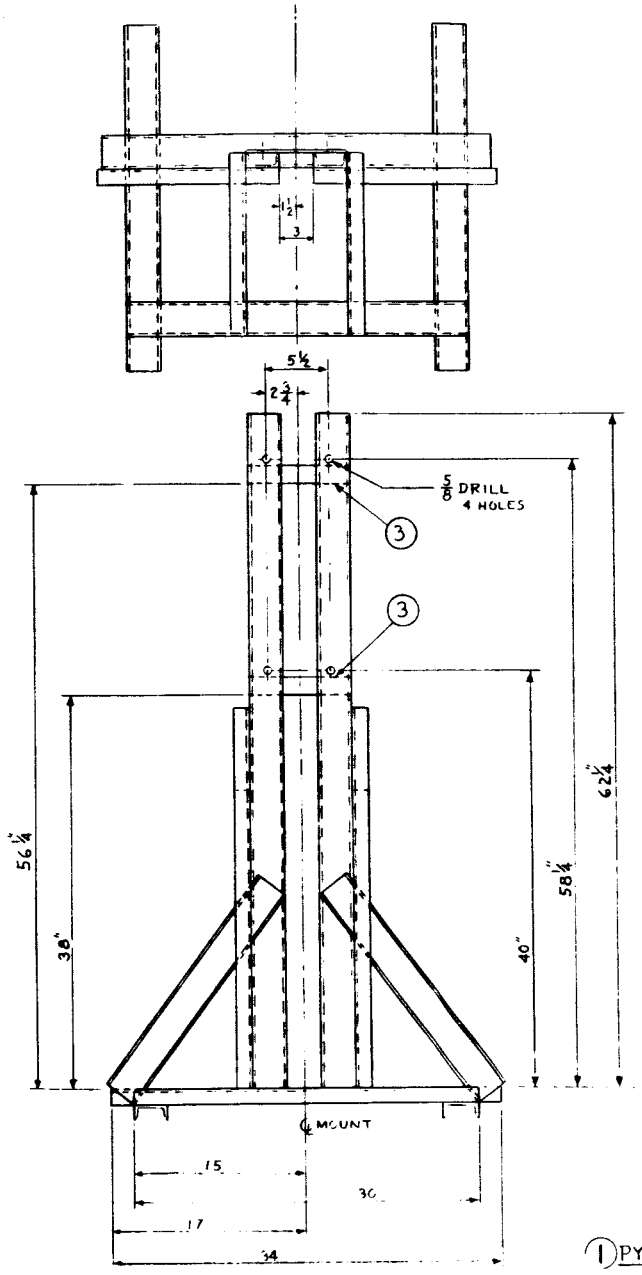

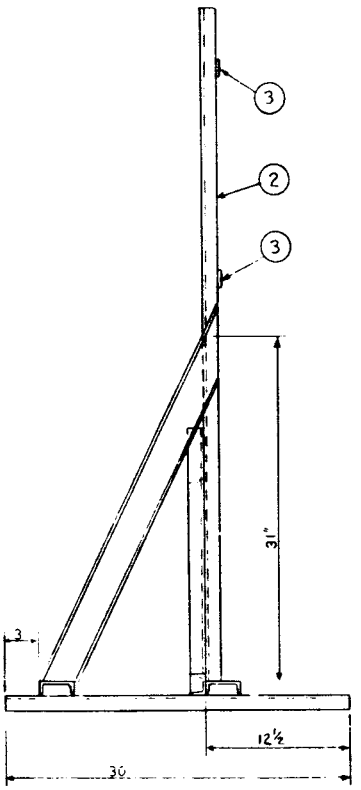

(1) PYROMETER MOUNT

UNITED NUCLEAR CORPORATION DEVELOPMENT DIVISION			
PYROMETER MOUNT			
			SCALE: 3/16 = 1"
			CLASS U / SIZE D
			DWG. NO. 14391
APPROVALS	DATE	PROJ. APPLIC.	

UNITED NUCLEAR
CORPORATION
DEVELOPMENT DIVISION

POROUS TUNGSTEN SPECIMEN SPECIFICATION

ORIGINAL ISSUE PREPARED BY	PROJECT APPLICATION	SPECIFICATION NO.
T. D. Hawkins	Hydrogen Thermal Conductivity Project 2194	14393
DATE 8/2/63		LATEST REV. 3 DATE 8/5/63
		REV. DESCRIPTIONS START ON PAGE NO. 1

ORGANIZATION	CHECKED BY	DATE	APPROVED BY	DATE
R&D Engr			T D Hawkins	8/2/63

UNITED NUCLEAR
CORPORATION
DEVELOPMENT DIVISION

SPEC. NO. 14393

PAGE ____ OF ____

REV. NO.	DATE	PAGE NO.	DESCRIPTION	BY	CHKD.	APPD.
1	5/5/63		0.006 inch max. diam.	SJ.	SJ	TDK
2			remarked – The porous compact shall			
			have 100% interconnected pores.	SJ.	SJ	TDK
3			Add- The porosity of the specimen			
			shall be uniform and shall be			
			free of cracks	SJ	SJ	TDK

POROUS TUNGSTEN TEST SPECIMEN

This specification constitutes a revision of the preliminary specifications set forth in HTEO-48 and, therefore, supersedes that specification.

1. Specimen size, configuration, and number.

The test specimens shall be in the form of a right circular cylinder, with dimensions shown in the attached sketch. A total of two (2) specimens will be required. One (1) specimen shall be 1" nominal diam. by ½" long, and one (1) specimen shall be 1½" nominal diam. x ½" long.

2. Particle size.

All particles composing the porous compact shall be within the following size range:

Maximum particle size	0.010 inch max. diam.
Minimum particle size	0.006 inch max. diam.

3. Purity.

All tungsten used in fabricating the test specimens shall have a purity of 99.8% tungsten.

4. Porosity and pore interconnection.

The porosity of the final porous compact shall be at least 30%. **The porsity of the specimen shall be uniform and shall be free of cracks.**

5. Specimen identification and dimensions.

As-built values of the dimensions shown in the attached sketch shall be provided for each specimen. These dimensions shall be measured within $\pm$ 0.001 inch.

6. The specimen will be a free standing body with no mechanical loads other than its weight imposed on it. It is required, however, that the porous compact maintain its mechanical integrity (porosity and pore size) up to the sintering temperature of the tungsten.

BY TDH DATE 9/3/63 SUBJECT _____ SHEET NO. _____ OF _____

CHKD. BY _____ DATE _____ JOB NO. 2194-100

POROUS TUNGSTEN

TEST SPECIMEN

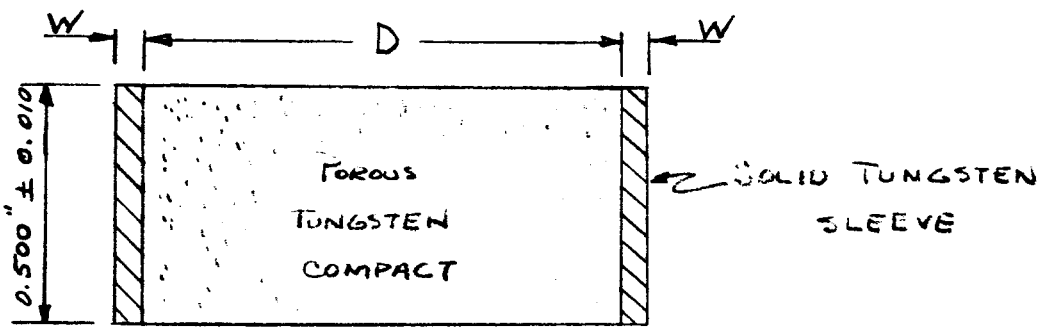

	D	W
SPECIMEN A	1.00" ± 0.01"	0.040" ± 0.005"
SPECIMEN B	1.50 ± 0.01"	0.040" ± 0.005"

UNITED NUCLEAR
CORPORATION
DEVELOPMENT DIVISION

BELL JAR FIXTURE SPECIFICATION

Reference Drawings

Lepel Laboratories Dwg. No. 7310, Rev. B
7310-1
6687-5

United Nuclear Corp. Dwg. No. 14276
14279

ORIGINAL ISSUE PREPARED BY T. D. Hawkins DATE 8/2/63	PROJECT APPLICATION Hydrogen Thermal Conductivity Project 2194		SPECIFICATION NO. 14392 LATEST REV. DATE REV. DESCRIPTIONS START ON PAGE NO.	
ORGANIZATION	CHECKED BY	DATE	APPROVED BY	DATE
Proj. Engr.			T D Hawkins	8/2/63

1. PURPOSE

This specification sets forth the procedures which are to be followed in the fabrication and assembly of the bell jar fixture which will provide a controlled atmosphere station for the heating of a porous tungsten test specimen with R.F. frequency induction heating equipment. The detailed requirements of the components of this fixture are set forth in drawings by Lepel Laboratories and United Nuclear Corporation which are referred to at appropriate places in this specification.

2. GENERAL DESCRIPTION

The fixture shall consist of a standard bell jar table similar in design to that shown in Lepel Laboratories Drawing No. 7310, Rev. B. The bell jar table shall be furnished complete and in accordance with the specification set forth in Drawing 7310, Rev. B, except as modified by this specification.

3. EQUIPMENT FURNISHED BY UNITED NUCLEAR CORP.

A stainless steel bell jar will be fabricated by United Nuclear Corp., Development Division. The bell jar shall be fabricated in accordance with UNC Drawing No. 14276. This design allows for the adaptation of the bell jar to the standard bell jar fixture designated in paragraph 2 above.

4. EQUIPMENT FURNISHED BY SUPPLIER

The supplier shall furnish the bell jar table as specified in Lepel Drawing No. 7310, Rev. B, with the exceptions listed below:

4.1 The bell jar assembly shown in Lepel Drawing No. 7310-1 is not required.

4.2 Two (2) guide plates as shown in Lepel Drawing No. 6687-5 shall be furnished, except that the 15-1/8" dia. hole shall not be cut out. The plates shall be complete in all other respects, and shall include roller guides and mountings, lifting lugs, and other assemblies and attachments which are normally supplied with the complete bell jar fixture. These plates will be modified by UNC for installation on the UNC stainless steel bell jar.

4.3 The table top shown in Lepel Drawing No. 7310, Rev. B, shall be machined to accept the base plate of the UNC stainless steel bell jar. The general arrangement is shown in UNC Drawing No. 14276, and the details required for machining are shown in UNC Drawing No. 14279.

4.4 The Flowrator Control Assembly as specified in Lepel Drawing No. 7310, Rev. B, shall be modified to provide for the measurement of the following gases and flow rates:

Hydrogen	10-75 SCFH
Helium	5-45 SCFH

Other requirements shall be as specified in the above designated drawing. The Flowrator Control Assembly shall be installed as shown on Lepel Drawing No. 7310, Rev. B, except that the "¼" OD copper tube, secure to detail 'O'" shall be omitted. UNC will install this line at final assembly.

4.5 The counter weights shown in Lepel Drawing 7310, Rev. B, shall be increased to accomodate the weight of the stainless steel bell jar which is approximately 180 lbs.

4.6 All parts for the R.F. co-axial lead through seal, shown in Lepel Drawing No. 7310, Rev. B, shall be fabricated by UNC. The supplier, however, shall mold the silastic-silicone rubber seal at assembly.

UNITED NUCLEAR
CORPORATION
DEVELOPMENT DIVISION

SOLID TUNGSTEN SPECIMEN SPECIFICATION

ORIGINAL ISSUE PREPARED BY	PROJECT APPLICATION	SPEC. NO.
T. D. Hawkins	Hydrogen Thermal Conductivity Project 2194	14394
DATE 8/2/63		LATEST REV. DATE
		REV. DESCRIPTIONS START ON PAGE NO.

ORGANIZATION	CHECKED BY	DATE	APPROVED BY	DATE
Trat. Engr			[signature]	8/5/63

SOLID TUNGSTEN TEST SPECIMEN

Requirement Specification

United Nuclear Project 2194

This specification sets forth the requirements for a solid tungsten test specimen to be used in the title project.

1. Size, Configuration, and Number

   One (1) test specimen will be required. The dimensions and tolerances are shown in the attached sketch. The specimen shall be in the form of a right circular cylinder.

2. Specimen Density

   A maximum density specimen is required. The density shall, however, be no less than 99%.

3. Purity

   The specimen material shall be at least 99.8% pure tungsten.

BY TDH DATE 7/9/63 SUBJECT _____ SHEET NO. _____ OF _____

CHKD. BY _____ DATE _____ JOB NO. 2196-200

SOLID TUNGSTEN TEST SPECIMEN

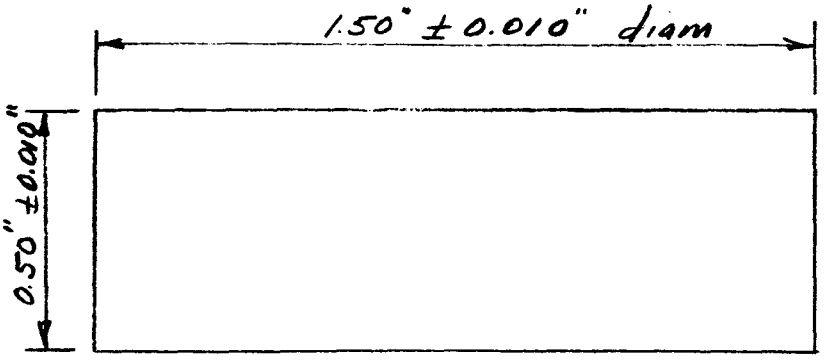

7.3 APPENDIX III – REDUCTION OF OBSERVED BRIGHTNESS TEMPERATURES TO TRUE TEMPERATURES

The technique of the optical pyrometer is to match the brightness of the calibrated filament to the apparent brightness of the subject at a given wave length (in reality, the match is made over a small band of wave lengths), hence, the name observed brightness temperature. The temperature recorded by the pyrometer is that of a black body having the same radiant energy flux within the wave length band of the instrument as the nonblack body under consideration. The radiant energy flux is obtained from Wien's formula for black body radiation

$$J_{BR} = C_1 \lambda^{-5} e^{-C_2/\lambda T_{BR}}$$

where J_{BR} is the radiant energy flux at wave length λ from a black body at temperature T_{BR}. T_{BR} is the temperature recorded by the pyrometer. The energy flux from a nonblack body is estimated from the same formula as follows:

$$J_{NB} = \epsilon_\lambda C_1 \lambda^{-5} e^{-C_2/\lambda T_T}$$

where J_{NB} is the radiant energy flux from a nonblack body at temperature T_T and having a spectral emissivity, ϵ_λ at wave length, $\lambda = 0.65\mu$. The true temperature T_T of the specimen is calculated from the observed brightness temperature T_{BR} by equating (matching) the radiant energy fluxes for the black body and nonblack body with the result

$$\frac{1}{T_T} = \frac{1}{T_{BR}} + \frac{\lambda}{C_2} \ln \epsilon_\lambda$$

Since there is a quartz window between the specimen and pyrometer, the radiant energy flux reaching the pyrometer is

$$J = \tau_\lambda \epsilon_\lambda C_1 \lambda^{-5} e^{-C_2/\lambda T_T}$$

where τ_λ is the spectral transmissivity of the window. In this case, the true temperature is related to the brightness temperature by

$$\frac{1}{T_T} = \frac{1}{T_{BR}} + \frac{\lambda}{C_2} \ln \tau_\lambda \epsilon_\lambda \tag{10}$$

C_2 is an empirical constant whose value is 25,891 (μ-°R).

The transmissivity of the quartz window was determined by making temperature measurements with and without the window in the line of sight. The transmissivity of the window is determined from the above radiant energy flux equations as follows:

$$\ln \tau_\lambda = \frac{C_2}{\lambda} \left[\frac{1}{T_{BR}(\text{measured without window})} - \frac{1}{T_{BR}(\text{measured with window})} \right]$$

The average transmissivity for the top viewing window is 0.909.

A comparison of true and observed brightness temperatures is shown in Fig. 25. The quartz window transmissivity is 0.909; the spectral emissivity for porous tungsten is 0.58; and the spectral emissivity for solid tungsten is shown in Fig. 26.

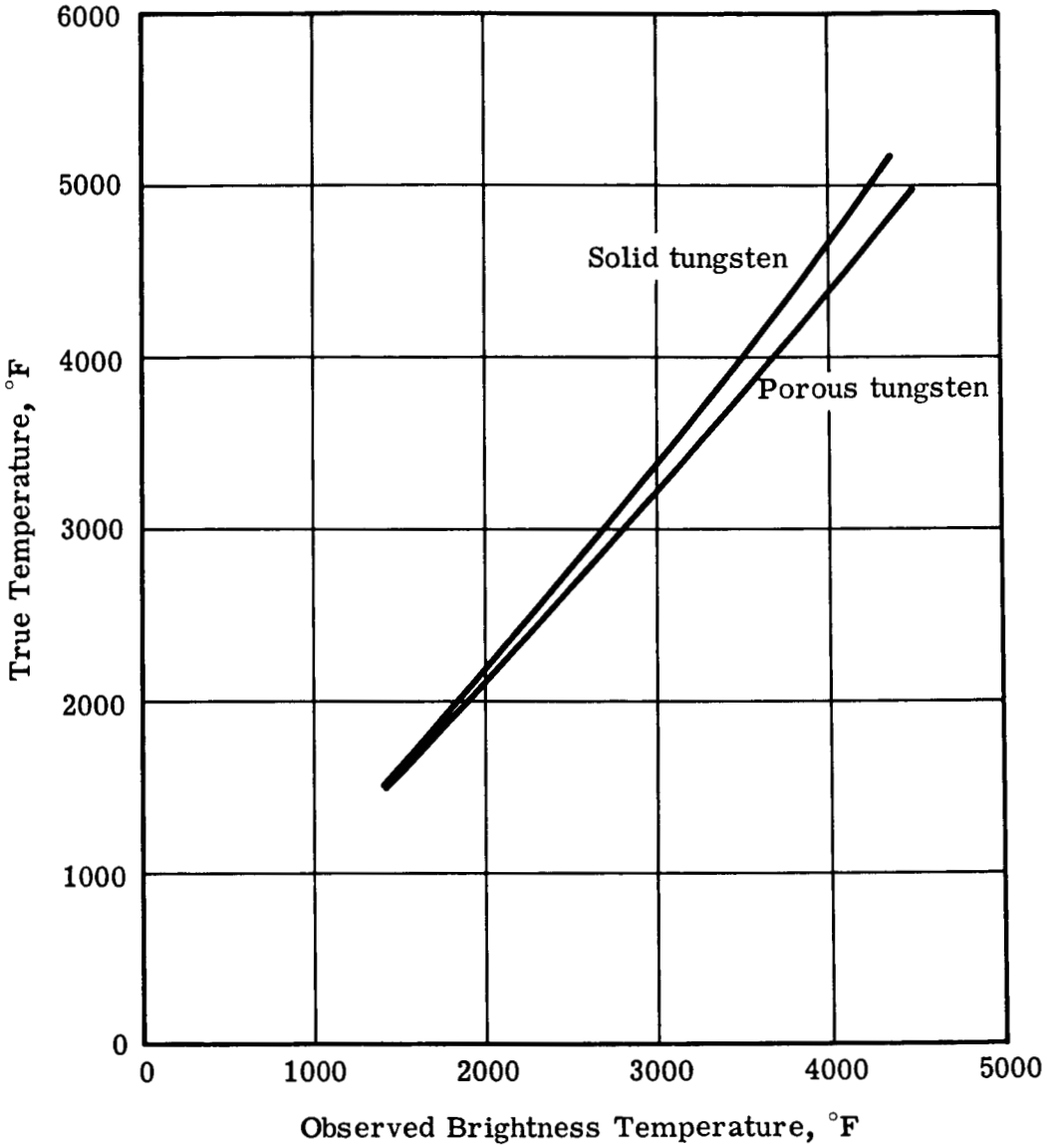

Fig. 25 — Comparison of true temperatures and observed brightness temperatures

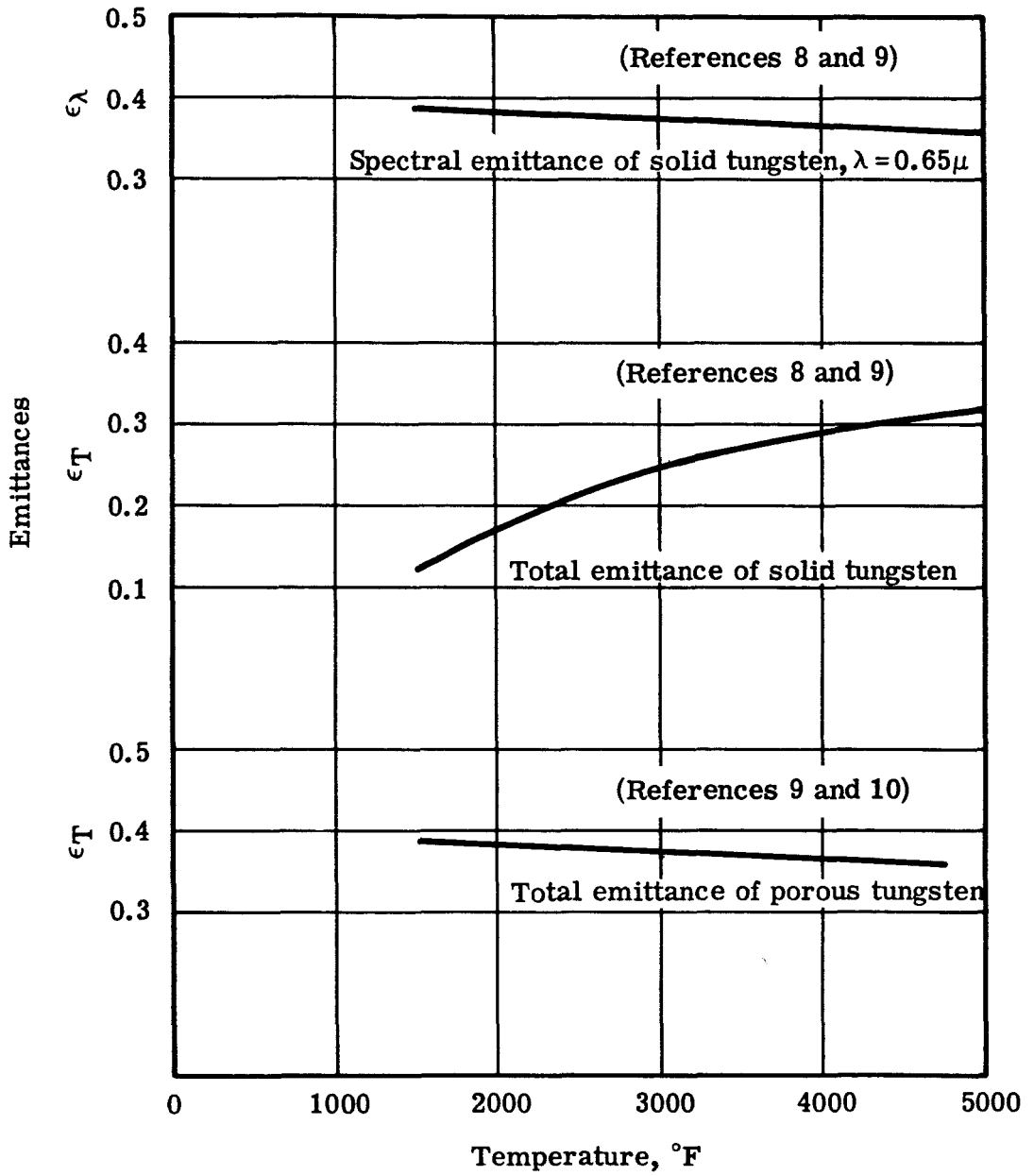

Fig. 26 — Emittances for porous and solid tungsten

7.4 APPENDIX IV – OBSERVED BRIGHTNESS TEMPERATURES OVER THE UPPER SURFACE OF THE SPECIMEN

The following tables contain uncorrected brightness temperature observations obtained for the solid and the porous tungsten specimens in vacuum, helium, and hydrogen. Two temperature observations were made at each radial location. No data are presented for the $1\frac{1}{2}$-in. porous Wah Chang specimen with solid ring as those data were subsequently discarded because of their obviously incorrect results. The pertinent features of the specimens are as follows:

Solid Tungsten – 1.52 in. diameter; 99.8% dense.

$1\frac{1}{2}$-in. Porous Wah Chang Specimen – 1.45 in. diameter; 42% porous; no solid ring surrounding the specimen.

1-in. Porous Wah Chang Specimen (sans solid ring) – 0.975 in. diameter; 42% porous; no solid ring surrounding the specimen.

$1\frac{1}{2}$-in. Porous Trial Specimen – 1.52 in. diameter; 55% porous; no solid ring surrounding the specimen.

Observed Brightness Temperatures Over Uppe

Run No.	0.76	0.6	0.45	0.30	0.15	0	0.15	0.30
				Radial Locations from Center Along X-				
21	2330	2322	2315	2310	2309	2302	2309	231
	2330	2322	2318	2311	2310	2310	2309	231
22	2730	2705	2695	2690	2680	2680	2682	269
	2728	2705	2695	2690	2682	2682	2690	269
23	3125	3090	3070	3055	3040	3045	3050	305
	3130	3100	3070	3050	3045	3050	3050	305
24	3520	3460	3420	3400	3390	3380	3390	340
	3520	3460	3420	3400	3390	3380	3385	340
25	2050	2043	2036	2036	2035	2040	2038	204
	2050	2040	2036	2036	2036	2038	2038	204
				Radial Locations from Center Along				
	0.70	0.60	0.45	0.30	0.15	0	0.15	0.30
119	2537	2525	2522	2518	2520	2515	2515	251
	2538	2525	2522	2520	2520	2515	2518	251
120	2900	2887	2870	2860	2856	2850	2855	285
	2900	2888	2870	2860	2858	2850	2855	286
121	3780	3740	3680	3650	3640	3640	3643	366
	3790	3740	3690	3655	3640	3640	3650	367
122	4020	3980	3900	3860	3850	3845	3855	386
	4020	3975	3900	3860	3850	3845	3855	386
123	4200	4140	4063	4000	3980	3965	3980	400
	4200	4135	4060	4000	3980	3970	3980	400
126	2765	2750	2743	2735	2720	2717	2730	274
	2760	2745	2743	2725	2715	2720	2730	273
127	3260	3238	3219	3195	3180	3175	3183	320
	3270	3245	3225	3200	3185	3183	3197	320

r Circular Surface – Solid Tungsten Specimen in Vacuum

-Axis, in.			Radial Locations from Center Along Y-Axis, in.					
0.45	0.60	0.76	0	0.15	0.30	0.45	0.60	0.76
2320	2331	2332	2310	2316	2318	2318	2322	2331
2320	2328	2332	2310	2318	2319	2318	2323	2332
2700	2720	2735	2682	2690	2692	2700	2718	2730
2700	2715	2730	2685	2690	2692	2700	2718	2730
3070	3090	3122	3042	3045	3055	3070	3090	3120
3075	3090	3110	3045	3045	3055	3065	3085	3120
3430	3480	3520	3380	3390	3380	3400	3440	3500
3430	3470	3520	3380	3380	3380	3400	3450	3490
2048	2050	2060	2045	2043	2040	2045	2052	2057
2045	2053	2060	2045	2043	2043	2045	2050	2057

X-Axis, in.			Radial Locations from Center Along Y-Axis, in.					
0.45	0.60	0.70	0	0.15	0.30	0.45	0.60	0.70
2522	2530	2540	2520	2530	2522	2525	2537	2541
2522	2530	2540	2525	2527	2526	2525	2535	2543
2870	2887	2910	2850	2860	2863	2875	2890	2910
2870	2890	2905	2850	2858	2863	2880	2890	2910
3700	3750	3800	3640	3643	3650	3680	3720	3740
3700	3750	3790	3640	3650	3650	3680	3720	3760
3920	3980	4020	3843	3855	3860	3900	3940	4000
3920	3980	4030	3843	3855	3865	3900	3940	4000
4055	4125	4200	3965	3980	3985	4010	4050	4110
4060	4125	4200	3965	3980	3985	4010	4050	4120
2740	2750	2765	2715	2730	2745	2745	2755	2767
2740	2745	2762	2722	2738	2740	2750	2760	2763
3205	3225	3245	3175	3195	3200	3225	3250	3266
3215	3235	3255	3187	3210	3220	3225	3250	3270

Observed Brightness Temperatures Over Upper Circular Surfac

	Radial Locations from Center Along X-Axis, in.											
Run No.	0.70	0.60	0.55	0.50	0.40	0.30	0.20	0	0.20	0.30	0.40	0.5(
79	1978	1958	1947	1930	1909	1902	1880	1860	1885	1900	1920	195
	1976	1960	1951	1938	1911	1888	1890	1860	1885	1900	1920	194
80	2062	2065	2040	2020	1988	1965	1958	1950	1960	1982	2012	205
	2070	2065	2045	2030	2000	1970	1960	1951	1968	1983	2017	205
81	1999	1992	1977	1962	1932	1920	1907	1895	1915	1930	1950	199
	1999	1994	1980	1960	1933	1916	1903	1895	1915	1930	1952	200
83	2345	2329	2290	2263	2230	2202	2182	2168	2190	2213	2263	232
	2352	2325	2298	2268	2239	2212	2183	2170	2188	2215	2270	232

	Radial Locations from Center Along X-Axis, in.											
	0.70	0.60	0.55	0.50	0.40	0.30	0.15	0	0.15	0.30	0.40	0.5(
84	2383	2370	2350	2311	2275	2240	2213	2197	2208	2245	2275	234
	2391	2375	2347	2311	2284	2240	2210	2204	2212	2252	2290	233
85	2338	2327	2291	2270	2225	2198	2160	2148	2157	2191	2238	227
	2335	2327	2300	2281	2225	2200	2167	2148	2168	2202	2235	228
86	2907	2910	2860	2825	2760	2680	2620	2600	2620	2675	2740	286
	2920	2920	2872	2840	2775	2670	2625	2602	2618	2675	2750	285
87	2905	2895	2835	2815	2745	2680	2600	2590	2620	2690	2750	285
	2910	2905	2850	2820	2742	2665	2595	2590	2620	2690	2750	285
88	3225	3250	3190	3110	3045	2940	2860	2815	2860	2940	3020	316
	3230	3245	3200	3110	3050	2950	2860	2820	2860	2945	3030	315
89	2038	2028	2008	1980	1960	1945	1925	1925	1930	1952	1976	200
	2040	2030	2008	1982	1961	1948	1927	1925	1930	1955	1979	201(
90	2262	2248	2225	2195	2157	2120	2095	2092	2108	2142	2160	221
	2272	2235	2227	2202	2161	2122	2100	2095	2110	2147	2180	221
91	2565	2600	2540	2520	2470	2400	2350	2335	2350	2398	2455	254
	2580	2580	2550	2520	2565	2410	2357	2335	2350	2402	2460	254
92	2970	3000	2930	2875	2790	2730	2640	2625	2655	2710	2790	288
	2970	2980	2935	2870	2790	2720	2640	2622	2655	2710	2790	290

e – 1½-Inch Porous Wah Chang Specimen in Vacuum

				Radial Locations from Center Along Y-Axis, in.							
)	0.55	0.60	0.70	0	0.20	0.30	0.40	0.50	0.55	0.60	0.70
0	1967	1978	1992	1858	1872	1885	1890	1925	1938	1942	1945
8	1968	1988	2000	1863	1872	1885	1898	1919	1930	1947	1942
0	2062	2083	2107	1950	1953	1970	1983	2010	2022	2048	2040
5	2068	2085	2112	1952	1953	1975	1988	2012	2030	2048	2050
5	2010	2028	2030	1899	1900	1922	1945	1972	1985	2010	2010
0	2013	2032	2032	1900	1900	1925	1950	1980	1993	2013	2010
0	2352	2367	2413	2168	2190	2225	2265	2295	2335	2360	2375
8	2360	2370	2425	2175	2192	2226	2258	2312	2338	2357	2365

				Radial Locations from Center Along Y-Axis, in.							
)	0.55	0.60	0.70	0	0.15	0.30	0.40	0.50	0.55	0.60	0.70
5	2387	2415	2412	2200	2217	2250	2298	2322	2360	2380	2382
5	2372	2418	2418	2198	2217	2242	2288	2325	2365	2395	2379
9	2320	2340	2360	2161	2161	2200	2238	2270	2296	2325	2320
8	2312	2342	2350	2155	2168	2203	2230	2278	2305	2325	2325
0	2900	2940	2960	2590	2605	2655	2715	2795	2863	2885	2940
5	2880	2950	2960	2598	2610	2660	2725	2810	2870	2920	2900
0	2895	2945	2980	2590	2610	2665	2740	2805	2870	2885	2920
5	2890	2950	2980	2590	2600	2670	2740	2810	2865	2890	2925
0	3200	3280	3320	2820	2857	2955	3040	3150	3210	3245	3210
5	3230	3280	3340	2830	2890	2970	3030	3170	3210	3255	3220
5	2025	2050	2060	1925	1932	1948	1962	1990	2008	2020	2038
)	2032	2055	2060	1929	1932	1955	1969	1994	2010	2032	2038
)	2242	2257	2300	2090	2102	2120	2153	2190	2215	2223	2250
)	2237	2258	2290	2085	2104	2120	2162	2187	2210	2238	2250
)	2570	2600	2620	2338	2360	2392	2440	2495	2545	2570	2605
)	2580	2610	2630	2340	2360	2397	2460	2510	2545	2570	2615
)	2930	2995	3015	2625	2655	2690	2780	2855	2925	2970	2960
)	2940	2990	3005	2620	2660	2715	2785	2855	2925	2970	2960

Observed Brightness Temperatures Over Upper Circular Surf

Run No.	Radial Locations from Center Along X-Axis, in.										
	0.70	0.60	0.55	0.50	0.40	0.30	0.15	0	0.15	0.30	0.40
93	3465	3500	3420	3355	3225	3100	3000	2970	3000	3110	3210
	3465	3500	3440	3355	3240	3105	3000	2970	3000	3100	3230
94	3740	3760	3700	3580	3410	3280	3130	3085	3130	3280	3400
	3730	3740	3700	3600	3380	3260	3130	3085	3130	3270	3400
114	3940	4060	3930	3840	3640	3500	3350	3290	3340	3480	3660
	—	—	3960	3835	3640	3510	3350	3290	3330	3490	3620
115	4110	4230	4180	4040	3820	3700	3500	3470	3490	3700	3820
	—	—	4200	4050	3830	3695	3510	3430	3480	3680	3840
116	4410	4560	4500	4280	4110	3840	3660	3580	3660	3860	4000
	—	—	4480	4340	4090	3860	3670	3600	3660	3860	4020

ce – 1½-Inch Porous Wah Chang Specimen in Vacuum (Continued)

Radial Locations from Center Along Y-Axis, in.											
0.50	0.55	0.60	0.70	0	0.15	0.30	0.40	0.50	0.55	0.60	0.70
3355	3480	3550	3610	2980	3020	3100	3215	3310	3440	3490	3480
3350	3500	3540	3540	2990	3020	3110	3230	3345	3440	3470	—
3630	3740	3820	3860	3115	3160	3260	3410	3610	3720	3740	3720
3630	3740	3820	3880	3115	3165	3270	3420	3600	3700	3760	—
3840	4020	4070	4050	3310	3370	3540	3670	3880	4000	4010	—
3840	3970	—	—	3300	3370	3530	3670	3900	3980	—	—
4070	4220	4280	4260	3450	3540	3680	3830	4100	4180	4280	—
4060	4220	—	—	3440	3520	3680	3860	4090	4180	—	—
4300	4500	4540	—	3600	3690	3870	4070	4300	4450	4540	—
4330	4520	—	—	3580	3670	3860	4060	4300	4450	—	—

Observed Brightness Temperatures Over Upper Circular Surface –

Radial Locations from Center Along X-Axis, in.

Run No.	0.70	0.60	0.55	0.50	0.40	0.30	0.15	0	0.15	0.30	0.40	0.50
96	2508	2505	2480	2445	2373	2327	2282	2272	2288	2342	2388	2460
	2504	2510	2485	2438	2373	2325	2288	2272	2300	2345	2395	2468
97	2100	2082	2065	2040	1985	1958	1922	1912	1927	1948	1985	2038
	2090	2090	2063	2040	1985	1960	1922	1914	1927	1952	1985	2037
98	2435	2440	2410	2375	2312	2285	2220	2200	2235	2280	2305	2375
	2445	2440	2415	2375	2312	2280	2218	2210	2225	2275	2305	2380
99	2273	2272	2245	2210	2143	2105	2060	2050	2065	2115	2165	2210
	2272	2270	2250	2210	2145	2110	2070	2058	2065	2112	2155	2215
100	2710	2740	2700	2675	2575	2520	2465	2460	2475	2545	2590	2680
	2720	2725	2710	2670	2570	2525	2470	2450	2475	2540	2600	2675
101	2995	3045	3020	2960	2830	2770	2700	2660	2700	2780	2870	2970
	3005	3048	3025	2955	2850	2780	2695	2670	2695	2780	2860	2960
102	3335	3315	3290	3220	3090	3010	2910	2885	2925	3020	3120	3235
	3320	3310	3290	3240	3090	3020	2920	2880	2915	3020	3080	3225
103	3540	3600	3535	3460	3323	3217	3120	3080	3095	3220	3350	3490
	3555	3590	3535	3470	3320	3217	3100	3080	3095	3230	3300	3400

$1\frac{1}{2}$-Inch Porous Wah Chang Specimen in Helium (150 psia)

Radial Locations from Center Along Y-Axis, in.										
0.55	0.60	0.70	0	0.15	0.30	0.40	0.50	0.55	0.60	0.70
2520	2545	2560	2272	2290	2328	2380	2438	2480	2520	2485
2520	2550	—	2272	2296	2333	2390	2440	2480	2515	2510
2050	2075	2060	1905	1918	1950	1980	2015	2050	2052	2060
2052	2085	2080	1910	1920	1955	1980	2022	2050	2058	—
2415	2445	2445	2215	2225	2272	2300	2362	2395	2415	2420
2420	2445	—	2215	2227	2265	2305	2372	2390	2410	—
2258	2270	2265	2050	2060	2087	2122	2175	2215	2228	2235
2260	2273	—	2054	2055	2094	2120	2190	2215	2245	—
2740	2750	2740	2450	2460	2510	2560	2640	2680	2725	2730
2720	2770	—	2450	2480	2520	2575	2650	2705	2740	—
3040	3040	3040	2680	2680	2750	2840	2930	3000	3020	3040
3035	3040	—	2670	2695	2750	2840	2950	3000	3020	—
3320	3350	3330	2890	2910	2990	3080	3205	3260	3300	3290
3320	3330	—	2890	2920	3010	3105	3220	3270	3300	—
3540	3630	3600	3060	3095	3200	3295	3460	3530	3600	—
3580	3610	—	3050	3110	3205	3330	3460	3530	—	—

Observed Brightness Temperatures Over Upper Circular Surface

Run No.	Radial Locations from Center Along X-Axis, in.											
	0.70	0.60	0.55	0.50	0.40	0.30	0.15	0	0.15	0.30	0.40	0.50
104	2045	2060	2060	2025	1978	1940	1900	1890	1907	1945	1980	2030
	2048	2052	2051	2025	1978	1935	1900	1892	1910	1940	1980	2020
105	2245	2265	2255	2225	2165	2130	2090	2980	2905	2135	2190	2240
	—	—	2260	2225	2165	2137	2095	2080	2095	2135	2185	2245
106	2600	2660	2630	2593	2520	2470	2400	2385	2400	2460	2530	2600
	—	—	2630	2600	2530	2470	2405	2387	2400	2468	2530	2592
107	2900	2950	2925	2880	2770	2705	2635	2615	2635	2710	2790	2870
	2910	2960	2930	2870	2780	2705	2637	2615	2638	2717	2780	2870
108	3130	3210	3180	3120	3015	2940	2855	2820	2840	2950	3025	3145
	—	—	3190	3135	3030	2940	2855	2820	2850	2950	3030	3145
109	3430	3450	3420	3380	3230	3130	3055	3040	3060	3180	3280	3430
	—	—	3420	3360	3230	3140	3045	3030	3065	3200	3275	3420
110	3770	3830	3770	3735	3600	3460	3340	3300	3360	3500	3640	3760
	—	—	3790	3740	3600	3460	3350	3300	3360	3490	3630	3770
111	3950	4000	3970	3900	3750	3620	3480	3435	3500	3655	3780	3930
	—	—	3990	3900	3760	3630	3480	3435	3500	3660	3810	3960
112	4120	4180	4140	4085	3920	3780	3625	3600	3640	3790	3925	4095
	—	—	4155	4090	3935	3780	3630	3580	3640	3810	3925	4110
113	4370	4455	4440	4380	4200	4020	3880	3820	3900	4060	4200	4400
	—	—	4455	4380	4200	4020	3860	3820	3880	4060	4200	4380

- 1½-Inch Porous Wah Chang Specimen in Hydrogen (150 psia)

Raidal Locations from Center Along Y-Axis, in.										
0.55	0.60	0.70	0	0.15	0.30	0.40	0.50	0.55	0.60	0.70
2054	2070	2072	1900	1909	1925	1953	1995	2010	2030	2025
2052	2080	—	1900	1905	1922	1950	1990	2010	—	—
2275	2288	2270	2080	2088	2118	2155	2205	2235	2255	2250
2265	—	—	2085	2090	2120	2152	2200	2225	—	—
2620	2660	2630	2385	2400	2432	2490	2560	2590	2620	2620
2630	—	—	2385	2395	2435	2485	2560	2590	—	—
2925	2950	2940	2620	2630	2690	2760	2850	2890	2920	2880
2930	—	—	2620	2630	2690	2770	2850	2880	—	—
3205	3230	3180	2825	2860	2935	3010	3110	3150	3210	3150
3195	—	—	2830	2860	2935	3010	3120	3140	—	—
3470	3500	3470	3020	3050	3150	3220	3340	3400	3460	3430
3480	—	—	3015	3040	3150	3220	3340	3400	—	—
3830	3860	3840	3300	3340	3450	3560	3700	3760	3815	3760
3840	—	—	3300	3345	3460	3560	3720	3780	—	—
4000	4040	3980	3440	3500	3630	3750	3910	3970	4010	3960
3995	—	—	3460	3495	3640	3750	3930	3980	—	—
4180	4220	4140	3580	3650	3770	3940	4060	4120	4170	4100
4170	—	—	3590	3640	3780	3920	4070	4130	—	—
4460	4520	—	3820	3870	4020	4170	4340	4410	4440	—
4450	—	—	3820	3880	4020	4160	4350	4430	—	—

Observed Brightness Temperatures Over Upper Circular Surface – 1-Inch Porous Wa

Run No.	Radial Locations from Center Along X-Axis, in.										
	0.45	0.40	0.35	0.25	0.15	0	0.15	0.25	0.35	0.40	0.45
137	1990	1975	1962	1950	1925	1910	1920	1935	1950	1968	1975
	1993	1975	1965	1950	1925	1915	1920	1932	1950	1967	1975
138	2419	2382	2365	2325	2285	2270	2285	2315	2360	2370	2370
	2423	2390	2365	2325	2290	2273	2289	2315	2360	2370	2373
139	2830	2780	2765	2690	2640	2620	2645	2680	2725	2770	2780
	2820	2790	2760	2710	2650	2625	2650	2680	2760	2770	2800
140	3210	3180	3155	3035	2966	2910	2960	3025	3090	3135	3135
	3210	3200	3150	3025	2966	2930	2975	3050	3090	3135	3155
141	3640	3630	3550	3300	3270	3240	3290	3380	3490	3540	3530
	3640	3620	3540	3400	3260	3240	3290	3380	3490	3530	3510
142	3890	3890	3880	3700	3540	3500	3580	3660	3810	3850	3850
	3930	3940	3900	3700	3520	3500	3570	3700	3820	3870	3820
143	4240	4200	4180	3920	3790	3700	3810	3920	4080	4120	4090
	4250	4230	4165	3950	3790	3700	3810	3930	4090	4140	—
144	4610	4520	4490	4260	4080	3930	4080	4260	4440	4450	4400
	4610	4540	4520	4280	4090	3970	4060	4280	4380	4470	—

h Chang Specimen (Sans Solid Ring) in Vacuum

Radial Locations from Center Along Y-Axis, in.

0	0.15	0.25	0.35	0.40	0.45
1910	1920	1945	1957	1967	1977
1911	1930	1943	1952	1962	1972
2270	2300	2310	2340	2362	2380
2270	2282	2305	2362	2380	2380
2620	2635	2690	2750	2770	2790
2620	2635	2680	2750	2790	2790
2920	2965	3030	3100	3120	3140
2925	2960	3020	3110	3115	3130
3230	3280	3380	3520	3500	3530
3220	3290	3380	3480	3500	3480
3490	3570	3700	3830	3860	3830
3490	3580	3690	3850	3830	3830
3700	3790	3920	4080	4100	4140
3700	3820	3930	4120	4150	4100
3960	4030	4210	4410	4455	4400
3930	4050	4260	4445	4480	—

Observed Brightness Temperatures Over Upper Circular Surface – 1-In

Run No.	Radial Locations from Center Along X-Axis, in. 0.45	0.40	0.35	0.25	0.15	0	0.15	0.25	0.35
145	2015	2022	1998	1947	1910	1905	1920	1949	1980
	2023	2018	1985	1950	1910	1905	1915	1950	1980
146	2345	2343	2303	2258	2212	2183	2197	2228	2270
	2343	2330	2308	2258	2200	2175	2197	2240	2280
147	2680	2656	2644	2570	2506	2480	2506	2550	2605
	2690	2656	2640	2570	2500	2485	2510	2545	2610
148	2910	2890	2850	2775	2710	2690	2720	2790	2845
	2930	2900	2865	2780	2710	2680	2730	2790	2855

ch Porous Wah Chang Specimen (Sans Solid Ring) in Vacuum

Radial Locations from Center Along Y-Axis, in.							
0.40	0.45	0	0.15	0.25	0.35	0.40	0.45
1992	2000	1900	1915	1948	1975	1980	2005
1992	1995	1905	1915	1948	1978	1986	2000
2300	2280	2173	2197	2230	2265	2270	2280
2300	—	2170	2190	2215	2255	2275	—
2640	2630	2485	2520	2555	2585	2610	2620
2635	2620	2480	2515	2565	2600	2610	—
2870	2840	2680	2720	2775	2840	2850	2840
2870	—	2685	2725	2775	2840	2860	—

Observed Brightness Temperatures Over Upper Ci

Run No.	Radial Locations from Center Along X-Axis, in. 0.70	0.60	0.50	0.40	0.30	0.20	0	0.15	0.30
2	3326	3415	3283	3205	3010	2920	2810	2850	2970
	3317	3422	3320	3220	3010	2930	2843	2840	2963

	Radial Locations from Center Along X-Axis, in. 0.70	0.60	0.50	0.40	0.30	0.20	0	0.20	0.30
3	1883	1860	1840	1789	1769	1735	1732	1750	1769
	1885	1865	1845	1785	1769	1742	1730	1749	1769
4	2310	2289	2251	2170	2108	2075	2040	2077	2110
	2315	2285	2252	2163	2112	2079	2050	2079	2110

	Radial Locations from Center Along X-Axis, in. 0.70	0.60	0.45	0.30	0.15	0	0.15	0.30
5	2685	2690	2545	2440	2320	2312	2325	2420
	2690	2700	2540	2410	2328	2315	2324	2410
6	3155	3217	2990	2853	2678	2645	2685	2810
	3175	3217	2979	2840	2665	2635	2678	2820
14	3460	3500	3330	3100	2920	2870	2920	3090
	3480	3490	3330	3130	2910	2860	2905	3070

:cular Surface – 1½-Inch Porous Trial Specimen in Vacuum

				Radial Locations from Center Along Y-Axis, in.						
0.45	0.50	0.60	0.70	0	0.20	0.30	0.40	0.50	0.60	0.70
3200	—	3390	—	2821	2910	2990	3150	3315	3400	3480
3220	—	3410	—	2850	2910	3020	3170	3300	—	3480

				Radial Locations from Center Along Y-Axis, in.					
0.40	0.50	0.60	0.70	0	0.15	0.30	0.45	0.60	0.70
1790	1825	1859	1880	1735	1735	1755	1785	1840	1873
1799	1825	1861	1870	1735	1737	1758	1785	1841	1874
2151	2217	2293	2318	2052	2069	2105	2155	2260	2300
2161	2221	2301	2308	2044	2065	2105	2150	2260	2300

			Radial Locations from Center Along Y-Axis, in.					
0.45	0.60	0.70	0	0.15	0.30	0.45	0.60	0.70
2540	2664	2720	2305	2310	2371	2492	2630	2685
2525	2680	2710	2305	2315	2369	2501	2635	2700
3000	3175	3160	2640	2670	2820	2980	3160	3140
3015	3170	3150	2643	2687	2818	2970	3150	3170
3245	3480	3480	2870	2890	3040	3175	3380	3580
3210	3505	3490	2860	2880	3020	3195	2290	3600

Observed Brightness Temperatures Over Upper Circular Surfac

Run No.	Radial Locations from Center Along X-Axis, in.								
	0.70	0.60	0.45	0.30	0.15	0	0.15	0.30	0.45
9	1805	1830	1742	1690	1642	1632	1645	1670	1730
	1805	1830	1740	1682	1640	1630	1647	1682	1730
10	2278	2307	2190	2120	2035	2025	2040	2097	2185
	2288	2320	2198	2119	2040	2025	2047	2110	2188
11	2675	2695	2570	2470	2349	2338	2370	2445	2560
	2680	2725	2570	2470	2351	2332	2373	2435	2570
12	3064	3140	2970	2835	2700	2660	2710	2830	2960
	3100	3170	2965	2845	2680	2650	2720	2830	2960

e – 1½-Inch Porous Trial Specimen in Helium (150 psia)

Radial Locations from Center Along Y-Axis, in.							
0.60	0.70	0	0.15	0.30	0.45	0.60	0.70
1800	1800	1630	1645	1668	1710	1749	1758
1818	1810	1632	1645	1670	1700	1745	1760
2285	2275	2015	2052	2065	2169	2245	2272
2295	2275	2020	2042	2060	2160	2245	2270
2710	2640	2325	2370	2430	2530	2650	2660
2700	2680	2350	2360	2415	2530	2645	2670
3130	3030	2670	2690	2800	2940	3080	3090
3140	3030	2680	2700	2795	2940	3090	3120

Observed Brightness Temperatures Over Upper Circular Surface – 1-Inch Poro

Run No.	Radial Locations from Center Along X-Axis, in.									
	0.45	0.40	0.35	0.25	0.15	0	0.15	0.25	0.35	0.4
149	—	2015	2010	1955	1928	1910	1940	1960	1983	20
	—	2012	2010	1972	1928	1910	1938	1960	1990	—
150	2339	2358	2350	2288	2232	2222	2250	2293	2332	23
	—	2365	2350	2298	2235	2225	2250	2285	2335	23
151	2762	2750	2720	2640	2570	2550	2580	2640	2680	27
	2750	2750	2710	2630	2565	2545	2500	2630	2690	27
152	3110	3090	3070	2980	2890	2860	2920	2975	3050	30
	3120	3105	3080	2970	2890	2860	2905	2980	3040	30
153	3560	3520	3490	3390	3280	3240	3300	3375	3500	35
	3540	3540	3510	3380	3260	3230	3305	3375	3490	35
154	4360	4380	4370	4240	4070	3995	4090	4200	4320	43
	—	—	4365	4225	4055	4000	4090	4200	4325	—
155	3940	3920	3890	3775	3660	3600	3680	3770	3865	38
	3940	3920	3890	3770	3640	3600	3670	3760	3870	38

s Wah Chang Specimen (Sans Solid Ring) in Hydrogen (150 psia)

		Radial Locations from Center Along Y-Axis, in.					
0	0.45	0	0.15	0.25	0.35	0.40	0.45
.0	—	1910	1950	1970	1985	1999	—
-	—	1910	1940	1965	1980	1990	—
5	2330	2222	2250	2300	2325	2330	2300
5	—	2230	2250	2305	2328	2325	—
0	2660	2550	2570	2620	2670	2690	2680
0	—	2545	2570	2620	2670	2685	—
5	3000	2860	2890	2960	3020	3040	3070
0	—	2860	2895	2960	3010	3040	—
0	3400	3230	3280	3350	3455	3470	3450
0	—	3230	3280	3370	3460	3470	—
0	4280	4000	4060	4190	4280	4310	4270
-	—	4000	4060	4200	4280	—	—
0	—	3600	3640	3730	3840	3860	3840
0	—	3600	3650	3750	3840	—	—

Observed Brightness Temperatures Over Upper Circular Surface – 1½

Radial Locations from Center Along X-Axis, in

Run No.	0.70	0.60	0.45	0.30	0.15	0	0.15	0.30	0.45	0.60
16	2320	2365	2262	2180	2090	2073	2100	2142	2235	2312
	2312	2340	2275	2175	2090	2065	2098	2145	2245	2335
17	2645	2725	2610	2500	2400	2360	2385	2460	2555	2690
	2645	2735	2625	2500	2400	2362	2390	2480	2575	2720
18	3050	3185	3038	2900	2720	2660	2695	2830	3000	3170
	3045	3195	3030	2895	2712	2640	2710	2810	3000	3145
19	3360	3500	3330	3180	2990	2910	2940	3062	3285	3480
	3330	3490	3310	3190	2990	2900	2940	3065	3280	3480

½-Inch Porous Trial Specimen in Hydrogen (150 psia)

	Radial Locations from Center Along Y-Axis, in.					
0.70	0	0.15	0.30	0.45	0.60	0.70
2320	2060	2072	2130	2205	2274	2279
2320	2069	2075	2150	2210	2285	2285
2720	2360	2395	2445	2540	2640	2642
2730	2353	2375	2438	2550	2645	2640
3185	2650	2700	2810	2960	3090	3100
3165	2650	2690	2810	2960	3100	3100
3500	2885	2930	3040	3220	3400	3420
3460	2910	2930	3060	3240	3400	3420

8. NOMENCLATURE

a	Fractional cross-section of gas phase
h_{rp}	Equivalent heat-transfer coefficient, pore-to-pore radiation
h_{rs}	Equivalent heat-transfer coefficient, surface-to-surface radiation
k	Thermal conductivity
ℓ	Length of conduction path
L	Half-length of porous specimen
q_c	Heat flux due to convection
r	Radial coordinate
R_o	Radius to inner edge of heated layer
S_o	Summation of infinite series in solution to temperature-distribution equation
T	Absolute temperature
z	Axial coordinate
β	Ratio of gas thermal conductivity to solid thermal conductivity
δ	Fractional contact area of solid phase
ϵ_T	Total hemispherical emittance
ϵ_λ	Spectral emittance
σ	Stefan-Boltzmann radiation constant
φ	Relative length of conduction path

Subscripts

e Effective

g Gas phase

o Center

s Solid phase

9. REFERENCES

1. M. Hoch and D. Nitti, Technical Report No. ASD TR 61-528, prepared under Contract No. AF33(616)-7123, Wright-Patterson Air Force Base, Ohio
2. J. Mann and N. Blais, Thermal Conductivity of Helium and Hydrogen at High Temperatures, LA-2316 (Sept. 1959).
3. N. Grier, Calculation of Transport Properties and Heat Transfer Parameters of Dissociating Hydrogen, NASA TN D-1406.
4. S. Yagi and D. Kunii, Studies on Effective Thermal Conductivities in Packed Beds, A.I.Ch.Eng. 3:3 (Mar. 1957).
5. D. Kunii and J. Smith, Heat Transfer Characteristics of Porous Rocks, A.I.Ch.Eng. 6:1 (Mar. 1960).
6. R. Deissler and C. Eian, Investigation of Effective Thermal Conductivities of Powders, NACA RM E52C05 (June 1952).
7. R. Gorring and S. Churchill, Thermal Conductivity of Heterogeneous Materials, Ch. Eng. Prog., 57:7 (July 1961).
8. A. Goldsmith, T. Waterman, and H. Hirschhorn, "Handbook of Thermophysical Properties of Solid Materials," Vol. I, Elements (Melting Temperature above 1000°F), Pergamon Press, New York, 1961.
9. W. Wood, H. Deem, and C. Lucks, The Emittance of Chromium, Columbium, Molybdenum, Tantalum, and Tungsten, DMIC Memorandum 141, (Dec. 1961).
10. R. Allen, Total Emissivity and Spectral Emissivity at 0.65μ of Porous Tungsten-Bearing Alloys Above 1600°K, J. ARS, 3216 (June 1962).
11. T. Reynolds and L. Kreps, Gas Flow, Emittance, and Ion Current Capabilities of Porous Tungsten, NASA TN D-871 (Aug. 1961).
12. M. Jakob, "Heat Transfer," Vol. I, John Wiley & Sons, New York, 1956.
13. E. Eckert and R. Drake, "Heat and Mass Transfer," McGraw-Hill Book Co., New York, 1959.